

**Photorefractive Damage Resistance in Periodically Poled  
Lithium Niobate (PPLN) Waveguides with Ridge Geometry**

*A THESIS*

*submitted by*

**SHANTANU PAL**

*for the award of the degree*

*of*

**DOCTOR OF PHILOSOPHY**



**DEPARTMENT OF ELECTRICAL ENGINEERING  
INDIAN INSTITUTE OF TECHNOLOGY MADRAS  
CHENNAI - 600036, INDIA**

**APRIL 2016**

# THESIS CERTIFICATE

This is to certify that the thesis titled **Photorefractive Damage Resistance in Periodically Poled Lithium Niobate (PPLN) Waveguides with Ridge Geometry**, submitted to the Indian Institute of Technology, Madras, by **SHANTANU PAL**, for the award of the degree of **Doctor of Philosophy**, is a bonafide record of the research work done by him under my supervision. The contents of this thesis, in full or in parts, have not been submitted to any other Institute or University for the award of any degree or diploma.

**Dr. Bijoy Krishna Das**  
Research Guide  
Associate Professor  
Department of Electrical Engineering  
IIT Madras, 600 036

Place: Chennai, India

Date: Wednesday 6<sup>th</sup> April, 2016

*This thesis is dedicated to my family.*

*For their endless love and support.*

## ACKNOWLEDGEMENTS

The journey through my PhD study has been a wonderful learning session. Today when I look back, I can understand that really well by seeing the changes in me. It has evolved me as a more matured person both scientifically as well as in life outside academics. I would like to express sincere gratitude to my PhD supervisor Dr. Bijoy Krishna Das for everything I have learned during PhD. He has selected me as his first PhD student and given me the unique opportunity to develop my own research facilities starting from the scratch. The training I have received from him during my entire stay in IIT Madras will be a valuable asset throughout my life. He has also been instrumental in facilitating the entire process for carrying out a part of my PhD work in University of Paderborn, Germany under the guidance of Prof. Wolfgang Sohler. I consider myself really lucky for getting an opportunity to work with Prof. Sohler, of course it would not have been possible without a recommendation from my supervisor. Prof. Sohler not only gave me the opportunity to work with his internationally renowned research group, also supported me financially through one of his research projects during my entire stay in Paderborn. The devices which I have investigated during my thesis work were also fabricated in his laboratory, for which I will be always deeply indebted to him. I have learned a lot from him as well as from his research group during my stay in Paderborn, which have enriched me further as a researcher.

I would like to express my sincere gratitude to doctoral committee members Prof. Harishankar Ramachandran, Prof. Nandita Dasgupta, Prof. Nilesh J. Vasa and Prof. C. Vijayan for their valuable comments and suggestions. I will be always grateful to Prof. Amitava Dasgupta, Prof. Enakshi Bhattacharya and all other faculty members associated with MEMS & Microelectronics laboratory for their support at various stages of my research work.

Seniors Dr. Jaibir Sharma, Dr. Somesekhar Bhat, Dr. Jayadeva G. S, Dr. L. Sujatha, Dr. Binsu have helped me a lot by teaching me basics of fabrication towards the beginning of my PhD work. Working in the lab was always great fun because of the company of my present and former labmates. I am really thankful to Rupesh, Meenatchi, Sujith, Solomon, Narendran, G. Sridhar, John, Gaurang, Harish, Karthik, Sakthivel, Rashmi, Sidharth, Sreevatsa,



Saket, Dadavali, Parimal, Riddhi, Sumi, Sireesha, Usman, Ramesh, Amrutha for giving me a good company in the lab at various points of time. They have extended their help whenever needed, and it was really a great opportunity for me to be a part of such a lively research group-“Integrated Optoelectronics Group”. I am thankful to Dr. Mathew George for being my mentor during my stay in Paderborn and helping me in all possible way both inside and outside the lab to make my stay in Germany fruitful.

Finally, I must admit that the most valuable support I have always received from my family. My parents, though they did not understand much about my work they were always supportive and encouraging with their words and blessings. My better-half Ananya, who is also my best-friend is the main source of my strength and motivation. She always stood by me through thick and thin. She has taken care of all family needs and raised our little princess Anoushka almost single-handedly! I don't think any word is enough to express the depth of love and support that I have always received from her as I was chasing my dream.

**Shantanu Pal**

Place: Chennai, India

Date: Wednesday 6<sup>th</sup> April, 2016

# ABSTRACT

**KEYWORDS:** Lithium niobate, integrated optics, nonlinear optics, periodic poling, ridge waveguides, channel waveguides, photorefractive damage.

All-optical wavelength conversion is the most desirable option to use in DWDM-networks as it solves the channel contention problem, increases the network flexibility, efficiency and provides a dynamic reconfiguration of the network. Nonlinear integrated optical devices fabricated using periodically poled lithium niobate (PPLN) waveguides have received extensive attention in all-optical signal processing due to their interesting features (e.g. low propagation-loss, very high conversion efficiency, ultra-fast optical response etc.). A thorough literature survey reveals that these devices also suffer from photorefractive damage in presence of near-IR radiations ( $\lambda < 900$  nm). Even devices operating at communication wavelengths ( $\lambda \sim 1550$  nm) are also affected by the photorefractive damage because of the generation of shorter wavelengths during various nonlinear wavelength conversion processes. Photorefractive damage decreases the overall performance of a nonlinear integrated optical device. Hence, the suppression and control of photorefractive damage in lithium niobate waveguides is an active area of research over the years. Recently, it has been experimentally demonstrated that the ridge waveguide has much higher threshold for photorefractive damage compared to a standard diffused channel waveguide in presence of a high power radiation near the room temperature. But, a detailed investigation which can give further insight into this interesting feature of the PPLN ridge waveguide is still missing.

This thesis begins with a description of state-of-the-art understanding of photorefractive effect in bulk lithium niobate crystal and subsequently explains the superiority of ridge waveguide geometry in terms of photorefractive damage resistance for guided modes. Titanium-indiffused PPLN channel and ridge waveguides have been theoretically analyzed for efficient second harmonic generation and then the damage-resistant characteristics of the

PPLN ridge waveguide during second harmonic generation has been studied. Experimental investigations have been carried out on PPLN ridge and channel waveguides to validate the theoretical prediction. As expected, second harmonic measurements showed that the PPLN ridge waveguide (length - 15 mm) could sustain with a power level of  $P_{SH} > 10$  mW at room temperature without significant degradation of the phase-matching characteristics, whereas in case of channel waveguide (length - 36 mm)  $P_{SH} \sim 0.4$  mW could easily destroy the phase matching characteristics. The generated second harmonic power in ridge waveguide was also found to be stable as a function of time at room temperatures. The experimentally observed blue-shift in phase-matched wavelengths has been justified by the inherent bulk photorefractive effect of  $\text{LiNbO}_3$ . Thus, experimental results support the theoretical prediction and provides a reasonable explanation of the damage resistant characteristics in a PPLN ridge waveguide.

# TABLE OF CONTENTS

<b>ACKNOWLEDGEMENTS</b>	<b>ii</b>
<b>ABSTRACT</b>	<b>iv</b>
<b>LIST OF TABLES</b>	<b>viii</b>
<b>LIST OF FIGURES</b>	<b>xii</b>
<b>ABBREVIATIONS</b>	<b>xiii</b>
<b>NOTATION</b>	<b>xv</b>
<b>1 Introduction</b>	<b>1</b>
1.1 Motivation . . . . .	1
1.2 Research Objective . . . . .	3
1.3 Thesis Organization . . . . .	5
<b>2 Photorefractive Effect: Background Study</b>	<b>7</b>
2.1 Physics of Photorefractive Effect . . . . .	7
2.2 Analytical Model of Photorefractive Effect . . . . .	9
2.3 Photorefraction in LiNbO <sub>3</sub> Waveguides . . . . .	16
2.4 Conclusions . . . . .	19
<b>3 Damage Resistance in PPLN Ridge Waveguides</b>	<b>21</b>
3.1 Waveguide Design . . . . .	21
3.1.1 Single mode guidance . . . . .	21
3.1.2 Effective mode area . . . . .	28
3.2 QPM-Second Harmonic Generation . . . . .	30
3.3 Modal Stability in Ridge Waveguides . . . . .	35
3.4 Photorefraction Induced Detuning of $\lambda_{QPM}$ . . . . .	38

3.5	Conclusions . . . . .	40
<b>4</b>	<b>Device Fabrication and Experiments</b>	<b>41</b>
4.1	APE Ridge Waveguides: Preliminary Studies . . . . .	41
4.2	Ti:PPLN Waveguides: Sample Preparation . . . . .	48
4.3	Photorefractive Damage : Experimental Results . . . . .	58
4.3.1	Photorefractive damage of guided modes at $\lambda$ - 635 nm . . . . .	58
4.3.2	Second harmonic generation and characterizations . . . . .	60
4.4	Conclusions . . . . .	74
<b>5</b>	<b>Conclusions</b>	<b>76</b>
5.1	Summary . . . . .	76
5.2	Future Scope of Work . . . . .	78
<b>A</b>	<b>Nonlinear Propagation Equations for Three-Wave Mixing</b>	<b>79</b>
A.0.1	Nonlinear Propagation Equations for Three-Wave Mixing . . . . .	79
<b>B</b>	<b>LIST OF PAPERS BASED ON THESIS</b>	<b>99</b>
<b>C</b>	<b>CURRICULUM VITAE</b>	<b>100</b>
<b>D</b>	<b>DOCTORAL COMMITTEE</b>	<b>101</b>

## LIST OF TABLES

2.1	Typical parameter values for two-center charge transport model. . . . .	16
4.1	Dimensions of Fabricated Ridge Waveguides ( $W_1$ - upper ridge width, $W_2$ - lower ridge width) . . . . .	54
4.2	Propagation Loss for PPLN Ridge Waveguides . . . . .	58
4.3	Descriptions of Ti:PPLN waveguides used for second harmonic generation.	62

## LIST OF FIGURES

2.1	Physical mechanisms of photorefractive effect in LiNbO <sub>3</sub> . . . . .	8
2.2	Scheme of one-center charge transport model (not in scale). . . . .	11
2.3	Scheme of two-center charge transport model (not in scale). . . . .	13
2.4	Evolution of primary and secondary acceptor concentrations as a function of time for different incident intensities of laser light ( $\lambda \sim 488$ nm). . . . .	17
2.5	Intensity dependent change in photo-conductivity $\sigma(I)$ . . . . .	18
2.6	Variation of $\Delta n_{e,sat}$ as a function of $\log_{10}[I(mW/\mu m^2)]$ in LiNbO <sub>3</sub> . . . . .	19
3.1	Schematic of LiNbO <sub>3</sub> waveguides along with crystallographic axes :(a) ridge waveguide, (b) channel waveguide. . . . .	22
3.2	Extraordinary index distribution of LiNbO <sub>3</sub> (a) ridge waveguide (Y-cut, X-propagating, $R_H - 4 \mu m$ , $W - 7 \mu m$ ) and (b) channel waveguide (Z-cut, Y-propagating, $W - 7 \mu m$ ) for Ti-layer thickness - 100 nm, diffusion duration of 8.5 hours at 1060° C. . . . .	23
3.3	Intensity distributions of guided fundamental modes for : (a) ridge waveguide ( $R_H - 4 \mu m$ , $W - 7 \mu m$ ) and (b) channel waveguide ( $W - 7 \mu m$ ) at $\lambda - 1550$ nm. . . . .	25
3.4	Modal dispersion for LiNbO <sub>3</sub> waveguides: (a) ridge ( $R_H - 4 \mu m$ ) and (b) channel. Calculations are carried out for TE- (TM-) mode in case of ridge (channel) waveguide which is used to avail the highest nonlinear coefficient ( $d_{33}$ ) for wavelength conversions. . . . .	26
3.5	Effective index contrast with respect to bulk for the guided fundamental mode as a function of waveguide width for varying ridge heights :(a) $\lambda - 1550$ nm, (b) $\lambda - 775$ nm. Calculations are carried out for TE- (TM-) mode in case of ridge (channel) waveguide which is used to avail the highest nonlinear coefficient ( $d_{33}$ ) for wavelength conversions. . . . .	27
3.6	Effective mode area ( $A_{eff}$ ) for the pump mode :(a) ridge, (b) channel for Ti-layer thickness - 100 nm, diffusion time- 8.5 hours, temperature - 1060° C. Calculations are carried out for TE- (TM-) mode in case of ridge (channel) waveguide which is used to avail the highest nonlinear coefficient ( $d_{33}$ ) for wavelength conversions. . . . .	29
3.7	Calculated (a) SH- conversion efficiency ( $\eta$ ) vs. pump wavelength ( $\lambda_p \sim 1550$ nm), (b) SHG conversion efficiency ( $\eta$ ) vs. coupled pump power $P_p(z = 0)$ for Ti:PPLN channel and ridge waveguides. . . . .	34

3.8	Second Harmonic Conversion efficiency as a function of waveguide length.	35
3.9	Pump intensity profiles for channel (Pol-TM) and PPLN ridge (Pol-TE) waveguide at different internal power : (a) $P_p$ - 1 pW, (b) $P_p$ - 100 $\mu$ W, (c) $P_p$ - 200 $\mu$ W (50 mW) . . . . .	37
3.10	Algorithm used for Photorefractive Mode Calculations. . . . .	38
3.11	Phase-matching wavelength detuning $\Delta\lambda_{QPM}$ due to: (a) low $P_{SH}$ , (b) high $P_{SH}$ (for ridge), (c) temperature change. . . . .	39
4.1	Annealed-proton exchange setup: (a) schematic of the proton exchange reactor, (b) photograph of the proton exchange reactor and (c) photograph of the annealing furnace. . . . .	42
4.2	Microscope picture of fabricated APE Channel Waveguide (length - 2 cm, width - 6 $\mu$ m). . . . .	43
4.3	Fabrication scheme for APE:LiNbO <sub>3</sub> ridge waveguides. . . . .	44
4.4	Surface damage in LiNbO <sub>3</sub> substrate during surface activation. . . . .	45
4.5	Wet etching of LiNbO <sub>3</sub> : (a) etch-dept and(b) surface roughness. . . . .	45
4.6	Wet etch depth vs. proton exchange duration . . . . .	46
4.7	Wet etching of LiNbO <sub>3</sub> :(a) wet-etched surface, (b) wet-etch step height. . . . .	46
4.8	Reactive ion etching of LiNbO <sub>3</sub> by SF <sub>6</sub> : Ar Recipe : (a) step height, (b) surface morphology. . . . .	47
4.9	Reactive ion etching of LiNbO <sub>3</sub> by CHF <sub>3</sub> : Ar recipe : (a) ridge rstructure (side view), (b) ridge rstructure (top view), (c) EDS analysis. . . . .	48
4.10	Scheme of ridge waveguide fabrication: (a) wafer cleaning and, (b) Patterning of Cr- mask, (c) Ridge structure definition, (d) Deposition of Ti-layer on top of the ridge, (e) Ridge waveguide fabrication by Ti-indiffusion. . . . .	49
4.11	SEM micrograph fabricated ridge structure after ICP etching. . . . .	50
4.12	SEM picture of fabricated Ti-indiffused ridge waveguide . . . . .	50
4.13	Local periodic poling :(a)scheme of the electrode pattern, (b) deposited comb-electrode structure. . . . .	51
4.14	Periodic poling setup for ridge waveguide: (a) circuit diagram, (b) photograph of the setup (@ Integrated Optics Group, University of Paderborn). . . . .	52
4.15	Poling characteristics of a Ti-indiffused PPLN ridge waveguide. . . . .	52
4.16	Visualization of micro-domains in a Y-cut PPLN ridge waveguide. . . . .	53
4.17	Ridge waveguide cross-sections : (a) rectangular (W - ridge width, $R_H$ - ridge height), (b) trapezoidal ( $W_1$ - upper ridge width, $W_2$ - lower ridge width, $R_H$ - ridge height), (c) fabricated Y- cut ridge waveguide end-face. . . . .	54



4.18 Schematic of the mode-profile measurement setup. . . . .	55
4.19 Guided intensity profiles for Y-cut PPLN ridge waveguide: (a) TE-polarized wave, (b) TM-polarized wave. . . . .	55
4.20 Guided intensity profiles for Z-cut PPLN channel waveguide: (a) TE-polarized wave, (b) TM-polarized wave. . . . .	56
4.21 Schematic of waveguide propagation loss measurement setup. . . . .	57
4.22 Experimentally measured waveguide propagation loss:(a) TE-pol;(b) TM-pol. . . . .	57
4.23 Experimental setup for investigating photorefractive damage in LiNbO <sub>3</sub> waveguides. . . . .	59
4.24 Evidence of catastrophic photorefractive damage of multimode-excited intensity distributions (extra-ordinarily polarized) in Ti-indiffused LiNbO <sub>3</sub> channel waveguide (L-30 mm)at $\lambda_{PR} = 635$ nm ( $P_{coup} \sim 210 \mu\text{W}$ ): (a) immediately after switching on the laser and (b) after 2 min of irradiation. . . . .	59
4.25 Stable intensity distributions (dominant fundamental mode and extra-ordinarily polarized) in LiNbO <sub>3</sub> ridge waveguide (L -30 mm) at $\lambda_{PR} = 635$ nm ( $P_{coup} \sim 340 \mu\text{W}$ ):(a) immediately after switching on the laser and (b) after 2 min of irradiation. . . . .	60
4.26 Scheme of the experimental setup used for second harmonic generation in PPLN waveguide and measurement of wavelength dependent characteristics. . . . .	61
4.27 Fiber butt-coupling setup. . . . .	62
4.28 Transmission characteristics of dichroic mirror . . . . .	62
4.29 Second harmonic tuning characteristics of PPLN ridge waveguides for a broad pump wavelength range:(a) Waveguide # RG1 (Y-cut ridge waveguide);(b) Waveguide # RG2 (Y-cut ridge waveguide)and (c) Waveguide # RG3 (X-cut ridge waveguide). . . . .	63
4.30 Second harmonic tuning characteristics of PPLN ridge waveguides at 25° C :(a) Waveguide # RG1 (Y-cut ridge waveguide);(b) Waveguide # RG2 (Y-cut ridge waveguide) and (c) Waveguide # RG3 (X-cut ridge waveguide). . . . .	65
4.31 Second harmonic tuning characteristics of reference (Z-cut PPLN channel) waveguides at 30° C :(a) Waveguide # CH1; (a) Waveguide # CH2. . . . .	66
4.32 Photorefractive effect of increasing second harmonic power on PPLN channel waveguide at room temperature. . . . .	66
4.33 SHG power characteristics for Ti:PPLN waveguides as SH-power $P_{SH}$ versus coupled pump power $P_{p,coup}$ measured at 40°C (channel) and 30°C (ridge): (a) Ti:PPLN channel, (b) Ti:PPLN ridge guide. The insets show phase match characteristics at different power levels. . . . .	67

4.34	Detuning of the phase match wavelength $\Delta\lambda_{QPM}$ due to the onset of photorefractive by the generated SH power $P_{SH}$ for both types of waveguides: (a) Ti:PPLN channel and (b) Ti:PPLN ridge guide. . . . .	69
4.35	Detuning $\Delta\lambda$ of the phase matching wavelength versus the sample temperature for both types of waveguides. . . . .	70
4.36	SHG phase matching characteristics for Ti:PPLN waveguides as SH-power $P_{SH}$ versus pump wavelength $\lambda_p$ measured with different (coupled) pump power levels $P_{p,coup}$ after 0, 60 and 120 mins. at room temperature (30°C): (a) Ti:PPLN channel, (b) Ti:PPLN ridge. . . . .	71
4.37	SHG phase matching characteristics for Ti:PPLN ridge guides as SH-power $P_{SH}$ versus pump wavelength $\lambda_p$ measured with a coupled pump power $P_{p,coup} = 650$ mW after 0 <sup>+</sup> , 60 and 120 min at room temperature (30° C). Blue- and red-shifts were observed with time. . . . .	72
4.38	Room temperature stability of generated second harmonic power in ridge waveguide. . . . .	73

## ABBREVIATIONS

### Acronyms

<b>C-Band</b>	Conventional wavelength band ( $\lambda \sim 1527$ to $1567$ nm)
<b>L-Band</b>	Long wavelength band ( $\lambda \sim 1567$ to $1607$ nm)
<b>WDM</b>	Wavelength-division-multiplexing
<b>DWDM</b>	Dense wavelength-division-multiplexing
<b>AOWC</b>	All Optical Wavelength Conversion
<b>APE</b>	Annealed Proton Exchange
<b>IR</b>	Infra-Red
<b>QPM</b>	Quasi-Phase Matched
<b>PPLN</b>	Periodically Poled Lithium Niobate
<b>SHG</b>	Second Harmonic Generation
<b>DFG</b>	Difference Frequency Generation
<b>RTD</b>	Resistance Temperature Detector
<b>PID</b>	Proportional-Integral-Derivative
<b>EDS</b>	Energy Dispersive X-ray Spectroscopy
<b>DI</b>	De-ionized (water)
<b>PPR</b>	Positive Photo Resist
<b>UV</b>	Ultra-Violet
<b>RIE</b>	Reactive Ion Etching
<b>ICP-RIE</b>	Inductively Coupled Plasma- RIE
<b>SEM</b>	Scanning Electron Microscope
<b>FSR</b>	Free Spectral Range
<b>SMF</b>	Single Mode Fiber
<b>EDFA</b>	Erbium Doped Fiber Amplifier
<b>TE</b>	Transverse Electric (polarization)
<b>TM</b>	Transverse Magnetic (polarization)

### *Chemical Names*

<b>C<sub>7</sub>H<sub>6</sub>O<sub>2</sub></b>	Benzoic Acid
<b>H<sup>+</sup></b>	Proton
<b>Al</b>	Aluminum
<b>Ar</b>	Argon
<b>CHF<sub>3</sub></b>	Tri-fluoro Methane
<b>C<sub>4</sub>F<sub>8</sub></b>	Octafluorocyclobutane
<b>Cr</b>	Chromium
<b>HF</b>	Hydro Fluoric Acid
<b>HNO<sub>3</sub></b>	Nitric Acid
<b>H<sub>2</sub>O</b>	Water
<b>H<sub>2</sub>O<sub>2</sub></b>	Hydrogen Peroxide
<b>H<sub>2</sub>SO<sub>4</sub></b>	Sulphuric Acid
<b>NH<sub>4</sub>OH</b>	Ammonium Hydroxide
<b>NaOH</b>	Sodium Hydroxide
<b>SF<sub>6</sub></b>	Sulfur Hexafluoride

### *Units*

<b>dB</b>	Decibel
<b>dBm</b>	Decibel milli-Watts
<b>mW</b>	milli Watts
<b>μm</b>	Micrometer
<b>ps</b>	Pico Second
<b>μs</b>	Micro Second
<b>sccm</b>	standard cubic centimeter per minute
<b>mTorr</b>	milli-Torr (of pressure)
<b>mbar</b>	milli-Bar (of pressure)
<b>ml</b>	milli-liter (of fluid)

## NOTATION

$\mathbf{n}$	Refractive index
$\mathbf{n}_{eff}$	Effective refractive index
$\mathbf{n}_p$	Pump wave effective refractive index
$\mathbf{n}_{SH}$	SH- wave effective refractive index
$\epsilon$	Permittivity
$A_{eff}$	Guided mode area
$S_{eff}^{(2)}$	Effective area of interaction between Pump and SH mode
$\lambda$	Wavelength
$\beta$	Propagation constant
$\Lambda$	Poling period
$L$	Length
$\kappa$	Glass constant
$\alpha$	Loss per unit length
$\lambda_p$	Pump Wavelength
$\lambda_{SH}$	Second Harmonic Wavelength
$\lambda_{QPM}$	Phase-matched wavelength
$\Delta\lambda_{QPM}$	Detuning of $\lambda_{QPM}$

# CHAPTER 1

## Introduction

Lithium niobate ( $\text{LiNbO}_3$ ) is a widely used artificial ferroelectric material with many excellent optical properties (e.g. electro-optic, thermo-optic, acousto-optic, photorefractive and nonlinear-optic effects etc.) [1]. It has been used to demonstrate integrated-optical devices with wide range of applications [2]. Though periodically poled lithium niobate (PPLN) channel waveguides have very low propagation-loss and excellent conversion efficiencies for various second order nonlinear interactions [3]; these waveguides are affected by severe photorefractive damage at higher power levels [4]. Present thesis work is all about a study of photorefractive damage resistance characteristics in PPLN ridge waveguides and to establish its superiority over conventional PPLN channel waveguides. Motivation of this work, research objective and thesis organization have been presented in this introductory chapter.

### 1.1 Motivation

Many optical functions have been implemented using in  $\text{LiNbO}_3$  as bulk material [5], single-crystal fibers [6], thin films [7] and integrated optical substrate (waveguide devices) [8]. Among these waveguide/integrated optical are the most popular class due to well-established and matured waveguide fabrication technologies [9, 10, 11, 12]. Almost all the known integrated optical devices have been demonstrated either with Ti-indiffused ( $\text{Ti:LiNbO}_3$ ) or with annealed proton exchange (APE: $\text{LiNbO}_3$ ) channel waveguides till date. TE/TM-mode splitter (crosstalk  $< -20$  dB, insertion loss 1.7 dB) [13], polarizer (TM-mode extinction  $> 35$  dB) [14], polarization splitter (crosstalk  $< -20$  dB, total insertion loss 3 dB, wavelength independent operation over  $\Delta\lambda \sim 100$  nm) [15], directional coupler (crosstalk upto -24 dB, bar state extinction 47.8 dB) [16] and Y-junction power splitter / combiner (angular separation  $1.1^\circ$ , separation between parallel branches  $30 \mu\text{m}$ , splitting ratio  $\sim 50:50$ ) [17], wavelength multiplexer (insertion loss  $< 3$ dB, temperature sensitivity  $\sim 5.6 \times 10^{-2}$  nm/ $^\circ$  C, tuning rate 2.5 nm/V) [18], wavelength filter (switch data among channels 0.4 nm apart in less than 50

ns, insertion loss  $\sim 19$  dB and crosstalk  $< -22$  dB.) [19], DBR filter (reflectivity  $> 80\%$ ) [20], Bragg grating (reflectivity  $\sim 94\%$  @ 1546 nm) [21] etc. have been fabricated using LiNbO<sub>3</sub> channel waveguides. These components have been used to demonstrate various complex integrated optical devices.

It is worth mentioning here that by exploiting the excellent electro-optic property, high volume LiNbO<sub>3</sub> waveguide modulators with Mach-Zehnder interferometer (MZI) configuration have been commercially produced for ultra-high speed ( $\sim 100$  Gbit/s) data transmission [22, 23]. These are also being used for electric field sensing, optical metrology and in many other allied fields [24, 25, 26, 27]. Recently, ferroelectric domain-inversion technique has been used to develop electro-optic modulators with large bandwidth ( $> 10$  GHz), low driving voltage ( $< 2$  V), adjustable chirp parameters for the output wave and single side-band [28, 29, 30]. Acousto-optic (AO) effect in LiNbO<sub>3</sub> has been used to develop AO tunable filters (AOTFs). This device has a bandwidth of 2.0 nm and a tuning range of 130 nm, with fiber-to-fiber insertion loss  $< 4.6$  dB, residual polarization dependence of 1.3 dB for bar-state and 0.1 dB for cross-state [31]. These filters can be used for configuring WDM-networks. Integrated acousto-optic  $2 \times 2$  switches or add/drop multiplexers have also been developed at an operating wavelength  $\sim 1550$  nm. AO-filters can also be used in spectral slicing of supercontinuum source [32], acoustic modulation [33] and biomedical sensing [34]. Holographic digital memories also have been demonstrated in LiNbO<sub>3</sub> crystals [35, 36, 37]. These devices can be used for secured data storage with 3D encryption [38]. LiNbO<sub>3</sub> based holograms have longer life-time and hence are suitable for commercial applications [39]. Holographic gratings fabricated using LiNbO<sub>3</sub>:Fe can be used to develop narrow-band filters for using in high-resolution spectroscopy, solar and stellar astronomy, LIDAR, terrestrial remote sensing, laser wavelength locking, integrated waveguide lasers, grating couplers, optical sensors, confocal microscopes, wavelength filters etc. [40, 41, 42, 43]. Er-doped LiNbO<sub>3</sub> is a laser active material and it provides optical amplification and lasing in the wavelength range 1530-1576 nm [44, 45, 46, 47, 48]. A new family of compact, efficient, inexpensive waveguide amplifiers and lasers with advanced functionality have been demonstrated using low-loss Er:Ti:LiNbO<sub>3</sub> channel waveguides by exploiting electrooptic, acoustooptic and nonlinear optical properties of LiNbO<sub>3</sub>. These lasers and amplifiers can be combined with other active and passive devices on the same substrate to form

integrated optical circuits to be used in optical communications, sensing, signal-processing and in various measurement techniques [49, 50, 51, 52, 53, 54, 55].

In recent years, quasi-phase matched (QPM) PPLN channel waveguides have been used to demonstrate various second-order nonlinear interactions [56, 57, 58, 59, 60, 61]. These devices exhibit very high nonlinear conversion efficiency, low propagation-loss, ultra-fast optical response, negligible spontaneous emission noise, low cross talk, very low intrinsic frequency chirp and complete transparency to bit rate and modulation format [62]. Compact, stable, high-power and low-noise visible and multi-color laser sources have been demonstrated using PPLN channel waveguides [63, 64, 65, 66]. These lasers can be used in optical data storage, high-brightness displays, color printing, medical science, quantum communication, DWDM-systems and various sensors [67, 68, 69, 70, 71]. LiNbO<sub>3</sub> nonlinear integrated optical devices are considered to be the most promising class of devices which can be for highly efficient all-optical signal processing in modern DWDM-networks [72, 73, 74]. But, these devices are highly sensitive to photorefractive damage at higher pump power levels in presence of generated visible and near-IR waves ( $\lambda < 900$  nm). Photorefractive damage is more prominent in channel waveguides fabricated on congruent crystals. This process cascades itself with the increasing light intensity as the beam propagates through the waveguide and finally degrades the guiding characteristics completely. It is an inherent issue with lithium niobate waveguides with varying degree of sensitivity based on the fabrication methodology [75, 76, 77]. It is the most serious bottleneck for nonlinear integrated optical devices. Hence, proper control and reduction of photorefractive beam-distortion is absolutely essential for any practical application.

## **1.2 Research Objective**

Most commonly used technique for controlling the photorefractive damage in PPLN waveguides is to operate the device at a higher temperature ( $\sim 200^\circ$  C) and increase the dark conductivity, which can subsequently compensate for photo-induced electronic conductivity [78]. But, higher operating temperature makes fiber pigtailling more challenging and results in unstable device performance. Use of stoichiometric substrates for fabricating de-



vices can control the photorefractive damage to a great extent [79, 80]. But, stoichiometric  $\text{LiNbO}_3$  crystals are internally disordered and they have much lower dielectric breakdown voltage, which can cause breakdown during periodic domain inversion process. Another option to control optical damage in  $\text{LiNbO}_3$  is to use various optical damage resistant additives [81, 82, 83]. But, doping results in degradation of the optical quality of the substrate and also exhibits unstable device performance. Similarly, there are some more proposed techniques for the control of photorefractive damage [84, 85, 86], but all these need further investigations and understanding of resulting material behavior. Very recently, it has been demonstrated that, PPLN ridge waveguides are much more tolerant against photorefractive damage. Nishida et al. have demonstrated second harmonic generation ( $@\lambda_{QPM} \sim 1535.8$  nm) using directly bonded PPLN ridge waveguides (length-13 mm, width 10-20  $\mu\text{m}$  and height 30  $\mu\text{m}$ , poling period - 18  $\mu\text{m}$ ) with a peak conversion efficiency  $\sim 44$  %/W. When these waveguides were irradiated with an external high power pump wave ( $\lambda \sim 784$  nm,  $\sim 64$  mW), they did not show any significant damage even after 10 minutes [87]. Sugita et. al. have demonstrated second harmonic generation in a pure crystal directly bonded ridge waveguide fabricated on Y-cut MgO:PPLN wafer (thickness- 4  $\mu\text{m}$ , length - 10 mm, poling period - 3.2  $\mu\text{m}$ ). They could generate  $P_{SH} \sim 40$  mW from  $P_{pump} \sim 67.8$  mW ( $@\lambda_{QPM} \sim 849.2$  nm) at room temperature [88]. Nishida et. al. have generated  $P_{SH} \sim 110$  mW from  $P_{pump} \sim 190$  mW ( $@\lambda_{QPM} \sim 1542.4$  nm) on a ZnO-doped PPLN directly bonded ridge waveguide (length - 55 mm, width - 10  $\mu\text{m}$ , thickness - 6.2  $\mu\text{m}$ , poling period - 18  $\mu\text{m}$ ) at 50° C device temperature without any saturation in second harmonic power due to photorefractive damage [89]. L. Gui et. al. have shown stable  $P_{SH} \sim 50$  mW using  $P_{pump} \sim 700$  mW ( $@\lambda_{QPM} \sim 1548.5$  nm) in a Ti:LiNbO<sub>3</sub> locally poled X-cut ridge waveguide (width 8  $\mu\text{m}$ , height 3  $\mu\text{m}$ , length - 13 mm, poling period - 16.1  $\mu\text{m}$ ) [90]. Jedrzejczyk et. al. have demonstrated  $P_{SH} \sim 386$  mW using  $P_{pump} \sim 1.01$  W ( $\lambda_{QPM} \sim 1061$  nm) at  $\sim 30^\circ$  C in a MgO: PPLN ridge waveguide (length - 11.5 mm, width  $\sim 5$   $\mu\text{m}$  and ridge height 4  $\mu\text{m}$ ) [91]. Sun et.al. have generated  $P_{SH} \sim 466$  mW green laser (CW) near room temperature in a APE-MgO:PPLN ridge waveguide (width - 8.5  $\mu\text{m}$ , length - 1.4 cm long) [92]. All these results clearly demonstrate the photorefractive damage-resistant characteristics in PPLN ridge waveguides.

Due to their photorefractive damage resistant characteristics, PPLN ridge waveguides are ideal candidates for the development of nonlinear integrated optical devices for high power applications near room temperatures. Hence, a complete understanding of this characteristics is essential to design and develop damage-resistant QPM-PPLN waveguides. But, a proper explanation of the mechanism of damage-resistant characteristics in PPLN ridge waveguides is not yet available in literature and it needs further exploration. The main objective of the present research work is to investigate thoroughly the reason behind the higher photorefractive damage threshold in PPLN ridge waveguides in comparison to that of conventional buried channel waveguides and then give a suitable explanation for the same.

### **1.3 Thesis Organization**

With in the scope of the research objective, a theoretical study on the photorefractive damage resistant characteristics of PPLN ridge waveguides has been carried out and it has been explained with the help of it's strong modal confinement. Subsequently, theoretical predictions were validated with further experimental investigations. Accordingly, the entire thesis is organized into three main chapters as discussed below.

In chapter 2, the origin of the photorefractive effect and physics behind the photo-induced charge transport process in  $\text{LiNbO}_3$  have been discussed with the help of well-established theoretical models from the literature. The photorefractive damage in  $\text{LiNbO}_3$  waveguides has been theoretically analyzed using two-center charge transport model.

In chapter 3, second harmonic generation has been theoretically investigated in both Ti-indiffused PPLN channel and ridge waveguide, and it has been shown that a PPLN ridge waveguide with optimized dimensions is more efficient as a second harmonic generator compared to a PPLN channel waveguide. Then the effect of photorefractive damage has been theoretically analyzed in both Ti-indiffused PPLN channel and ridge waveguides and it has been found that, the higher modal confinement in PPLN ridge waveguide provides a better modal stability. Hence, the higher photorefractive damage threshold in a PPLN ridge waveguide can be attributed to it's much stronger modal confinement compared to a PPLN channel waveguide.

In chapter 4, initially various device fabrication steps have been discussed. Then optical

characterization results of these fabricated waveguides are given. The catastrophic change in the characteristics of LiNbO<sub>3</sub> channel waveguide and better stability of guided modes in ridge waveguide have been shown experimentally at an operating wavelength of  $\lambda$  - 635 nm. Results from second harmonic generation experiments in PPLN waveguides have been thoroughly analyzed and with the help of these results the damage-resistant characteristics of PPLN ridge waveguides have been validated.

Finally, the work carried out in this thesis has been summarized and possible directions for future investigations have been outlined.

## CHAPTER 2

### Photorefractive Effect: Background Study

In this chapter, the origin of photorefractive effect and various well-known charge-transport models which are used to describe the photorefractive effect in bulk  $\text{LiNbO}_3$  have been discussed and these models have been used to estimate the effect of photorefractive damage in  $\text{LiNbO}_3$  waveguides. The charge transport-model discussed in this chapter has been used in chapter 3 to investigate the damage resistant characteristics in PPLN ridge waveguides.

#### 2.1 Physics of Photorefractive Effect

The photorefractive effect is a change in refractive index of  $\text{LiNbO}_3$  in presence of a nonuniform light intensity. It was observed for the first time by Ashkin et al. [93]. Though the photorefractive effect in  $\text{LiNbO}_3$  is attractive for memory applications [94, 95]; it is also turned out to be the main bottleneck against high power applications of nonlinear integrated optical devices. The change in optical properties of  $\text{LiNbO}_3$  during photorefractive effect is driven by the gradient of incident light intensity. An inhomogeneous light intensity of proper wavelength can cause donors species in the illuminated region of the crystal to release valance electrons, which are then elevated into the conduction band and finally get trapped by acceptor species in darker region of the crystal after being transported along the crystallographic c-axis [96]. Due to relatively longer life time of trapped charges ( $\sim$  ms), the incident light intensity needed to drive the photorefractive optical changes can be very low. The mechanism of photorefractive effect in  $\text{LiNbO}_3$  is shown in Figure 2.1. Three most important steps during the entire process are: optical absorption, charge transport, and electro-optic effect. Optical absorption and charge transport together give rise to photoconductivity, while the electro-optic effect translates the internal electric field into refractive index changes and modifies the actual index distribution of the crystal [97]. Various transition metal ions; e.g.  $\text{Fe}^{2+}/\text{Fe}^{3+}$ ,  $\text{Cu}^+/\text{Cu}^{2+}$ , and  $\text{Mn}^{2+}/\text{Mn}^{3+}$  [98] etc. or color centers ( $\sim$  ppm level) incorporated in  $\text{LiNbO}_3$  crystal during growth or waveguide fabrication act as

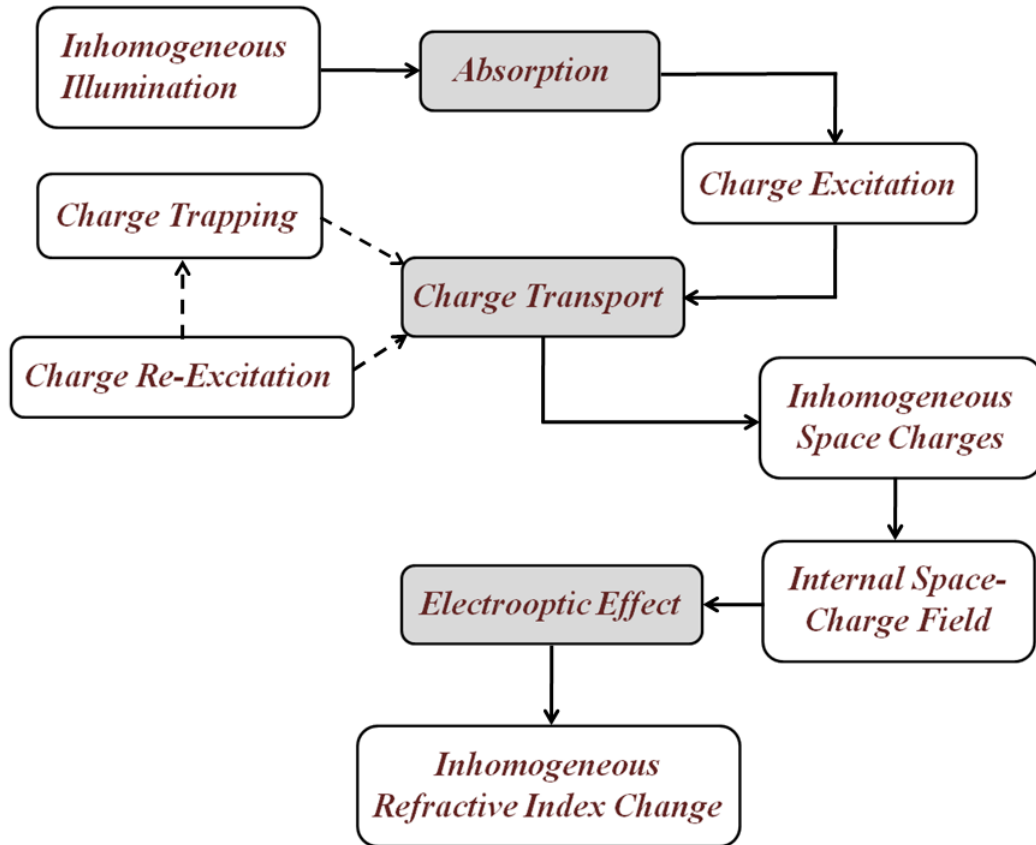


Figure 2.1: Physical mechanisms of photorefractive effect in  $\text{LiNbO}_3$ .

photorefractive centers. Here, reduced valence ions act as charge donors, whereas oxidized valence ions act as acceptors. The photorefractive change in refractive index is reversible in nature and depends on the input intensity and impurity concentrations [99, 100, 101, 102]. Photorefractive relaxation time is a measure of specific resistance of the crystal and it depends on crystal temperature [103, 104], impurity concentration and can vary from  $10^{-4}$  seconds to several months [105, 106]. The relaxation is also possible upon illumination of  $\text{LiNbO}_3$  crystal with photoactive radiation [107]. At room temperature, the persistence of the induced photorefractive damage in  $\text{LiNbO}_3$  is in general very large. Sometimes, band-to-band electron excitation induced by deep UV light [108] or sometimes X-ray [109] or  $\gamma$ -ray [110] radiation can also cause photorefraction in lithium niobate crystal.

## 2.2 Analytical Model of Photorefractive Effect

When an undoped LiNbO<sub>3</sub> crystal is illuminated with a light intensity  $\mathbf{I}$  at a particular wavelength electrons trapped at various defect/impurity levels are excited into the conduction band and a charge transport process is initiated due to bulk-photogalvanic effect, diffusion and drift process or a combination of these processes. Total photo-induced current density  $\vec{\mathbf{J}}$  in LiNbO<sub>3</sub> can be written as:

$$\vec{\mathbf{J}} = \vec{\mathbf{J}}_{\text{phg}} + \vec{\mathbf{J}}_{\text{diff}} + \vec{\mathbf{J}}_{\text{drift}} \quad (2.1)$$

Here,  $\vec{\mathbf{J}}_{\text{phg}}$  is the current density due to bulk-photogalvanic effect,  $\vec{\mathbf{J}}_{\text{diff}}$  is the diffusion current density and  $\vec{\mathbf{J}}_{\text{drift}}$  is the drift current density. Each of these current components are briefly described below:

**Bulk-photogalvanic current:** The bulk-photogalvanic effect is the most prominent effect causing photorefractive damage in lithium niobate [111]. The bulk-photogalvanic current is a light-induced current in absence of an electric field. It can be written as [112]:

$$\vec{\mathbf{J}}_{\text{phg}} = \beta \mathbf{I} \hat{c} \quad (2.2)$$

Here  $\beta$  ( $= \alpha_{33}$ ) is the bulk-photogalvanic constant and  $\alpha_{33}$  is a component of the bulk-photogalvanic tensor ( $\alpha_{ijk}$ ) of lithium niobate.  $\hat{c}$  is the crystallographic  $\mathbf{c}$ -axis and for lithium niobate  $\hat{z} \parallel \hat{c}$ . Bulk-photogalvanic current migrate charges in darker regions of the crystal resulting in the development of the space-charge field. It can also be dependent on the polarization of the incident radiation and the polarization-dependent bulk-photogalvanic current can be written as [113, 114]:

$$J_{\text{phg},i} = \sum_{j,k} \frac{1}{2} (\alpha_{ijk} E_j^* E_k + c.c.) \quad (2.3)$$

where  $\alpha_{ijk}$  are components of photogalvanic tensors. The bulk photovoltaic effect can be observed in lithium niobate both under visible and X-ray irradiation [115].

**Diffusion current:** The diffusion current is driven by concentration gradients of free charge carriers and it can be written as follows:

$$\vec{\mathbf{J}}_{\text{diff}} = -eD\vec{\nabla}n \quad (2.4)$$

where  $D$  is the diffusivity tensor and  $D=(\mu k_B T/e)$ . Here,  $e$  is the electronic charge,  $k_B$  is the Boltzmann constant and  $T$  is the crystal temperature.

**Drift current:** The drift current results from the Coulomb interaction of an electric field with various charge carriers. It can be written as:

$$\vec{J}_{\text{drift}} = e\mu n\vec{E} \quad (2.5)$$

Here,  $e$  is the electronic charge,  $\sigma$  is the conductivity,  $\mu$  is the mobility for electrons,  $n$  is the electron density in conduction band and  $\vec{E}$  is the electric field. Electric field consists of three contributions: the space charge field  $\vec{E}_{\text{sc}}$ , external electric field  $\vec{E}_{\text{ext}}$  and the pyroelectric field  $\vec{E}_{\text{pyro}}$ . Hence, Equation 2.6 can be written as:

$$\vec{J}_{\text{drift}} = e\mu n(\vec{E}_{\text{sc}} + \vec{E}_{\text{ext}} + \vec{E}_{\text{pyro}}) \quad (2.6)$$

The space charge field results from the redistribution of charge carriers and it is responsible for the photorefractive damage. The applied electric field is externally controlled. The pyroelectric field is generated due to changes in spontaneous polarization once the crystal temperature is raised during light illumination. Pyroelectric field is more prominent at higher input power and for pulsed radiations. The photorefractive space-charge field developed in lithium niobate can be obtained from the solution of Poisson's equation and the continuity equations as shown below:

$$\vec{\nabla} \cdot \vec{D} = \rho \quad (2.7)$$

and

$$\vec{\nabla} \cdot \vec{J} + \frac{\partial \rho}{\partial t} = 0 \quad (2.8)$$

### Charge transport models:

To understand the physics behind the charge-transport process and to explain various experimental results related to photorefractive effect models were developed considering generation and recombination rates of free charge carriers. At first, rate equations were developed

with considering only one set of filled and empty traps for charge carriers and the corresponding model was named as the one-center charge transport model. Different predictions of one-center model were in very good agreement with experimental results obtained at continuous wave (cw) intensities over a wide range of intensities [116]. Hence, this model became widely accepted. But, at very high light intensities experimental results showed considerable deviations from predictions of one-center charge transport model. It was subsequently observed that this anomalous behavior can be explained considering the presence of atleast one additional set of filled and empty traps for charge carriers in the charge-transport process and corresponding model was named as the two-center charge transport model. It could successfully explain various experimental results related to photorefractive effect at high light intensities. In this section one-center and two-center charge transport models have been briefly discussed along with necessary rate equations.

**(i) One-center charge transport model:** In one-center charge transport model photo-excited free electrons travel along the crystallographic z-axis from filled traps i.e.  $Fe^{2+}$ -ions (in the illuminated region) to empty traps i.e.  $Fe^{3+}$ -ions (in the dark region) according to the following scheme:



The basic scheme of one-center charge transport model has been shown in Figure 2.2 [117, 118, 119]. One-dimensional space-charge field generated in lithium niobate can be calcu-

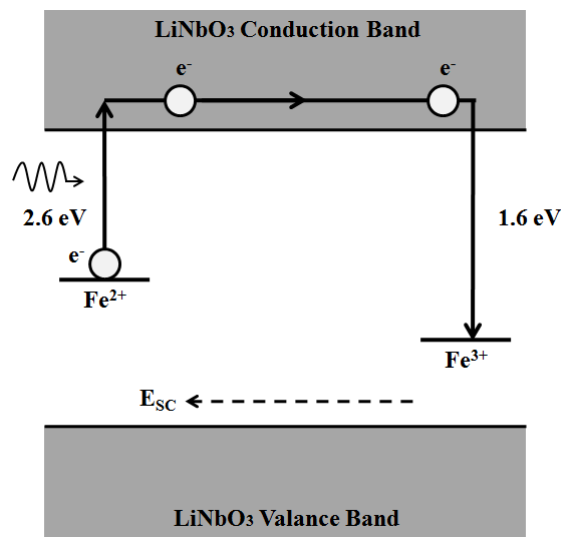


Figure 2.2: Scheme of one-center charge transport model (not in scale).



lated using following set of coupled equations (considering only one set of filled and empty traps) :

$$\frac{\partial n}{\partial t} = \frac{\partial N_{Fe}^+}{\partial t} + \frac{1}{e} \frac{\partial J}{\partial z} \quad (2.10)$$

$$\frac{\partial N_{Fe}^+}{\partial t} = q_{Fe} s_{Fe} I (N_{Fe} - N_{Fe}^+) - \gamma_{Fe} n N_{Fe}^+ \quad (2.11)$$

$$J = -e\mu n E - eD \frac{\partial n}{\partial z} + \kappa_{Fe} (N_{Fe} - N_{Fe}^+) I \quad (2.12)$$

In Equation (2.12), the electric field component  $E = E_{sc}$ , where  $E_{sc}$  is the photorefractive space-charge field (assuming that both external field and pyroelectric field are absent). The space charge field can be calculated from the following equation :

$$\frac{\partial E}{\partial z} = -e(n + N_{Fe} - N_c) / \epsilon \epsilon_0 \quad (2.13)$$

Here,  $N_c$  is the concentration of non-mobile charges which maintain the overall charge neutrality of the substrate. Using the charge conservation condition ( $\rho = 0$ ), the approximate expression for the photo-conductivity can be written as:

$$\sigma = e\mu \frac{q_{Fe} s_{Fe} I (N_{Fe} - N_c)}{\gamma_{Fe} N_c} = A \frac{(N_{Fe} - N_c)}{N_c} I = A \frac{N_{Fe}^+}{N_c} I \quad (2.14)$$

Here,  $I$  is light intensity,  $\tau_{Fe} = (I / \gamma_{Fe} N_c)$  is life time of photo-carriers in the conduction band,  $\mu$  is mobility,  $q_{Fe}$  is quantum efficiency,  $s_{Fe}$  is absorption cross-section of donor impurities,  $N_{Fe}$  and  $N_{Fe}^+ = (N_{Fe} - N_c)$  are concentrations of donors and ionized traps respectively. According to one-center charge transport model, the photoconductivity is a linear function of the light intensity and the concentration ratio of donors and traps and this relation is found to be experimentally valid over a wide range of impurity concentrations and also at low and moderate light intensities [120]. An approximate expression for the saturation refractive index change according to one-center model can be derived as follows:

$$\Delta n_{e,sat} = -\frac{1}{2} n_e^3 r \times \left[ \frac{\kappa_{Fe} (N_{Fe} - N_c)}{\sigma} \right] I \quad (2.15)$$

**(ii) Two-center charge transport model:** Two-center charge transport model was developed with the help of experimental data obtained from various  $\text{LiNbO}_3:\text{Fe}$  samples [121,

122]. The scheme of the two-center charge transport model is shown in Figure 2.3. In

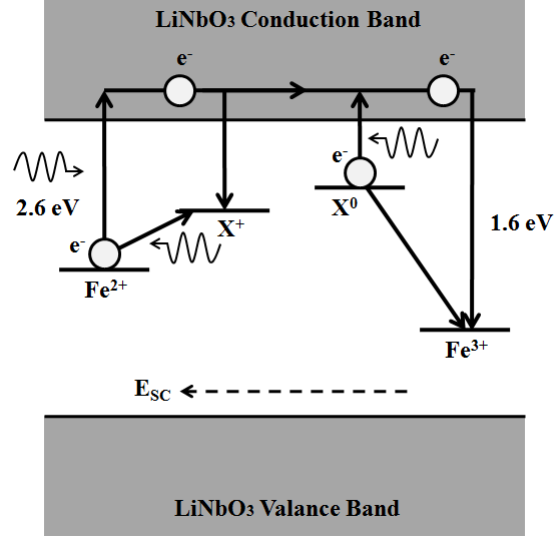


Figure 2.3: Scheme of two-center charge transport model (not in scale).

the two-center model it was assumed that  $\text{Fe}^{2+}$ -ions were donor species with a concentration  $N_{Fe}$  and  $\text{Fe}^{3+}$ -ions were acceptor species with a concentration  $N_{Fe}^+$ . The rate of light-induced excitation of electrons from the  $\text{Fe}^{2+}$ -state into the conduction band was  $q_{Fe} s_{Fe} (N_{Fe} - N_{Fe}^+) I$ , where  $s_{Fe}$  was the absorption cross-section and  $q_{Fe}$  was the quantum efficiency of transition.  $\gamma_{Fe}$  is the recombination constant of electrons. The secondary donor center (X-center) was assumed to have a concentration  $N_X$ , which becomes active at higher light intensities.  $\beta_X$  is the spontaneous ionization probability of filled X-centers. Also, it was assumed that electron can directly transfer from  $\text{Fe}^{2+}$  to  $X^+$  and from  $X^0$  to  $\text{Fe}^{3+}$  states with excitation and recombination rates as  $q_{FeX} s_{FeX} N_X^+$  and  $\gamma_{XFe}$  respectively. Equations describing the Two-center charge transport process along the crystallographic z-axis in  $\text{LiNbO}_3$  can be described using following equations [123]:

$$\frac{\partial N_{Fe}^+}{\partial t} = (q_{Fe} s_{Fe} + q_{FeX} s_{FeX} N_X^+) (N_{Fe} - N_{Fe}^+) I - [\gamma_{Fe} n + \gamma_{XFe} (N_X - N_X^+)] N_{Fe}^+ \quad (2.16)$$

$$\begin{aligned} \frac{\partial N_X^+}{\partial t} = & (\beta_X + q_X s_X I + \gamma_{XFe} N_{Fe}^+) (N_X - N_X^+) \\ & - [\gamma_X n + q_{FeX} s_{FeX} (N_{Fe} - N_{Fe}^+) I] N_X^+ \end{aligned} \quad (2.17)$$

$$\frac{\partial n}{\partial t} = \frac{\partial N_{Fe}^+}{\partial t} + \frac{\partial N_X^+}{\partial t} + \frac{1}{e} \frac{\partial J}{\partial z} \quad (2.18)$$

$$J = -e\mu n E - eD \frac{\partial n}{\partial z} + \kappa_{Fe} (N_{Fe} - N_{Fe}^+) I + k_X (N_X - N_X^+) I \quad (2.19)$$

In Equation (2.19), the electric field component  $E=E_{sc}$ , the photorefractive space-charge field. All X centers are typically ionized in dark i.e.  $N_X=N_X^+$ . The photorefractive space-charge field space charge field can be calculated from the following equation :

$$\frac{\partial E}{\partial z} = -e(N_{Fe}^+ - N_c + N_X^+ - N_X - n)/\epsilon\epsilon_0 \quad (2.20)$$

Since,  $n \ll N_{Fe}, N_X$  [124, 125], these can be omitted in the charge density expression. Also, the free electron concentration in lithium niobate does not change with time, hence using the adiabatic approximation in Equation (2.18) and then using Equation (2.16), an approximate expression of the concentration of free electrons in the conduction band can be written as follows:

$$n = \frac{q_{Fe} s_{Fe} I (N_{Fe} - N_{Fe}^+) + (\beta_X + q_X s_X I) (N_X - N_X^+)}{\gamma_{Fe} N_{Fe}^+ + \gamma_X N_X^+} \quad (2.21)$$

Using the charge conservation relation one can write that,  $\partial N_{Fe}^+ / \partial t = -\partial N_X^+ / \partial t$  and  $N_{Fe}^+ = (N_c + N_X - N_X^+)$ . With these relations Equation (2.17) can be written as:

$$\frac{\partial N_X^+}{\partial t} = \xi_1 (N_X^+)^2 + \xi_2 (N_X^+) + \xi_3 \quad (2.22)$$

where

$$\xi_1 = \gamma_{XFe} - q_{FeX} s_{FeX} I, \quad (2.23)$$

$$\xi_2 = -\beta_X - q_X s_X I - \gamma_{XFe} (N_c + 2N_X) - q_{FeX} s_{FeX} I (N_{Fe} - N_c - N_X) \quad (2.24)$$

and

$$\xi_3 = (\beta_X + q_X s_X I) N_X + \gamma_{XFe} (N_c + N_X) N_X \quad (2.25)$$

From Equation (2.17) the time evolution of the secondary shallow trap can be derived as follows (using  $N_{Fe}^+ / N_c \approx 1$ ):

$$N_X^+ = N_X - \frac{q_{FeX} s_{FeX} I (N_{Fe} - N_c) N_X}{\beta_X + \gamma_{XFe} N_c + [q_X s_X + q_{FeX} s_{FeX} (N_{Fe} - N_c)] I} \times [1 - \exp(-\{\beta_X + \gamma_{XFe} N_c + [q_X s_X + q_{FeX} s_{FeX} (N_{Fe} - N_c)] I\} t)] \quad (2.26)$$

Similarly, the time evolution of the primary acceptor state can be derived from Equation (2.26) as follows:

$$N_{Fe}^+ = N_c + \frac{q_{FeX} s_{FeX} I (N_{Fe} - N_c) N_X}{\beta_X + \gamma_{XFe} N_c + [q_X s_X + q_{FeX} s_{FeX} (N_{Fe} - N_c)] I} \times [1 - \exp(-\{\beta_X + \gamma_{XFe} N_c + [q_X s_X + q_{FeX} s_{FeX} (N_{Fe} - N_c)] I\} t)] \quad (2.27)$$

Above equations can be used to simulate the effect of an incident focused laser beam (CW) to a lithium niobate waveguide, if the beam diameter is much smaller than the width of the crystal. The steady-state value of the filled trap density  $N_X^f$  can be approximated according Equation (2.26) as follows:

$$N_X^f = N_X - \frac{\xi_2 + (\xi_2^2 - 4\xi_1 \xi_3)^{1/2}}{2\xi_1} \quad (2.28)$$

under the assumption that : the time development of the space-charge field  $E_{sc}$  is much slower than the buildup time of filled trap density  $N_X^f = (N_X - N_X^+)$ . Using the charge conservation condition, the intensity dependent photo-conductivity can be written as follows:

$$\sigma = e\mu \frac{q_{Fe} s_{Fe} I (N_{Fe} - N_c) I + [\beta_X + (q_X s_X - q_{Fe} s_{Fe}) I] N_X^f}{\gamma_{Fe} (N_c + N_X^f)} \quad (2.29)$$

The increase in photoconductivity will result in a spatially varying space-charge field within the substrate and it will change the refractive index of the substrate via electro-optic effect

according to the Equation (2.30) as shown below:

$$\Delta n_{e,sat} = -\frac{1}{2}n_e^3 r \times \left[ \frac{\kappa_{Fe}(N_{Fe} - N_C) + (\kappa_X - \kappa_{Fe})N_X^f}{\sigma} \right] I \quad (2.30)$$

Typical parameters used for calculations using in two-center charge transport model has been listed in Table 2.1.

Table 2.1: Typical parameter values for two-center charge transport model.

<b>Primary (Fe) - center parameters</b>	<b>Typical value</b>
Abs. cross-section ( $s_{Fe}$ ) [ $\text{m}^2/\text{J}$ ]	$10^{-5}$ [126]
Recomb. const. $q_{Fe}$ [ $\text{m}^3/\text{s}$ ]	$1.65 \times 10^{-14}$ [126]
Glass const. $\kappa_{Fe}$	$2.80 \times 10^{-9}$ [127]
<b>Secondary (X) - center parameters</b>	<b>Typical value</b>
Donor ( $X^0$ ) conc. [ $\text{m}^{-3}$ ]	$10^{26}$ [122]
Shallow trap ( $X^+$ ) $N_X^+$ conc. [ $\text{m}^{-3}$ ]	$10^{26}$ [122]
Thermal ionization prob. $\beta_X$ [ $\text{s}^{-1}$ ]	0 [122]
Absorption cross-section $s_X$ [ $\text{m}^2$ ]	$5.00 \times 10^{-5}$ [126]
Quantum eff. $q_X$ ( $X^+ \rightarrow \text{C.B.}$ )	$5.00 \times 10^{-16}$ [126]
Glass constant of X-center $\kappa_X$ [ $\text{m}^3/\text{V}$ ]	$42.40 \times 10^{-33}$ [122]
<b>Two - center parameters</b>	<b>Typical value</b>
Absorption cross-section ( $\text{Fe}^{2+} \rightarrow X^+$ ) $s_{FeX}$ [ $\text{m}^2$ ]	$4.00 \times 10^{-31}$ [122]
Quantum eff. of transition $q_{FeX}$	$3.22 \times 10^{-30}$ [122]
Recombination constant $\gamma_{XFe}$ [ $\text{s}^{-1}/\text{m}^3$ ]	$1.14 \times 10^{-21}$ [122]

## 2.3 Photorefraction in LiNbO<sub>3</sub> Waveguides

In telecommunication networks wavelength conversion can be easily carried out within the communication band via cascaded second-order interactions (cSHG/DFG) [128]. In this technique any two wavelengths within the communication band are chosen as the pump and the signal wave respectively. Initially a second harmonic wave is generated from the pump wave, which subsequently interacts with the signal wave via DFG to complete the conversion process. Hence, for successful wavelength conversion second harmonic generation is an inherent process to start with [129]. During QPM-SHG in PPLN waveguides very high power second harmonic waves (@  $\lambda < 900$  nm) are generated due to lower propagation

loss and very high nonlinear co-efficient ( $d_{33}$ ). Typically, lithium niobate waveguide cross-sections are relatively low ( $\sim 1.2 \times 10^{-7} \text{ cm}^2$  [4]), hence the generated intensity inside lithium niobate waveguides is very high resulting in onset of photorefractive damage almost instantly as soon as the second harmonic wave is generated. Hence, two-center charge transport model has been used to analyze the effect of photorefractive damage in lithium niobate waveguides with continuous wave illumination. For calculations, various parameters have been taken from literature [123].

Figure 2.4 shows the redistribution of primary and second traps/acceptor states in a waveguide as a function of time at different intensity level. It can be seen that for a constant incident intensity, initially  $N_{Fe}^+$  ( $N_X^+$ ) increases (decreases) with time and finally (for  $t > 10$  ms) reaches a quasi steady-state. In the quasi-steady state, any photorefractive change in the

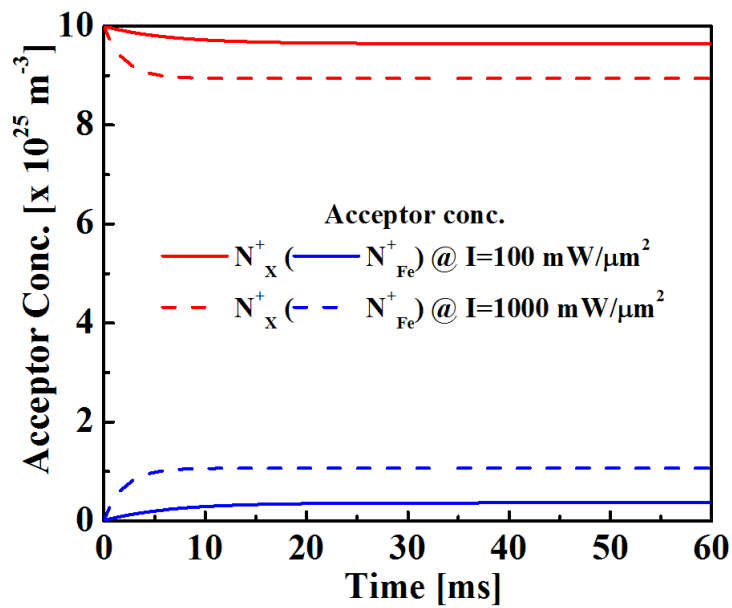


Figure 2.4: Evolution of primary and secondary acceptor concentrations as a function of time for different incident intensities of laser light ( $\lambda \sim 488 \text{ nm}$ ).

waveguide is mainly controlled by the intensity  $I$  of the incident radiation and the device operating temperature. Higher value of the incident radiation shows larger change in the waveguide.

Figure. 2.5 shows the intensity dependent change in the steady-state photo-conductivity in the waveguide with different impurity concentrations [122]. From the figure it can be

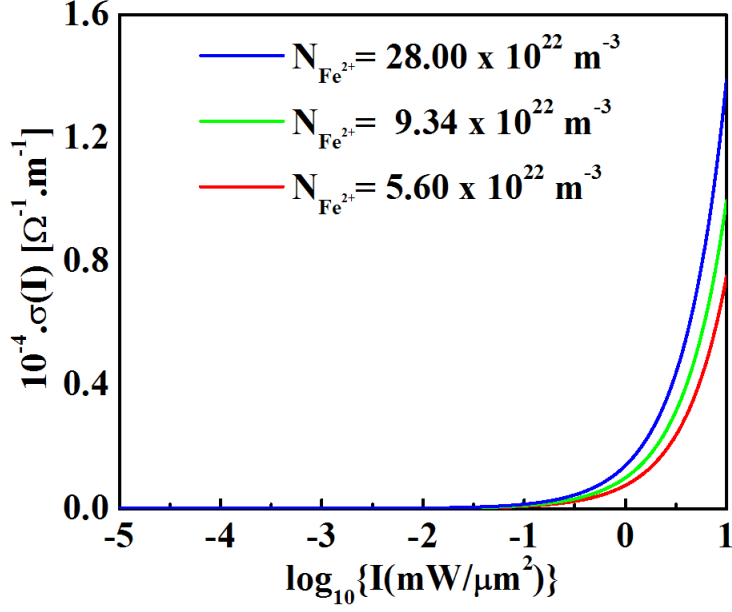


Figure 2.5: Intensity dependent change in photo-conductivity  $\sigma(I)$ .

understood that as the photo-conductivity increases, more free carriers (electrons) are transported from the illuminated region substrate to the dark region. If the impurity concentration is higher in the substrate it results in even larger increase in the photo-conductivity. The photoconductivity creates a spatially inhomogeneous charge-distribution and finally a space-charge field is created within the substrate which changes the local refractive index within the waveguide via electro-optic effect. Figure 2.6 shows the typical variation of the saturation photorefractive index change ( $\Delta n_{e,sat}$ ) as a function of the incident intensity  $\mathbf{I}$  for different impurity levels. The saturation refractive index change inside a waveguide can increase with the increase in the input intensity, resulting in higher photorefractive damage. For a fixed intensity inside a waveguide, the photorefractive index change can be higher if the impurity concentration is higher within the substrate, hence the photorefractive damage in a waveguide is also dependent on the property of the substrate material (e.g. impurity concentration etc.). Figure 2.6 gives a typical idea of the optical damage threshold present in LiNbO<sub>3</sub> waveguides. With the help of this idea waveguides can be designed to obtain better stability against photorefractive damage.

In a Ti-indiffused waveguide the original refractive index profile can be defined as:

$$n_W(x, y) = n_{bulk,air}(x, y) + \Delta n^{Ti}(x, y) \quad (2.31)$$

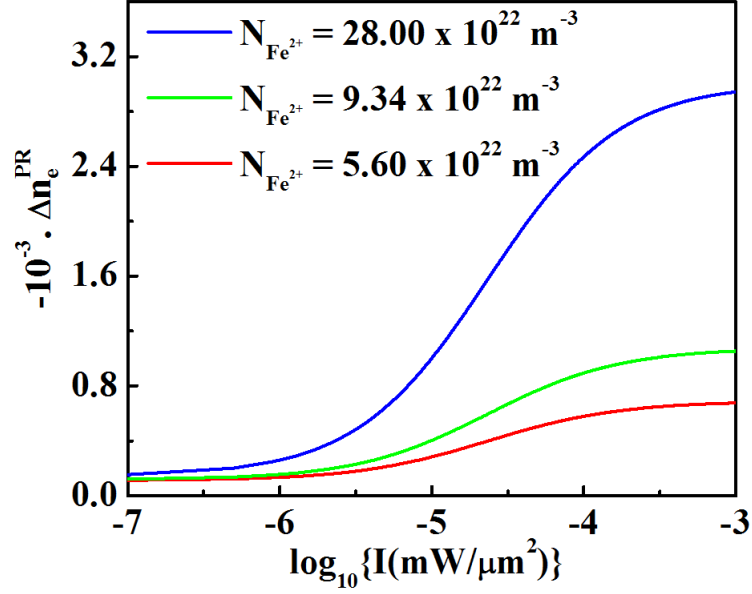


Figure 2.6: Variation of  $\Delta n_{e,sat}$  as a function of  $\log_{10}[I(\text{mW}/\mu\text{m}^2)]$  in  $\text{LiNbO}_3$ .

where  $\Delta n^{Ti}(x, y)$  is change in refractive index due to Ti-indiffusion in the waveguide region. In presence of a photorefractive incident radiation ( $\lambda_{PR}$ ), the changed refractive index profile in the waveguide region becomes:

$$n_{PRW}(x, y) = n_{bulk,air}(x, y) + \Delta n^{Ti}(x, y) - \Delta n^{PR}[I_{\lambda_{PR}}(x, y)] \quad (2.32)$$

Here,  $\Delta n^{PR}[I_{\lambda_{PR}}(x, y)]$  is the refractive index change due to  $I_{\lambda_{PR}}(x, y)$ . The ultimate change in refractive index can be calculated accurately by updating the intensity profile of the guided mode in an iterative manner. The photorefractive damage becomes stronger at shorter wavelengths [130, 131].

## 2.4 Conclusions

In this chapter, the origin of the photorefractive effect and different photorefractive charge-transport models in lithium niobate have been briefly discussed. Then time-evolution acceptor (both primary and secondary) concentrations as a function of the incident intensity, intensity dependent change in photo-conductivity at various impurity levels have been studied. Finally, the effect of photorefractive damage in lithium niobate waveguide i.e. an intensity



dependent change in extra-ordinary refractive index have also been studied using two-center charge transport model. Various parameters used for the calculation were obtained from the literature [122] meant for an incident wavelength  $\lambda = 488$  nm, which is close to the peak wavelength of  $\text{Fe}^{2+}$  absorption spectrum ( $\lambda \sim 470$  nm). Hence, without loss of generality it can be assumed that the photorefractive index change is of the same order for a given wavelength in both  $\text{LiNbO}_3$  channel and ridge waveguides. With the knowledge of the intensity dependent change in refractive index, Ti-indiffused ridge waveguide geometry have been optimized in the following chapter such that it can withstand against the so called photorefractive damage.

## CHAPTER 3

### Damage Resistance in PPLN Ridge Waveguides

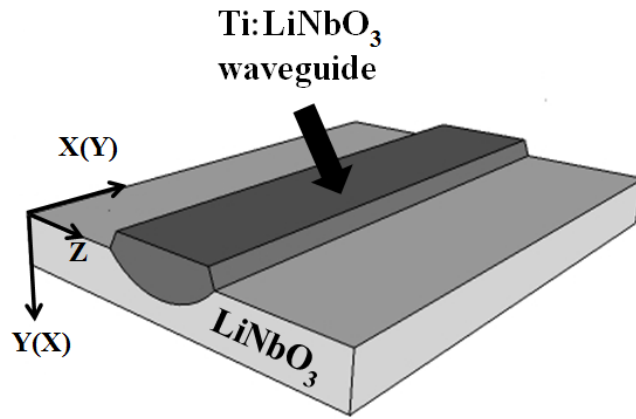
A theoretical investigation has been carried out in this chapter in an effort to justify the superiority of photorefractive damage resistance of guided modes in ridge waveguide. The PPLN ridge waveguide has been chosen for the second harmonic (SH) generation via QPM process operating at  $\lambda \sim 1550$  nm. It is worth to mention here that the harmonic generation (visible wavelength range) in PPLN devices is responsible for photorefractive damage. Initially the geometry of a Ti-indiffused ridge waveguide has been optimized for highly efficient second harmonic generation. Then with the knowledge of the intensity dependent refractive index change in lithium niobate according to two-center model, modal characteristics of PPLN waveguides have been studied in presence of second harmonic generation. It has been observed that modal properties of a Ti-indiffused ridge waveguide with an optimized geometry are more tolerant against small photorefractive changes or these waveguides are photorefractive damage resistant in nature.

### 3.1 Waveguide Design

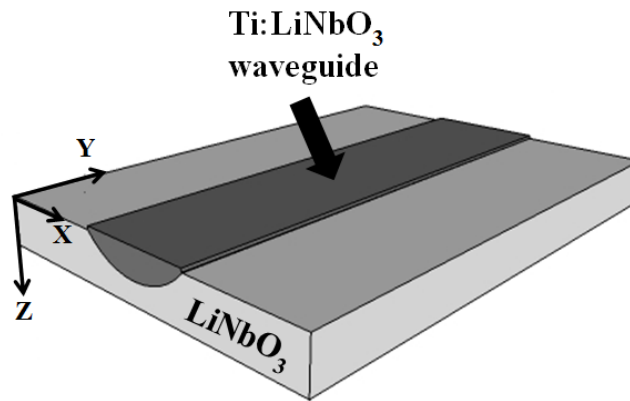
In the present work Ti-indiffused ridge waveguides have been investigated and results were compared with those from channel waveguides having similar diffusion parameters. Ti-indiffusion process was carried out at a temperature  $\sim 1060^\circ$  C for  $\sim 8.5$  hour in an inert environment. Various fabrication parameters (e.g. waveguide width, effective depth, and peak index change) were controlled to design and fabricate single-mode waveguides with minimum waveguide-fiber coupling loss [132, 133].

#### 3.1.1 Single mode guidance

Schematics of LiNbO<sub>3</sub> ridge and channel waveguides are shown in Fig. 3.1a and Fig. 3.1b, respectively. Lithium niobate channel waveguides used in various nonlinear applications



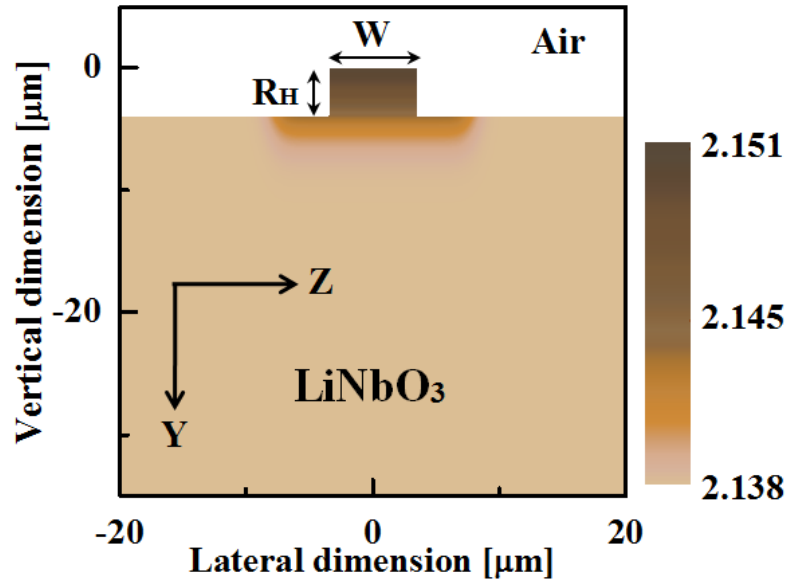
(a)



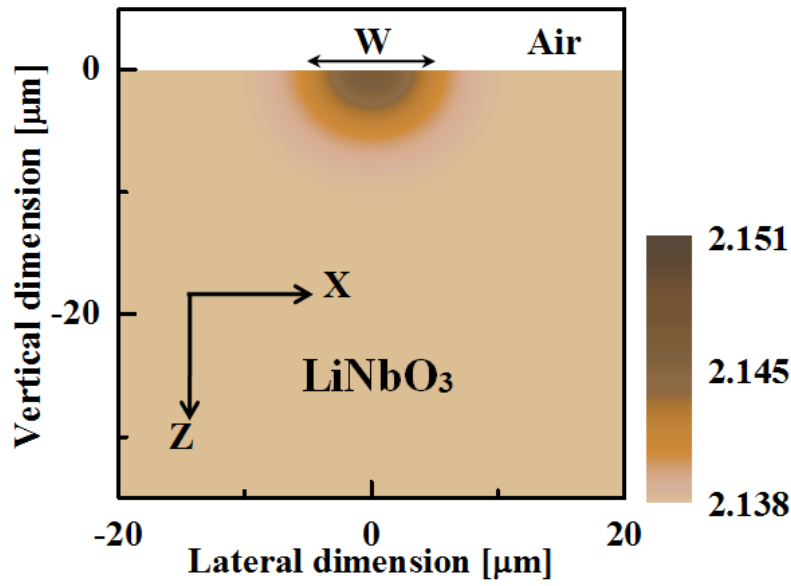
(b)

Figure 3.1: Schematic of  $\text{LiNbO}_3$  waveguides along with crystallographic axes : (a) ridge waveguide, (b) channel waveguide.

are fabricated on crystallographic  $-Z$  surface of a  $Z$ -cut lithium niobate substrate on crystallographic  $-Z$  surface, where ridge waveguides are fabricated on  $X$ -( $Y$ -) substrates so that the largest nonlinear coefficient ( $d_{33}$ ) can be used for most efficient nonlinear interactions, which is oriented along crystallographic  $Z$ -axis. During Ti-indiffusion, in case of ridge waveguide the Ti-ion distribution diffuses only vertically downwards within the ridge region due to the physical boundary, and subsequently beyond the ridge region it may spread along the lateral direction too. For channel waveguides the Ti-distribution spreads both in lateral as well as in the vertical direction. Refractive index profiles of lithium niobate waveguides can be well-approximated by mathematical function with an assumption that the diffusion



(a)



(b)

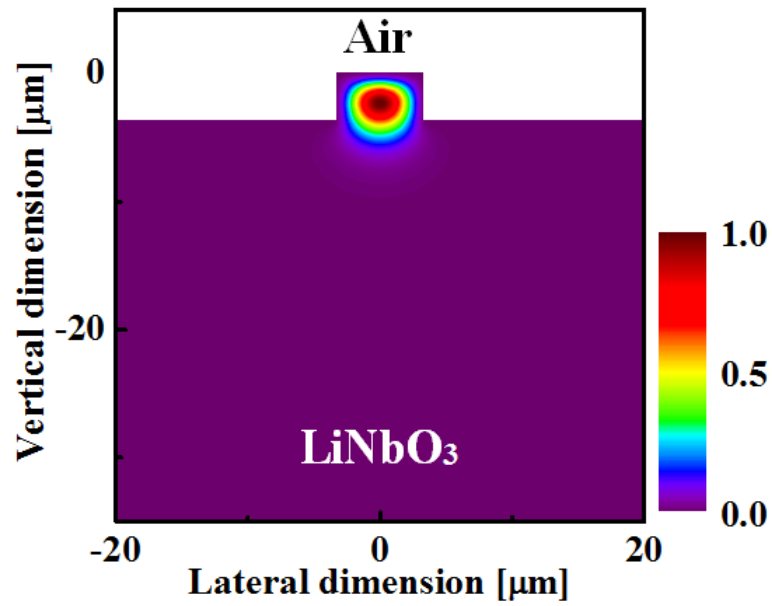
Figure 3.2: Extraordinary index distribution of LiNbO<sub>3</sub> (a) ridge waveguide (Y-cut, X-propagating,  $R_H$  - 4  $\mu\text{m}$ ,  $W$  - 7  $\mu\text{m}$ ) and (b) channel waveguide (Z-cut, Y-propagating,  $W$  - 7  $\mu\text{m}$ ) for Ti-layer thickness - 100 nm, diffusion duration of 8.5 hours at 1060° C.

time is long enough to diffuse all Ti-atoms into the substrate. For a ridge waveguide, within the ridge region the profile is linear with Ti-concentration decreasing downwards, whereas

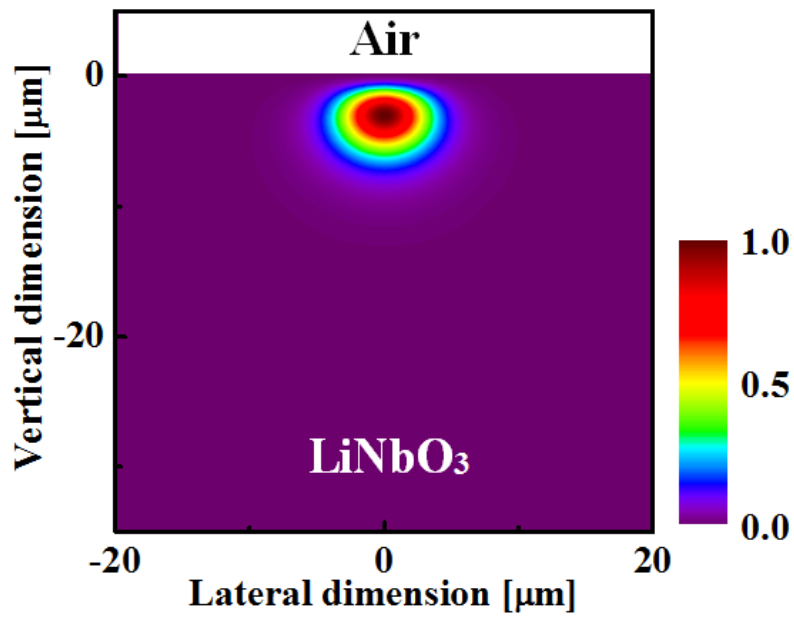
beyond the ridge region it can be approximated by the sum of error functions laterally and by a Gaussian function perpendicular to the substrate surface. Similarly, for the channel waveguide it is approximated by a sum of error functions laterally and by a Gaussian function vertically. The refractive index profile in a Ti-indiffused waveguide (Ridge/Channel) can be defined as:

$$n_W(x, y) = n_{bulk,air}(x, y) + \Delta n^{Ti}(x, y) \quad (3.1)$$

where  $\Delta n^{Ti}(x, y)$  is change in refractive index in the waveguide region due to Ti-indiffusion. Typical refractive index profile for a ridge waveguide (Y-cut crystal and X-propagating) of ridge height  $R_H$  and that of a channel waveguide (Z-cut crystal and Y-propagating) have been shown in Fig. 3.2a and Fig. 3.2b. Diffusion parameters used for this calculation are: Ti-layer thickness - 100 nm, diffusion time - 8.5 hour, temperature - 1060 °C. For the given diffusion parameters the vertical diffusion depth of 4.3  $\mu\text{m}$  (5.0  $\mu\text{m}$ ) is obtained for ridge (channel) waveguide configuration and the corresponding maximum surface refractive index change is found to be  $\sim 1.2 \times 10^{-2}$  ( $0.8 \times 10^{-2}$ ) at an operating wavelength  $\lambda$  - 1550 nm. Here, only the change in the extraordinary refractive index change is estimated as the extra-ordinary polarized light is used in majority of PPLN nonlinear integrated optical devices. For a ridge waveguide, the waveguide  $W$  is width of the ridge structure, but for channel waveguide we have defined it by the width of deposited Ti-film used for indiffusion. Detailed mathematical relations used for the calculation are given in the literature [134]. Guided fundamental modes (@  $\lambda \sim 1550$  nm) of a ridge waveguide ( $W$  - 7  $\mu\text{m}$ ,  $R_H$  = 4  $\mu\text{m}$ ) and channel waveguide ( $W$  - 7  $\mu\text{m}$ ) are shown in Figure 3.3. The  $1/e^2$  mode-size for TE-polarized (TM-polarized) fundamental mode at  $\lambda$  - 1550 nm for the ridge (channel) waveguide are estimated to be  $\sim 5.5 \mu\text{m} \times 5.3 \mu\text{m}$  ( $9.5 \mu\text{m} \times 6.8 \mu\text{m}$ ). Which clearly shows that even for similar fabrication parameters the mode size of the ridge waveguide is much smaller compared to the mode size of the channel waveguide. Figure 3.4 shows width dependent dispersion curves for both channel and ridge waveguides. From dispersion curves it is observed that for the ridge waveguide single-mode cut-off width  $\sim 10 \mu\text{m}$ , whereas for the channel waveguide single mode cut-off width  $\sim 8 \mu\text{m}$ . The single mode guided region is of great interest because almost all integrated optical devices are designed to sustain only the fundamental mode for their efficient operations and better coupling efficiency with optical fibers. Since, the ridge waveguide is having larger single-mode guidance region it



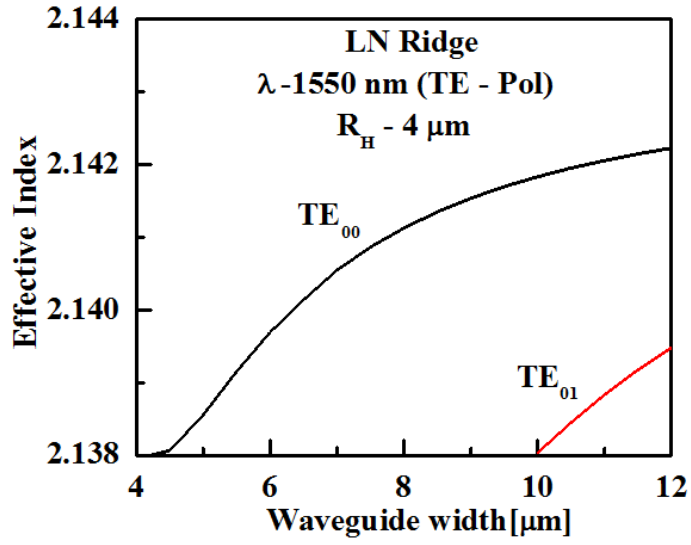
(a)



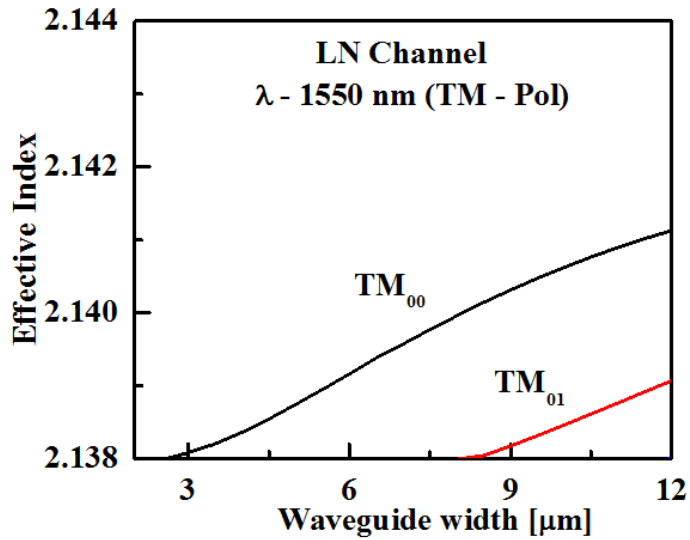
(b)

Figure 3.3: Intensity distributions of guided fundamental modes for : (a) ridge waveguide ( $R_H - 4 \mu\text{m}$ ,  $W - 7 \mu\text{m}$ ) and (b) channel waveguide ( $W - 7 \mu\text{m}$ ) at  $\lambda - 1550 \text{ nm}$ .

is more suitable to use ridge waveguides for the design and development of various novel integrated optical devices. From the modal dispersion curves it is also observed that effec-



(a)

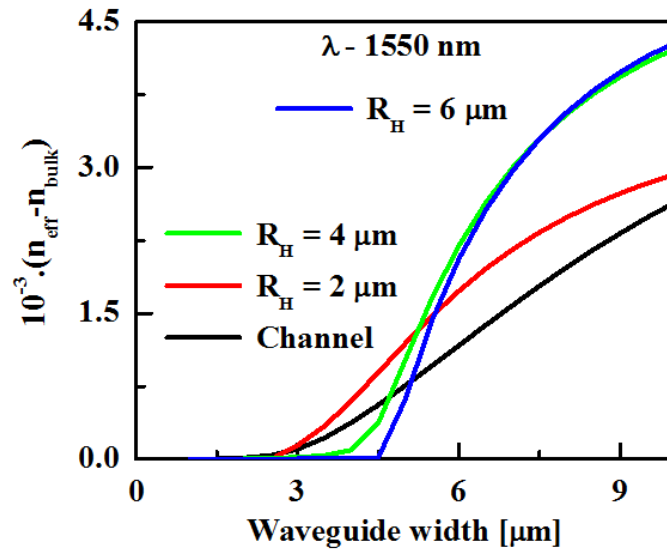


(b)

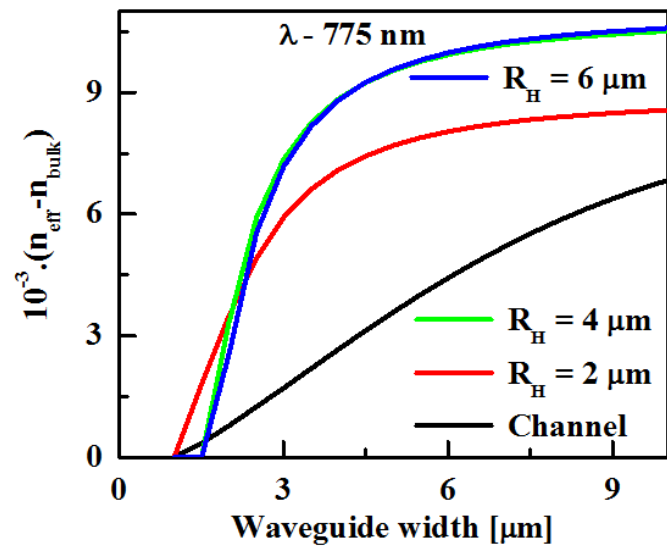
Figure 3.4: Modal dispersion for LiNbO<sub>3</sub> waveguides: (a) ridge ( $R_H - 4 \mu\text{m}$ ) and (b) channel. Calculations are carried out for TE- (TM-) mode in case of ridge (channel) waveguide which is used to avail the highest nonlinear coefficient ( $d_{33}$ ) for wavelength conversions.

tive indices of ridge waveguides are much higher compared to effective indices of channel waveguides. Figure 3.5 shows the variation of  $n_{eff} - n_{bulk}$  as a function of waveguide width for guided fundamental modes at  $\lambda - 1550 \text{ nm}$  and its second harmonic wavelength

at  $\lambda - 775$  nm, respectively, by taking ridge height  $R_H$  as a parameter. It is seen that index



(a)



(b)

Figure 3.5: Effective index contrast with respect to bulk for the guided fundamental mode as a function of waveguide width for varying ridge heights :(a)  $\lambda - 1550$  nm, (b)  $\lambda - 775$  nm. Calculations are carried out for TE- (TM-) mode in case of ridge (channel) waveguide which is used to avail the highest nonlinear coefficient ( $d_{33}$ ) for wavelength conversions.

contrast for both the pump mode as well as the second harmonic mode are much higher in



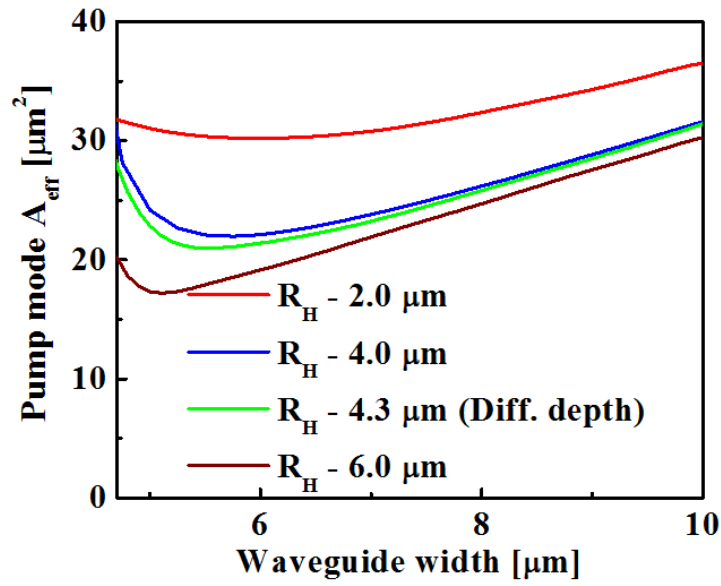
case of ridge waveguide compared to channel waveguides. The tighter modal confinement in ridge structure is mainly attributed to The higher value of  $(n_{eff} - n_{bulk,air})$  in case of ridge waveguide can be attributed to it's tighter modal confinement and hence smaller mode size. The value of  $(n_{eff} - n_{bulk})$  is found to increase for the ridge waveguide to its maximum for  $R_H \sim 4 \mu\text{m}$ , which is close to the Ti-diffusion depth in vertical direction. Similar plots for the channel waveguide much weaker index contrast, which clearly explains weak modal confinement of channel waveguides compared to an optimized ridge waveguide structure. Higher effective index contrast also suggests for a better modal stability in case of ridge waveguides.

### 3.1.2 Effective mode area

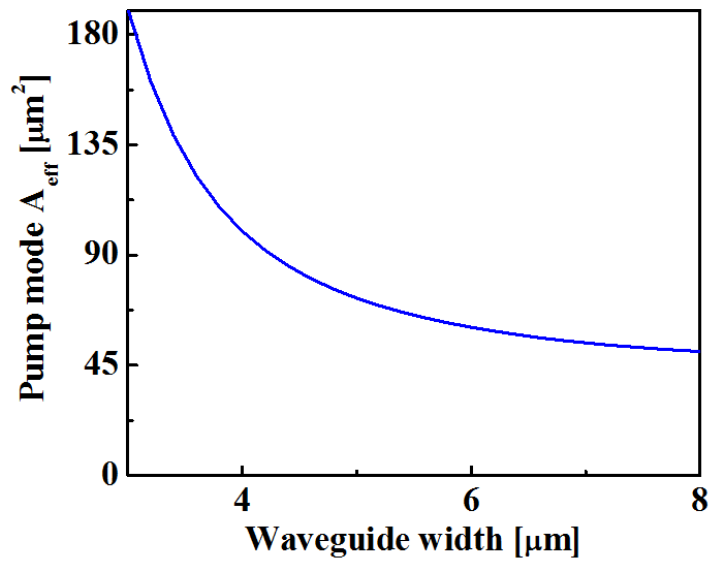
For efficient operation of nonlinear integrated optical devices smaller waveguide mode dimensions are essential. Waveguide mode size can be optimized by varying various waveguide fabrication parameters. In the present work, the width of the Ti-strip has been varied and corresponding effective mode area ( $A_{eff}$ ) has been calculated at  $\lambda \sim 1550 \text{ nm}$  to determine the optimum mode size using the formula as shown below:

$$A_{eff} = \frac{[\iint e^2(x, y) dx dy]^2}{[\iint e^4(x, y) dx dy]} \quad (3.2)$$

Here  $e(x,y)$  is the electric field profile of the propagating waveguide mode. Lower value of  $A_{eff}$  leads to the tighter modal confinement and stronger overlap between various interacting waves during nonlinear interactions. Figure 3.6 shows the effective area of the pump wave mode as a function of the waveguide width for both lithium niobate ridge (Figure 3.6a) and channel (Figure 3.6b) waveguides within their range of operation under single mode condition. In case of lithium niobate ridge waveguide, effective mode area of the pump wave is relatively larger for the smaller value of ridge height ( $R_H$ ), and it is progressively reduced with the increase in ridge height. But, for  $R_H >$  vertical diffusion depth ( $\sim 4.3 \mu\text{m}$  for used set of parameters), the value of the effective mode area of the pump wave nearly saturates. For similar set of fabrications parameters it has been observed that the effective mode area for the pump wave is always much larger in case of channel waveguide, which implies that it is always possible to achieve better modal confinement hence improved nonlinear



(a)



(b)

Figure 3.6: Effective mode area ( $A_{eff}$ ) for the pump mode :(a) ridge, (b) channel for Ti-layer thickness - 100 nm, diffusion time- 8.5 hours, temperature - 1060° C. Calculations are carried out for TE- (TM-) mode in case of ridge (channel) waveguide which is used to avail the highest nonlinear coefficient ( $d_{33}$ ) for wavelength conversions.

interactions using ridge waveguides. For the present work, channel waveguide width  $\sim 7 \mu\text{m}$  has been used (standard waveguide width used for all  $\text{LiNbO}_3$  integrated optical devices fabricated using channel waveguides for efficient coupling with standard single-mode fiber at 1550 nm). For comparison purpose, the width of the ridge waveguide is also considered as  $7 \mu\text{m}$  and the ridge height is kept as  $4 \mu\text{m}$  (so that the mode can be confined within the ridge structure).

### 3.2 QPM-Second Harmonic Generation

Nonlinear optics deals with the nonlinear interactions of light with matter. When a beam of light passes through a material, it interacts with individual atoms and molecules and polarizes them. If the intensity of the input beam is large and comparable to the electric field binding electrons to the nucleus of atoms or molecules, the response of dipoles to the input optical field becomes nonlinear and dipoles begin to oscillate anharmonically. As a result these dipoles generate an optical field having a frequency different from that of the incident field. In a source-free ( $\rho = 0$ ), linear, isotropic, homogeneous, lossy ( $\sigma \neq 0$ ) nonlinear dielectric medium the light-matter interaction can be described by the following equation:

$$\nabla^2 \vec{E} - \mu_0 \epsilon \frac{\partial^2 \vec{E}}{\partial t^2} - \mu_0 \sigma \frac{\partial \vec{E}}{\partial t} - \mu_0 \frac{\partial^2 \vec{P}_{NL}}{\partial t^2} = 0 \quad (3.3)$$

Here,  $\vec{P}_{NL}$  is the nonlinear polarization term,  $\epsilon$  is the permittivity of the medium,  $\mu_0$  is the permeability of the free space. The polarization term induced by the second-order nonlinear interactions are much stronger compared to other higher order terms. Hence, the nonlinear polarization term can be written as:

$$\vec{P}_{NL} = \epsilon_0 [\chi^{(2)} \vec{E} \vec{E}] \quad (3.4)$$

Second order nonlinear interactions are observed in non-centrosymmetric crystals. Second harmonic generation (SHG) is one of the basic second-order nonlinear interaction. During, SHG two photons having same polarization at a frequency  $\omega_p$  (pump frequency) combine and generate one photon with the same polarization at a second harmonic frequency  $\omega_{SH}$  ( $=2\omega_p$ ). This process is known as the type-zero phase matching in literature. Using the

slowly varying envelope approximation, coupled-mode equations for second harmonic generation can be written as:

$$\frac{\partial A_P}{\partial z} + \frac{\alpha_P}{2} A_P + j\sqrt{\eta} A_P^* A_{SH} \cdot \exp[-j\Delta k_{SHG}z] = 0 \quad (3.5a)$$

and

$$\frac{\partial A_{SH}}{\partial z} + \frac{\alpha_{SH}}{2} A_{SH} + j\sqrt{\eta} A_P A_P \cdot \exp[j\Delta k_{SHG}z] = 0 \quad (3.5b)$$

$$\eta = \frac{k_P^2}{\lambda_P^2} = \frac{8\pi^2}{\epsilon_0 c} \left[ \frac{d_{eff}^2}{n_P^2 n_{SH} \lambda_P^2 A_{eff}^{(2)}} \right] \quad (3.5c)$$

and

$$S_{eff}^{(2)} = \frac{\left[ \int_{-\infty}^{\infty} \int_{-\infty}^{\infty} |e_P(x, y)|^2 dx dy \right]^2 \left[ \int_{-\infty}^{\infty} \int_{-\infty}^{\infty} |e_{SH}(x, y)|^2 dx dy \right]}{\left[ \int_{-\infty}^{\infty} \int_{-\infty}^{\infty} e_P(x, y) e_{SH}(x, y) e_P(x, y) dx dy \right]^2} \quad (3.5d)$$

In above equations  $A_P$ ,  $A_{SH}$  are normalized complex amplitudes of the pump and the second-harmonic wave respectively.  $\alpha_P$  and  $\alpha_{SH}$  are propagation-loss for the pump and the second harmonic wave respectively.  $\Delta k_{SHG} = k_{SHG} - 2k_P$  is the phase-mismatch during second harmonic generation.  $d_{eff}$  is the effective nonlinear coefficient for second harmonic generation, which depends on the material property and polarization of the pump wave.  $\eta$  is the normalized conversion efficiency for the second harmonic generation. Wavelength dispersion in lithium niobate waveguides causes variations in both pump and second harmonic refractive indices, thereby making  $\Delta k_{SHG} \neq 0$  in a waveguide. Hence, the phase relationship between these two waves changes continuously as a function of position and consequently the direction of power flow also follows the same. But, an efficient and steady growth of the second harmonic power needs a continuous conversion of the pump power into the second harmonic power. This can be accomplished in  $\text{LiNbO}_3$  waveguides by compensating the phase-velocity mismatch between the pump wave and the second harmonic wave using quasi-phase matching (QPM) [135]. Here, the largest nonlinear coefficient,  $d_{33}$  is used for the phase-matching by aligning all interacting waves along crystallographic z-axis

and hence achieving the highest possible conversion efficiency. In this technique, initially the pump and the second harmonic waves are allowed to propagate along the waveguide in a non-phased-matched fashion, till the point where the accumulated phase mismatch between these two waves reaches a value  $\pi$ , and then immediately the sign of the nonlinear coefficient  $d_{33}$  is reversed and the interacting waves are forced to interfere constructively. For steady growth of the second harmonic wave, this periodic modulation of the nonlinear coefficient is carried out along the entire waveguide length and a  $d_{33}$  grating is formed along the waveguide length. This QPM grating introduces an additional phase-term  $K_{QPM}$  in the phase mismatch equation as shown in Equation (3.6):

$$\Delta k_{QPM} = \Delta k_{SHG} - K_{QPM} = (k_{SH} - 2k_P) - K_{QPM} \quad (3.6)$$

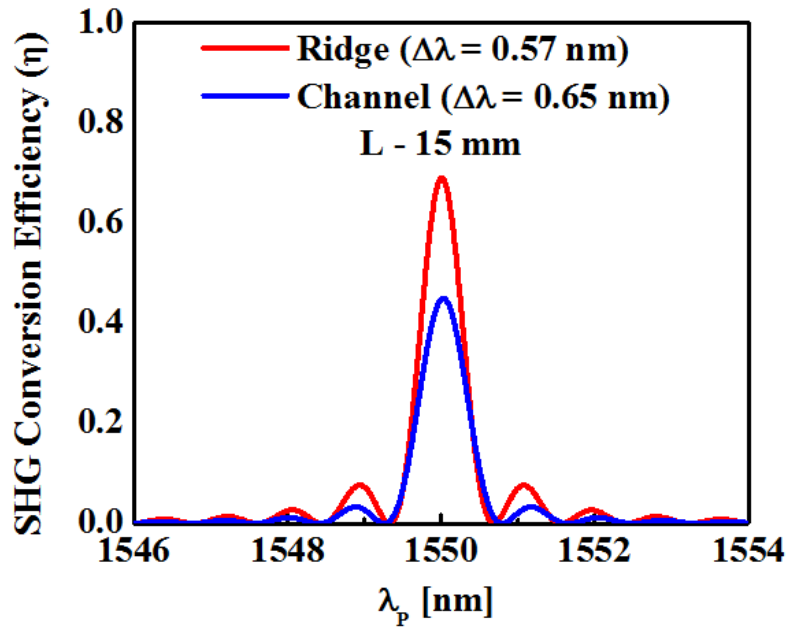
where, there term  $K_{QPM} = (2\pi m/\Lambda_{QPM})$  compensates for the phase-mismatch during second harmonic generation. Here “m” is the order of the QPM-grating,  $\Lambda_{QPM} = 2l_c$  is the grating period and  $l_c$  is the coherence length, the distance over which both the pump and the second harmonic wave propagate in the same direction. The effective nonlinear co-efficient  $d_{eff}$  in a QPM-lithium niobate waveguide with first order grating structure can be written as:

$$d_{eff} = \frac{2}{\pi} d_{33} \quad (3.7)$$

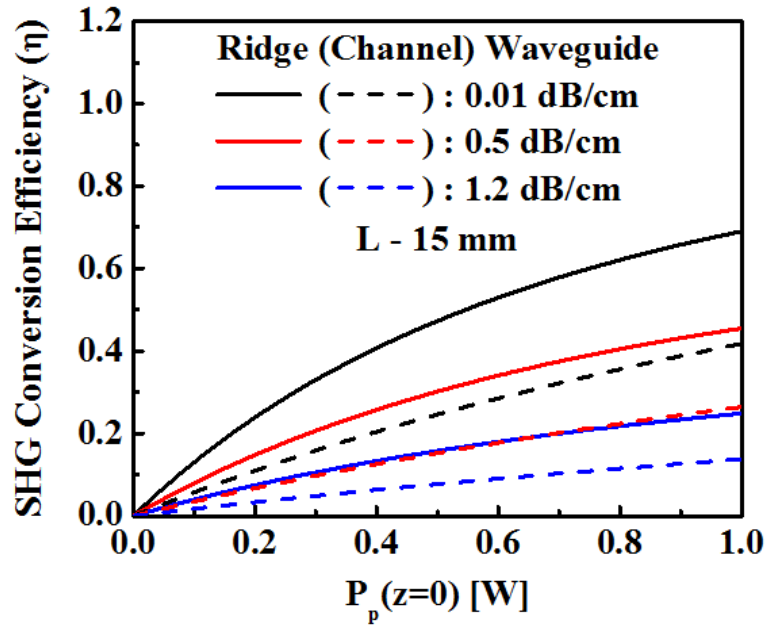
where  $d_{33}$  is the nonlinear co-efficient of lithium niobate within the waveguide. The QPM-SHG was quantitatively investigated with the help of coupled mode equations as shown in Equation (3.5). Here pump ( $A_P$ ) and second harmonic ( $A_{SH}$ ) wave amplitudes are normalized such that the power in each wave  $P_i = |A_i|^2$ , where  $i=P, SH$ .  $\alpha_P, \alpha_{SH}$  are waveguide propagation losses for the pump power as well as the second harmonic power respectively,  $\Delta k_{QPM}$  is the phase-mismatch for QPM-SHG and  $\eta_0 [W^{-1}.m^{-2}]$  is the normalized conversion efficiency which depends on pump wavelength  $\lambda_P$ , effective refractive indices of pump ( $n_{eff,P}$ ) and second harmonic ( $n_{eff,SH}$ ) modes, effective nonlinear coefficient  $d_{33} = 13.1$  pm/V [136] and the effective area (overlap) of interacting modes  $S_{eff}^{(2)}$ .

$$\eta_0 = \left[ \frac{8d_{eff}^2 \pi^2}{\varepsilon_0 c n_{2\omega} n_{\omega}^2 \lambda_{\omega}^2 S_{eff}^{(2)}} \right] \quad (3.8)$$

$e_p^2(x,y)$  and  $e_{SH}^2(x,y)$  are intensity distributions of guided pump and second harmonic modes, respectively. The quasi phase-matched condition is achieved by a periodic ferroelectric domain inversion with a periodicity of  $\Lambda = \lambda_p / [2(n_{eff,SH} - n_{eff,P})]$ . The peak second harmonic conversion efficiency in a waveguide of length  $L$  is defined as  $\eta_{SH} = [P_{SH}(L)/P_{P,coup}(0)]$ . Since guided modes are tightly confined in ridge waveguides, a better non-linear optic interaction is expected when it is compared to typical channel waveguides. The smaller effective area  $S_{eff}$  in the ridge waveguide is attributed to the tighter modal confinements and better overlap of pump and second harmonic guided modes; it is mainly responsible for the higher SHG efficiency in ridge guides even for higher propagation losses. Fig. 3.7a shows the SH-conversion efficiency  $\eta = P_{SH}(z = L)/P_p(z = 0)$  vs. pump wavelength  $\lambda_p$  plot for Ti:PPLN waveguides (channel and ridge) of same length,  $L = 15$  mm and same propagation loss ( $\alpha_p = \alpha_{SH} = 0.01$  dB/cm) for a given coupled pump power  $P_p(z = 0) = 1$  W. From Fig. 3.7a it can be observed that the conversion efficiency for second harmonic generation in a PPLN ridge waveguide is much higher compared to a channel waveguide and also the band-width (FWHM) of the phase-matching curve is narrower in case of the ridge waveguide. Fig. 3.7b shows the SH- conversion efficiency as a function of coupled pump power  $P_p(z = 0)$  under phase-matching condition ( $\Delta\beta_{SHG} = 0$ ), with waveguide propagation loss ( $\alpha_p = \alpha_{SH}$ ) as the parameter. It can be seen that even with increasing propagation loss the generated second harmonic power will be always higher in case of ridge waveguide due to its higher conversion efficiency. In ridge waveguides, tighter modal confinement and better overlap of pump and second harmonic guided modes is responsible for higher SH- conversion efficiency even with higher propagation losses. Figure 3.8 shows calculated second harmonic conversion efficiency as a waveguide length for PPLN channel and ridge waveguides assuming waveguide loss as a parameter. From the figure it is seen that for the similar propagation loss, the second harmonic conversion efficiency in case of ridge waveguide is always higher compared to a PPLN channel waveguide of same length. Hence it is possible to achieve a similar level of second harmonic conversion efficiency as in case of a PPLN channel waveguide using a PPLN ridge waveguide of smaller length.



(a)



(b)

Figure 3.7: Calculated (a) SH- conversion efficiency ( $\eta$ ) vs. pump wavelength ( $\lambda_p \sim 1550$  nm), (b) SHG conversion efficiency ( $\eta$ ) vs. coupled pump power  $P_p(z = 0)$  for Ti:PPLN channel and ridge waveguides.

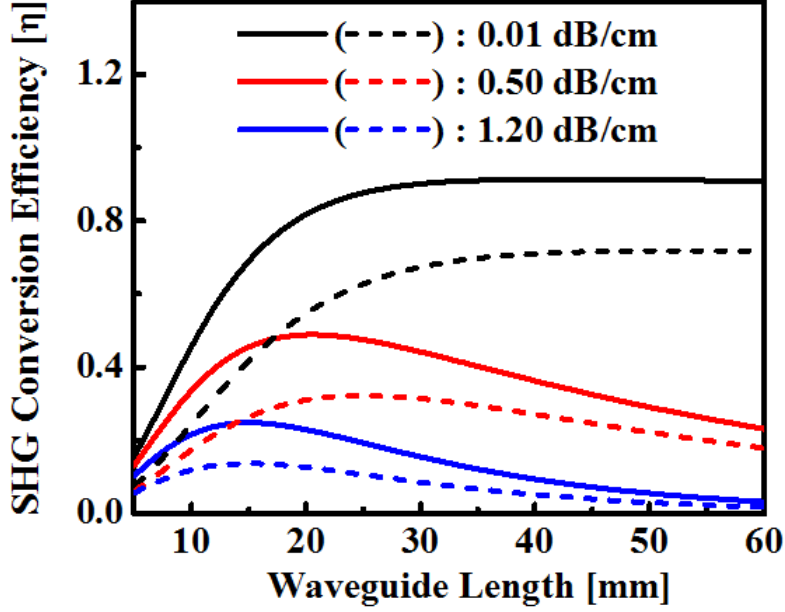


Figure 3.8: Second Harmonic Conversion efficiency as a function of waveguide length.

### 3.3 Modal Stability in Ridge Waveguides

In this section, we have theoretically analyzed modal stabilities of single-mode Ti-indiffused ridge and channel waveguides at communication wavelengths ( $\lambda \sim 1550$  nm) by evaluating eigen modes under the influence of photorefractive effect in presence of second harmonic waves ( $\lambda \sim 775$  nm). We have also investigated photorefractive induced detuning of phase matching wavelengths as a function of generated second harmonic powers for PPLN waveguides with a quasi phase-matched period of  $\Lambda \sim 16.1$   $\mu\text{m}$ .

**Intensity dependent photorefraction :** Photorefractive effect is an inherent property of  $\text{LiNbO}_3$ , but the actual strength of photorefractive effect depends also on the concentration of defect and/or trap states present in the crystal. Various experimental results suggest mainly the  $\text{Fe}^{2+}$  and  $\text{Fe}^{3+}$  ions serve as defect- and trap-states, respectively. When  $\text{LiNbO}_3$  is exposed to intense laser beams in the visible and near infrared regions, electrons are photo-excited (from defect states) into the conduction band in bright regions and then migrate into the dark areas and subsequently captured by trap states. A net amount of charge transport in any direction is determined by the photovoltaic tensor [121]. In  $\text{LiNbO}_3$ , light induced photorefractive effects have been observed for both ordinary ( $n_o$ ) as well as extra-ordinary ( $n_e$ ) indices. However, the change in  $n_o$  is relatively smaller compared to that of  $n_e$  as shown by [96].



Again in most cases, extra-ordinarily polarized light is used for various nonlinear interactions, hence we have discussed only the effect of photorefractive change of  $n_e$ . The change in refractive index ( $n_e$ ) as a result of net charge transport along +c direction of LiNbO<sub>3</sub> has been derived by widely accepted two-center model as proposed by Jermann et al [123].

**Photorefractive Damage Resistance :** In a Ti-indiffused waveguide (Channel/Ridge) the refractive index profile can be defined as :

$$n_W(x, y) = n_{bulk,air}(x, y) + \Delta n^{Ti}(x, y) \quad (3.9)$$

where  $\Delta n^{Ti}(x, y)$  is change in refractive index in the waveguide region due to Ti-indiffusion. As discussed earlier, in presence of visible and near infra-red radiation ( $\lambda < 900$  nm), there will be an intensity dependent change in refractive index profiles (photorefractive damage), which would result in deformation of the guided mode structure and finally may result into a change in phase-matching condition. Therefore, as the second harmonic waves ( $\lambda_{SH} \sim 775$  nm) generated from Ti:PPLN waveguide for an incident pump wavelength of  $\lambda_p \sim 1550$  nm), the changed refractive index profile of the waveguide can be written as:

$$n_{PRW}(x, y) = n_{bulk,air}(x, y) + \Delta n^{Ti}(x, y) - \Delta n^{PR}[I_{SH}(x, y)] \quad (3.10)$$

In the above equation,  $\Delta n^{PR}[I_{SH}(x, y)]$  is the refractive index change due to  $I_{SH}(x, y)$ , which can be represented by the normalized second harmonic intensity profile  $f_{SH}(x, y)$  in the unperturbed waveguide. Thus the generated second harmonic power can be expressed as:

$$P_{SH} = I_{SH}^{peak} \cdot \iint f_{SH}(x, y) dx dy \quad (3.11)$$

$I_{SH}^{peak}$  is the peak intensity of the guided second harmonic mode in the unperturbed waveguide. We have computed  $\Delta n^{PR}[I_{SH}(x, y)]$  using equation (1) after inserting the unperturbed guided second harmonic intensity distribution by using Lumerical Mode Solver. The resulting refractive index profile  $n_{PRW}(x, y)$  of the photorefractive damaged waveguide is then used again to obtain the final “steady-state” mode profiles for both pump and second harmonic waves. Figure 3.10 shows the algorithm used for photorefractive mode calculations in PPLN waveguides. We have calculated intensity profiles at different second harmonic power levels are shown in Figure 3.9 and noticed that ridge waveguide is far superior in preserving

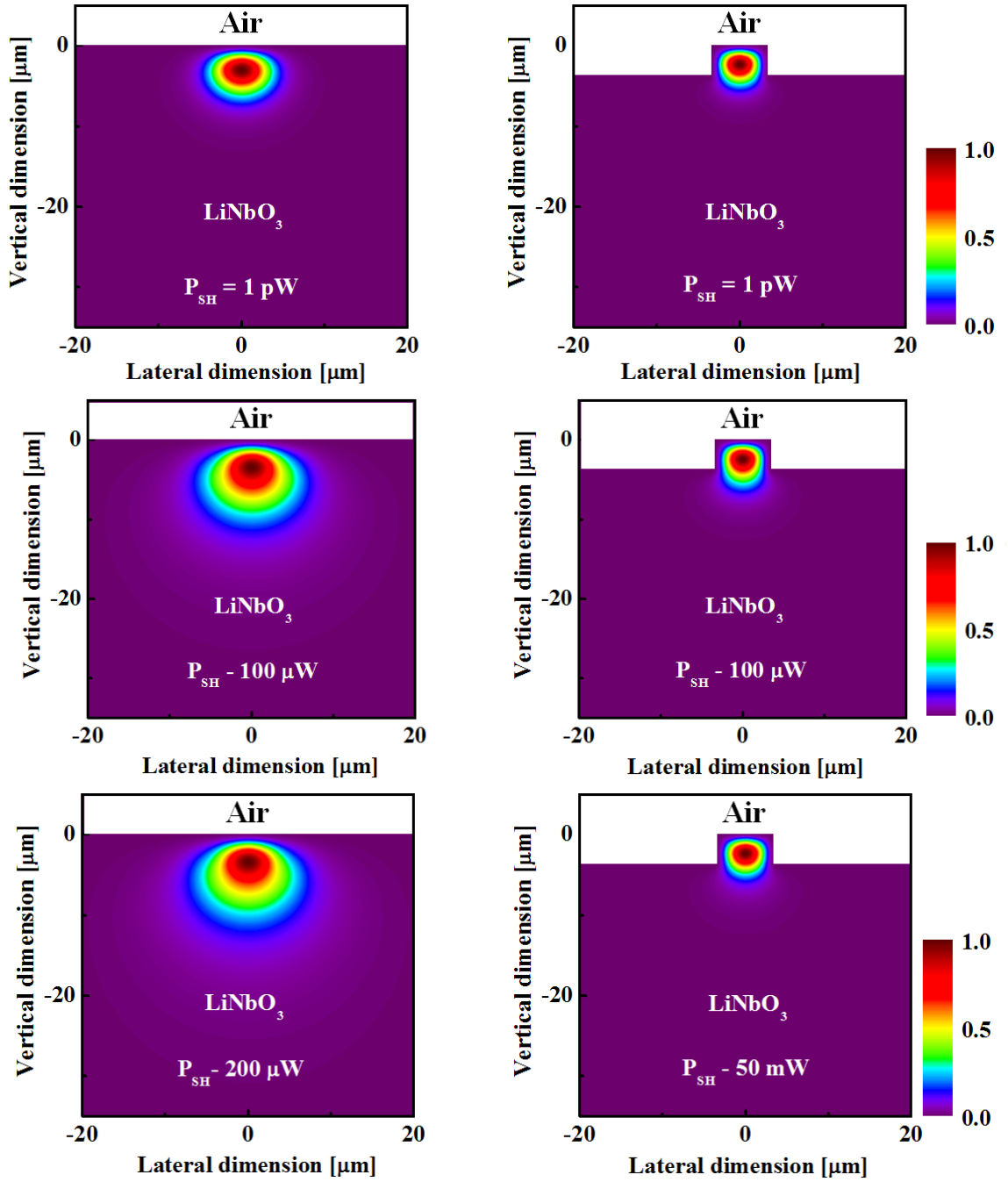


Figure 3.9: Pump intensity profiles for channel (Pol-TM) and PPLN ridge (Pol-TE) waveguide at different internal power : (a)  $P_p$  - 1 pW, (b)  $P_p$  - 100  $\mu$ W, (c)  $P_p$  - 200  $\mu$ W (50 mW)

guided mode field distributions as predicted earlier. From our results it has been observed that for a given power level though the intensity inside a ridge waveguide is more (because of tighter modal confinement), it is able to maintain the stability in the guided- mode profile due to its high index contrast, whereas in case of channel waveguide even a lower intensity is inducing a dramatic change. It is evident from Figure 3.9 that the confinement of second

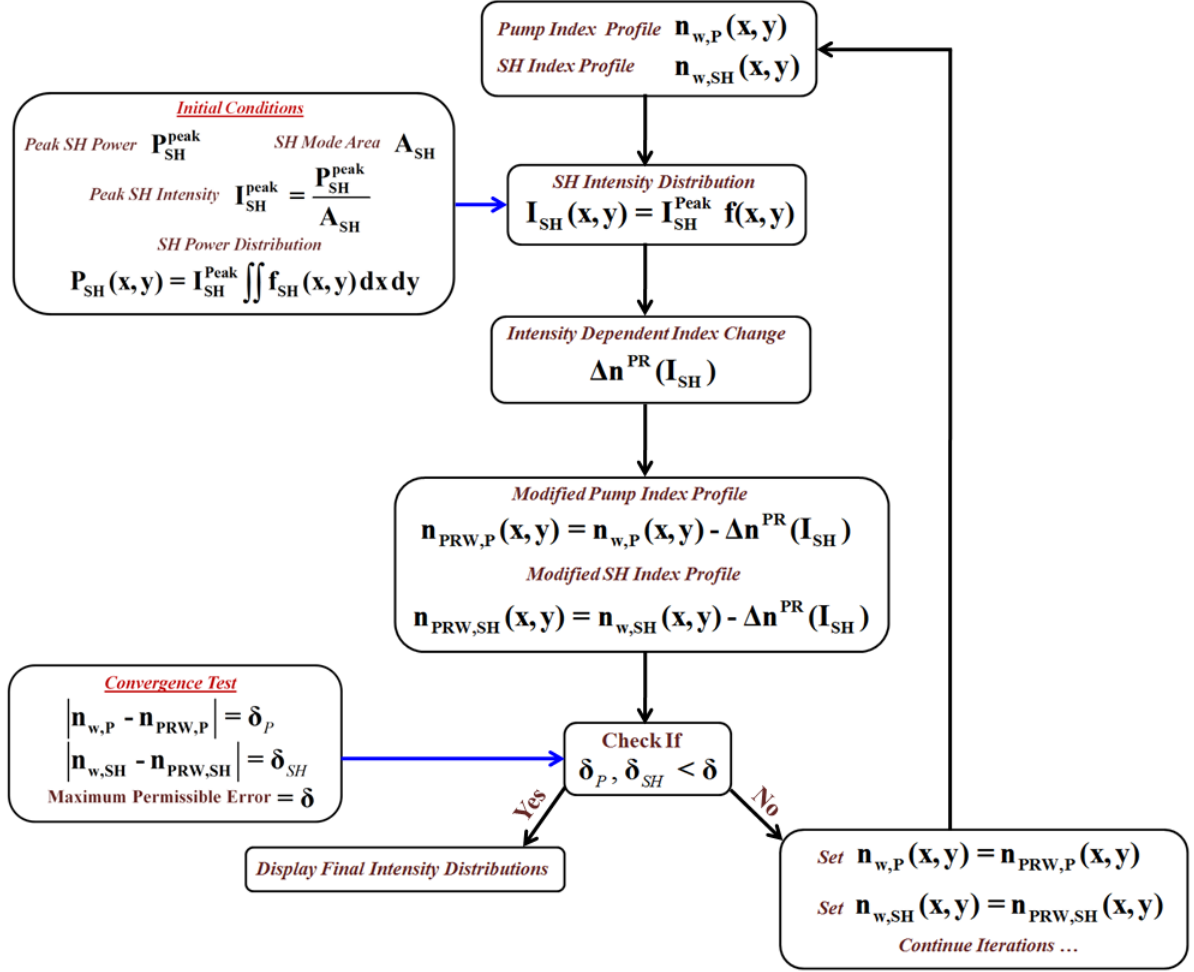


Figure 3.10: Algorithm used for Photorefractive Mode Calculations.

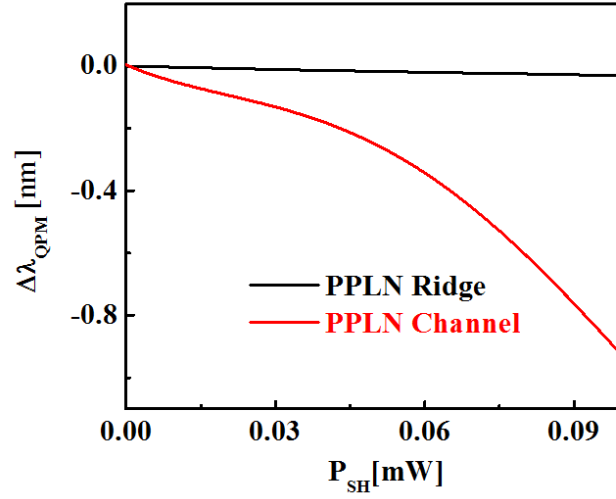
harmonic mode in channel waveguide is getting weaker at 100  $\mu$ W power level and nearly destroyed at 100  $\mu$ W. However, the calculated mode profile for ridge waveguide does not show any significant degradation even at a power level of 50 mW. This result agrees very well also with experimental results reported by [137].

### 3.4 Photorefractive Induced Detuning of $\lambda_{QPM}$

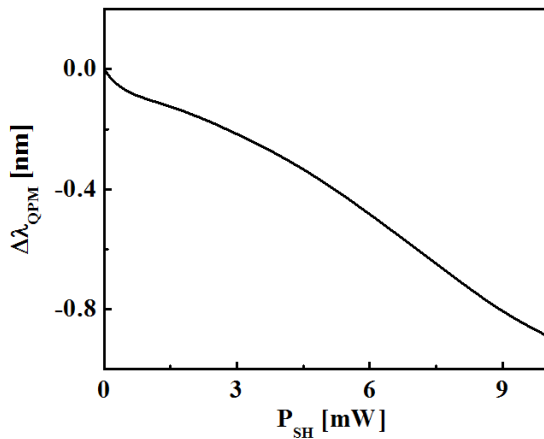
Photorefractive damage in PPLN waveguides during second harmonic generation also causes a detuning of the phase-matched wavelength (known as the blue-shift) according to the Equ. 3.12:

$$\Delta\lambda_{QPM} = 2\Lambda(\Delta n_{eff,SH} - \Delta n_{eff,p}) \quad (3.12)$$

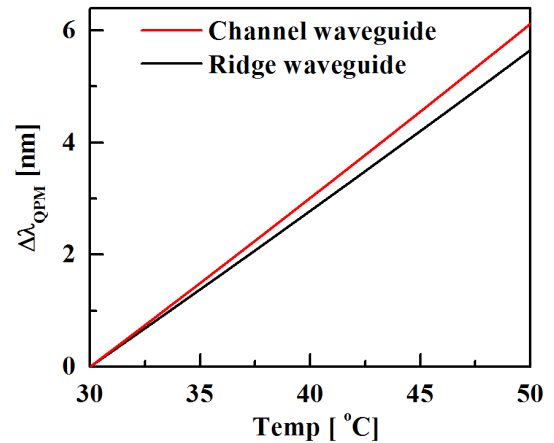
Here,  $\Delta n_{eff,SH}$  and  $\Delta n_{eff,p}$  are intensity dependent changes in guided mode effective indices at second harmonic and pump wavelengths, respectively. Figure 3.11a shows the



(a)



(b)



(c)

Figure 3.11: Phase-matching wavelength detuning  $\Delta\lambda_{QPM}$  due to: (a) low  $P_{SH}$ , (b) high  $P_{SH}$  (for ridge), (c) temperature change.

QPM-wavelength detuning  $\Delta\lambda_{QPM}$  for Ti:PPLN ridge and channel waveguides as function of the generated SH-power level  $P_{SH}$  up to 100  $\mu\text{W}$  (assuming constant SH-power along the propagation direction). As expected, the calculated detuning is much stronger for the channel guide. After the onset of photorefraction the effective area (overlap)  $S_{eff}$  of the interacting modes grows due to the change of the effective indices as discussed above. This

growth results in a reduction of the SHG-efficiency which is much stronger in the conventional channel waveguide than in the ridge waveguide. Similarly, Figure 3.11b shows the QPM-wavelength detuning in case of ridge waveguide when the generated second harmonic power inside the waveguide is much higher. Such detuning in quasi-phase matched wavelength can be compensated by slightly increasing the device operating temperature. The direction of the QPM-wavelength shift due to the temperature change is exactly opposite to the direction QPM-wavelength change due to photorefractive detuning (known as red-shift). The temperature detuning occurs according to the following equation:

$$\Delta\lambda_{QPM} = 2\Lambda \frac{d\Delta n}{dT} dT \quad (3.13)$$

where,  $d(\Delta n)/dT = (dn_{SH}/dT) - (dn_p/dT)$ . The blue-shift in the phase matching wavelength can be exactly compensated by changing the device operating temperature (close to room temperatures) according to the temperature tuning curve as shown in Figure 3.11c.

### 3.5 Conclusions

In this chapter Ti-indiffused PPLN ridge waveguides have been theoretically analyzed for single-mode guidance and optimum mode area. For similar set of fabrications parameters it has been observed that the effective mode area for the pump wave is always much larger in case of channel waveguide, which implies that it is always possible to achieve better modal confinement hence improved nonlinear interactions using ridge waveguides. Photorefractive damage resistance in PPLN ridge waveguides have been theoretically analyzed using two-center model. It has been observed that though there is detuning of the phase-matched wavelength in case of PPLN ridge waveguide due to inherent bulk-photorefractive effect in  $\text{LiNbO}_3$ , the stronger modal confinement in PPLN ridge waveguides always provides a better modal stability against photorefractive damage, resulting in a higher photorefractive damage threshold. In the following chapter various experimental investigations have been carried out to validate the theoretical prediction.

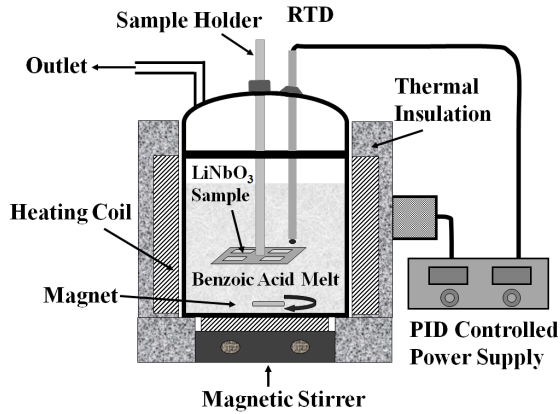
# CHAPTER 4

## Device Fabrication and Experiments

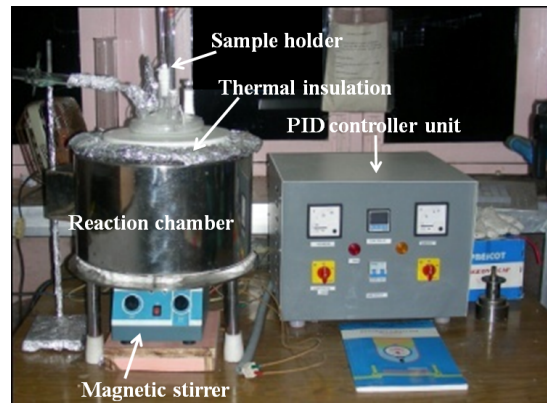
In the previous chapter, it has been theoretically established that the PPLN ridge waveguide structures are superior in terms of photorefractive damage resistance. For experimental validation, at first fabrication of APE: PPLN ridge waveguides were attempted. However, at later stage only Ti: PPLN ridge waveguides have been studied because of the access of nearly optimized fabrication process available with the Integrated Optics Group, University of Paderborn, Germany. For the completeness of the thesis work, some preliminary studies for the sample preparation carried out at IIT Madras have also been included.

### 4.1 APE Ridge Waveguides: Preliminary Studies

Different fabrication approaches towards the realization of  $\text{LiNbO}_3$  channel and ridge waveguides have been discussed in this section. Work started with the development of a suitable proton exchange reactor and annealing furnace. Subsequently, investigations were carried out for fabrication and optimization of various parameters towards single-mode guidance of lithium niobate channel and ridge waveguides. A proton exchange reactor has been designed and constructed using in-house facilities (as shown in Figure 4.1a and Figure 4.1b). In the reactor the proton exchange reaction has been carried out inside the inner glass chamber. Before starting the reaction, the chamber was filled with benzoic acid. Then small pieces of  $\text{LiNbO}_3$  were placed inside the chamber using a sample holder with adjustable height. Initially the holder was clamped much above the acid level to avoid any unwanted chemical reaction. Then the temperature of the chamber was slowly raised by using a heating coil kept surrounding the chamber. At  $180^\circ\text{C}$  benzoic acid started melting and became completely liquid above  $\sim 200^\circ\text{C}$ . The chamber was covered with an insulator layer to avoid heat dissipation during the reaction. During the entire process temperature inside the chamber was monitored and controlled using a resistance temperature detector (RTD) and PID controller. Once the temperature of the acid melt became stable at  $200^\circ\text{C}$ , samples were inserted into



(a)



(b)



(c)

Figure 4.1: Annealed-proton exchange setup: (a) schematic of the proton exchange reactor, (b) photograph of the proton exchange reactor and (c) photograph of the annealing furnace.

the acid melt by changing the height of the holder. The sample holder was made to process four samples ( $30 \text{ mm} \times 15 \text{ mm}$ ) at a time. For an uniform rate of reaction rate, the acid melt was continuously stirred during the reaction using a magnetic stirrer. The exhaust outlet in the setup was used for safe disposal of benzoic acid fumes from the reaction chamber into the main exhaust system of the laboratory. After proton exchange process waveguide samples were annealed at  $350^\circ \text{C}$  for 1-8 hours with a constant oxygen flow using a furnace installed in the lab (as shown in Figure 4.1c) to remove the index instabilities.

Figure 4.2 shows the surface profiler image of fabricated APE-channel waveguides on X-cut  $\text{LiNbO}_3$  wafer parallel to crystallographic Y-axis. These waveguides guide only extraordi-

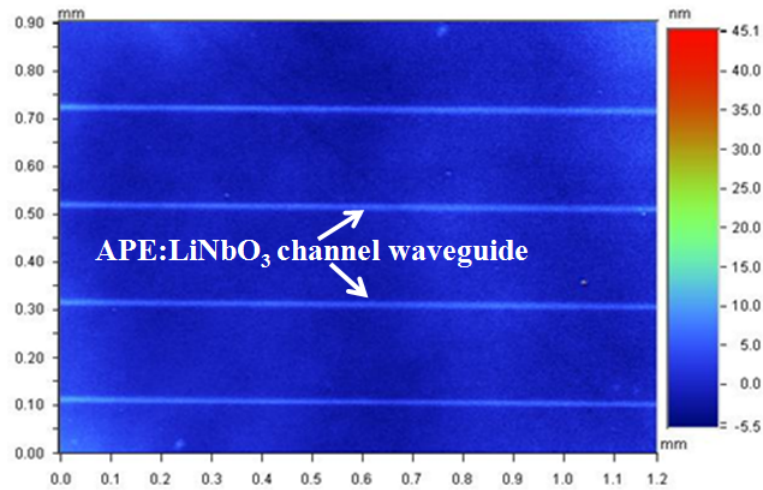


Figure 4.2: Microscope picture of fabricated APE Channel Waveguide (length - 2 cm, width -  $6 \mu\text{m}$ ).

narly polarized light at  $\lambda \sim 1550 \text{ nm}$  [138] and hence could be used as TE-pass polarizer with an extinction ratio  $\sim 35 \text{ dB}$  for the ordinarily polarized light [139].

After fabrication of channel waveguides, various etching techniques were investigated for realization lithium niobate ridge waveguides. Existing etching techniques in lithium niobate can be classified into two categories: wet-etching and dry-etching. Wet etching is the most simplest method for etching, hence initially wet etching technique in lithium niobate has been studied followed by dry-etching of lithium niobate.

**Fabrication of  $\text{LiNbO}_3$  ridge structures by wet etching :** Wet etching is a widely used technique for micro-structuring of many materials. But, etching of lithium niobate is a challenging process due to its strong etch resistance [140] and non-uniform etch rates. Wet etching has been carried out by following scheme as shown in Figure 4.3. Initially, a Cr-layer ( $4 \mu\text{m} - 8 \mu\text{m}$  wide and  $250 \text{ nm}$  thick) deposited on the substrate by e-beam evaporation and it was subsequently patterned. The patterned layer was used as a mask to protect the waveguide region during the wet etching process. The adhesion of the mask layer was increased by annealing the sample at  $500^\circ \text{C}$  for 5 hours in an inert ambiance ( $\text{N}_2$ -flow). It has found in literature that the wet etching of lithium niobate is excessively slow, but the introduction of structural defects on the substrate surface can accelerate the etching rate. Hence, surface activation of the unmasked lithium niobate surface was carried out in 99.9% benzoic acid melt which acted as a source of protons ( $\text{H}^+$ ) and  $\text{Li}^+$ -ions from the



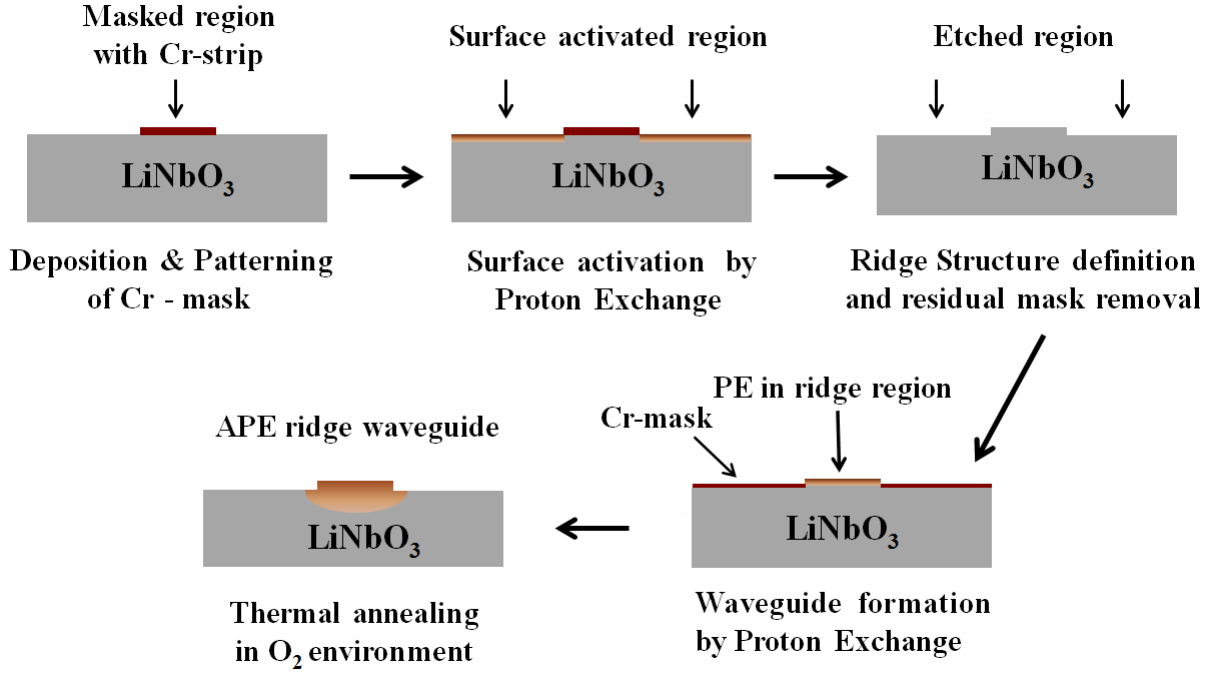
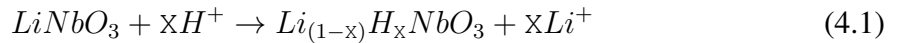


Figure 4.3: Fabrication scheme for APE:LiNbO<sub>3</sub> ridge waveguides.

substrate surface were replaced by H<sup>+</sup>-ions creating sufficient surface modifications and hence defects. The chemical reaction that took place at the surface layer of LiNbO<sub>3</sub> crystal during the proton exchange process can be written as:



Here  $Li_{(1-x)}H_xNbO_3$  is the composition of the exchanged layer and  $x$  is the fraction of exchanged ions. Normally, the rate of indiffusion of H<sup>+</sup>-ions to lithium niobate increases at an elevated temperature for proton exchange. Initial calculation showed that the proper confinement of the guided mode is possible with ridge height greater than 3  $\mu\text{m}$  or even more, following that the surface activation was carried at a temperature 230° C (diffusion co-efficient:  $D = 0.818 \mu\text{m}^2 / \text{hr}$  [141]) for 3 hrs so that subsequently the optimum etch depth can be realized by wet etching. However, it was observed that due to a strong proton exchange reaction at 230° C at a temperature close to the boiling point of benzoic acid ( $\sim 249^\circ \text{C}$ ), micro-cracks were developed in proton exchanged regions of the substrate which were then propagated towards masked regions in course of time as shown in Fig. 4.4. Subsequently, surface activation was carried out at 200° C and for relatively longer time to achieve the optimum diffusion depth. After surface activation by proton exchange process,



Figure 4.4: Surface damage in LiNbO<sub>3</sub> substrate during surface activation.

wet etching of C-cut lithium niobate was carried out. Two different types of solutions were used for this purpose. Solution I : conc. HF and conc. HNO<sub>3</sub> = 1:2 and solution II : 60-ml HF with 40% conc, 39-ml HNO<sub>3</sub> with 100% conc. The wet-etching was performed at the room

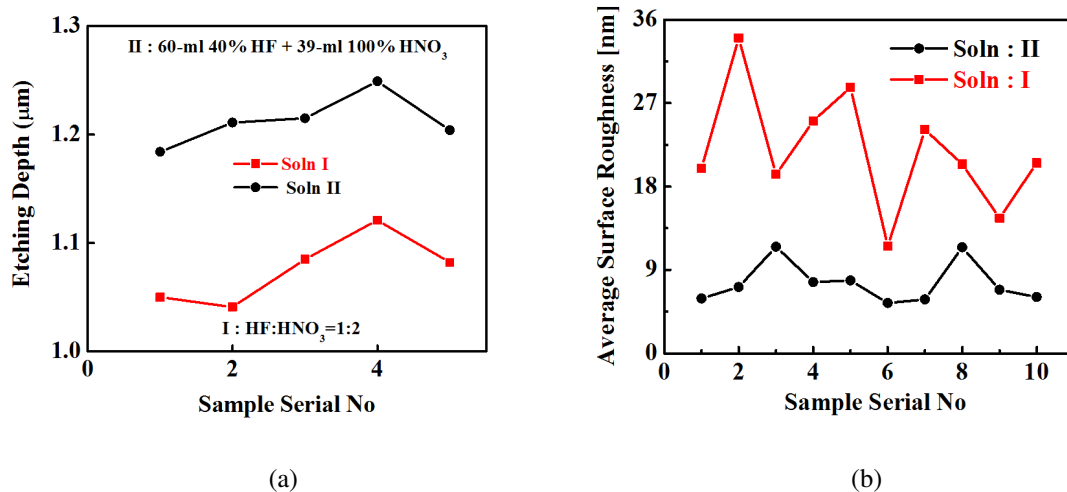


Figure 4.5: Wet etching of LiNbO<sub>3</sub>: (a) etch-dept and(b) surface roughness.

temperature without stirring. After etching the sample has been cleaned thoroughly and then the Cr-mask has been removed from the surface. Then followed by another cleaning step, the sample was coated with a very thin layer of Al before any further measurement. Surface characteristics of the lithium niobate sample carried out using a surface-profiler (Model No: VEECO NT 1000). The average etching depth was found to be higher in the sample etched using the solution-II (shown in Figure. 4.5) and also the measured rms surface roughness was found to be relatively less in the second sample. Hence, solution-II was used for sub-

sequent wet etching studies. The etch depth could be increased with increasing the depth of the proton exchanged region (as shown in Fig. 4.6). After the surface activation, the wet

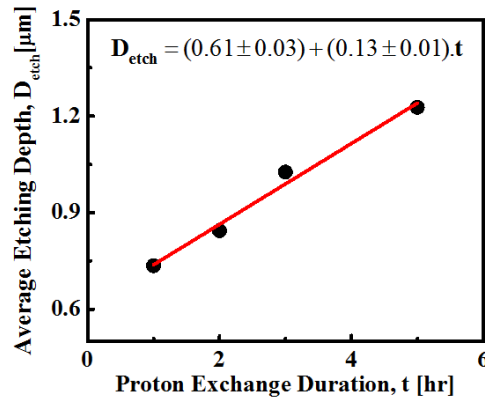


Figure 4.6: Wet etch depth vs. proton exchange duration

etching of the substrate was carried out using a mixture of 60-ml HF (40% conc.) and 39-ml HNO<sub>3</sub> (100% conc.) at room temperatures (see Fig. 4.7). After 12 hours of wet etching an etch depth  $\sim 2.8 \mu\text{m}$  was obtained, but considerable amount of under-etching was observed underneath the mask and the boundary between etched and non-etched part had a spread of over a distance  $\sim 20 \mu\text{m}$  (as shown in Fig. 4.7) due to long etching time. Also, at the

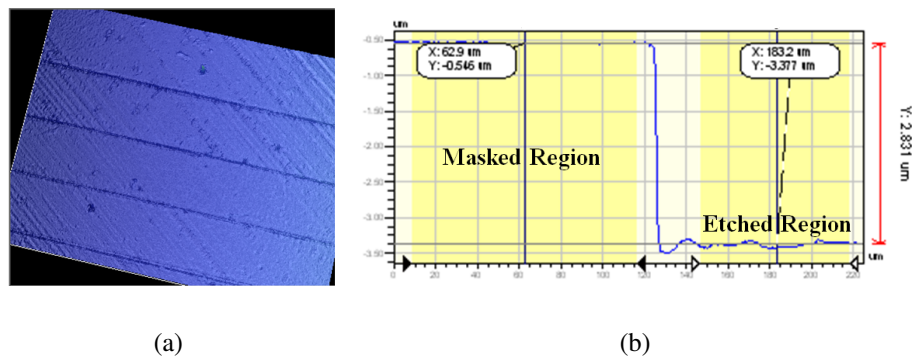


Figure 4.7: Wet etching of LiNbO<sub>3</sub>: (a) wet-etched surface, (b) wet-etch step height.

end of the process ridge cross-sections became almost triangular in shape due to excessive under-cut (as shown in Fig. 4.7). Hence, these structures are found to be unsuitable for the fabrication of APE:LN ridge waveguides.

**Fabrication of LiNbO<sub>3</sub> ridge structures by RIE :** After wet etching dry-etching (RIE and ICP-RIE) of lithium niobate were also investigated. Dry etching of lithium niobate was carried out using fluorine based plasma due to good volatility of fully fluorinated niobium species at temperature  $\sim 200^\circ \text{C}$ . But, it could also result in re-deposition of LiF [142] on

the etched surface. LiF has a melting temperature more than 800° C. Also LiF re-deposition could lower the subsequent etching rate. To prevent the re-deposition of LiF, lithium concentration at the substrate surface was reduced by proton exchange process [143]. To keep the re-deposition of LiF under control etching process was carried out in smaller steps (3-4 min duration) and then post-etching the substrate was cleaned using a solution  $\text{NH}_4\text{OH}:\text{H}_2\text{O}_2:\text{H}_2\text{O} = 7:10:35$  solution for 30 sec to remove the etching residue as described in [137]. The etching process was repeated multiple times till the final etching depth is achieved. prior to dry etching, surface activation was carried out by proton exchange process in a benzoic acid melt at 200° C for 12 hours. At first attempt, dry etching was carried out with the following chemistry -  $\text{SF}_6:\text{Ar} :: 25\text{ sccm}: 20\text{ sccm}$ , RF power - 200 W, pressure - 100 mTorr. After

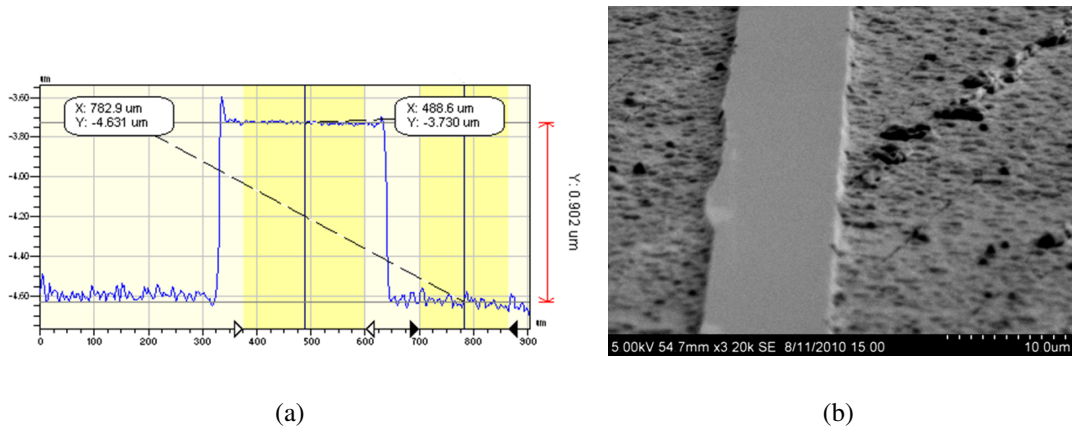
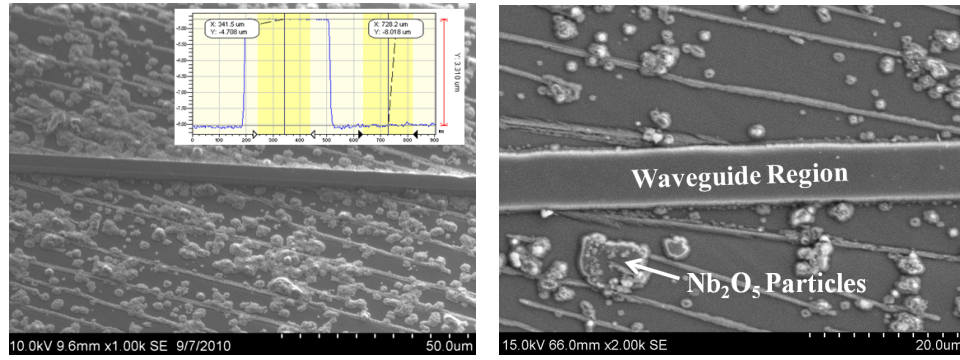


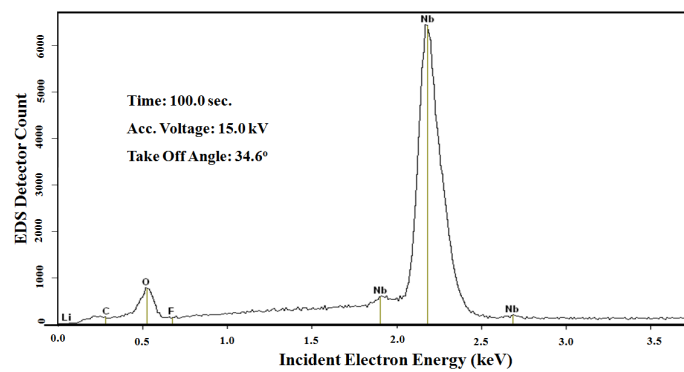
Figure 4.8: Reactive ion etching of  $\text{LiNbO}_3$  by  $\text{SF}_6:\text{Ar}$  Recipe : (a) step height, (b) surface morphology.

etching the sample for 3-4 minutes, it was cleaned thoroughly in  $\text{NH}_4\text{OH}:\text{H}_2\text{O}_2:\text{H}_2\text{O}$  solution. An etch depth  $\sim 0.9\ \mu\text{m}$  was obtained after 60 min of etching and also the surface roughness of the substrate was very high. Step height and the surface morphology of the etched structure has been shown in Figure 4.8. Next, dry-etching of lithium niobate substrate was carried out using the recipe:  $\text{CHF}_3:\text{Ar} :: 50\text{ sccm}: 50\text{ sccm}$ , RF power - 350 W, pressure - 60 mTorr. The sample was etched upto a depth  $\sim 3.23\ \mu\text{m}$  in 100 minutes (as shown in Figure 4.9a). But, after etching many islands like depositions were observed on the etched surface (as shown in Figure 4.9b), which could not be removed by plasma cleaning or high temperature annealing. Even keeping the sample in concentrated HF solution for  $\sim 12$  hours did not have effect any effect on those white deposits. Also some residual stress were observed on the surface in a regular linear pattern at an angle  $\sim 8^\circ$  with crys-



(a)

(b)



(c)

Figure 4.9: Reactive ion etching of  $\text{LiNbO}_3$  by  $\text{CHF}_3$ : Ar recipe : (a) ridge rtructure (side view), (b) ridge rtructure (top view), (c) EDS analysis.

tallographic Y-axis (waveguides are parallel to Y-axis), which was not removed completely even after etching up to  $3.23 \mu\text{m}$ . But, no surface stress was observed at portions of the substrate covered by the metal mask (ridge region). EDS studies of the white deposition on the substrate showed that these deposits were  $\text{Nb}_2\text{O}_5$  compounds (as shown in Figure 4.9c). Due to non-ideal surface condition the above approach was also found to be unsuitable for subsequent waveguide fabrication.

## 4.2 Ti:PPLN Waveguides: Sample Preparation

The fabrication work for  $\text{Ti}:\text{LiNbO}_3$  PPLN ridge waveguides was carried out in the Technology Laboratory of the Integrated Optics Group, University of Paderborn. Ti-indiffused PPLN ridge waveguides were fabricated on both X-cut and Y-cut  $\text{LiNbO}_3$  substrates fol-

lowing a similar fabrication scheme. Hence, only the fabrication scheme for Y-cut ridge waveguides has been briefly discussed. Details of the fabrication technique can be found elsewhere [90]. A scheme for the ridge waveguide fabrication is shown below in Figure 4.10.

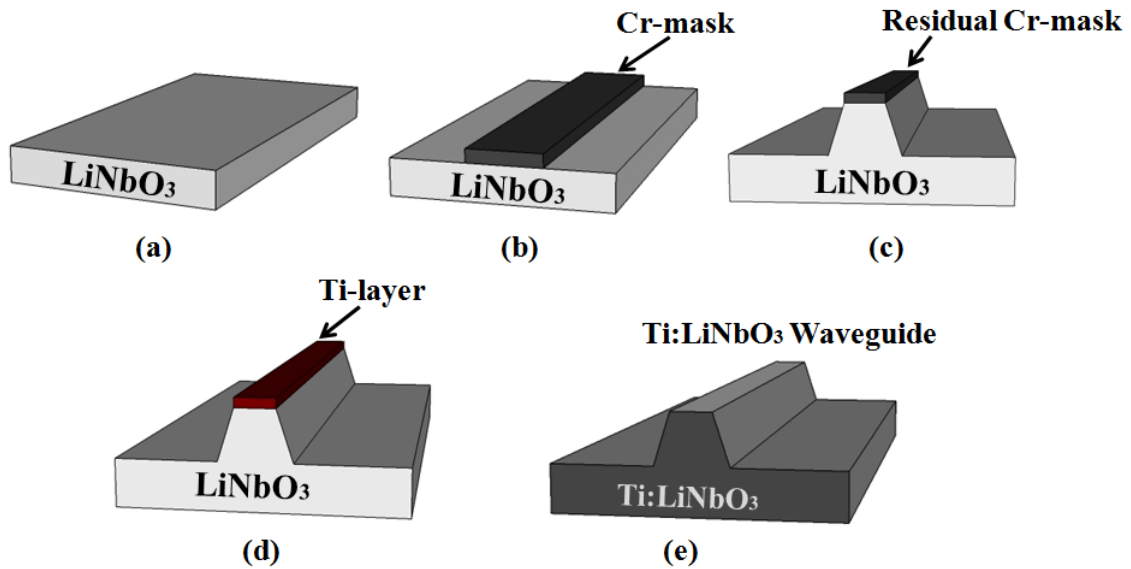


Figure 4.10: Scheme of ridge waveguide fabrication: (a) wafer cleaning and, (b) Patterning of Cr- mask, (c) Ridge structure definition, (d) Deposition of Ti-layer on top of the ridge, (e) Ridge waveguide fabrication by Ti-indiffusion.

**Substrate preparation :** Initially, the Y-cut substrate was diced into smaller pieces ( $20 \text{ mm} \times 25 \text{ mm}$ ) and then these were thoroughly cleaned in “piranha” solution ( $\text{H}_2\text{SO}_4:\text{H}_2\text{O}_2 = 3:1$ ) at  $50^\circ \text{ C}$  for 15 minutes to remove various organic residues from the sample. After that, the sample was cleaned in a running flow of DI water to remove various residues of the acid. Next, it was cleaned in RCA-I solution for ( $\text{H}_2\text{O}:\text{H}_2\text{O}_2:\text{NH}_4\text{OH} = 7:2:1$ ) for 30 minute to remove various metal contaminant from the wafer. Finally, after drying the sample with  $\text{N}_2$ -gun, it was immediately loaded into the e-beam evaporation system.

**Deposition and definition of Cr-mask :** A 300 nm thick Cr-layer was deposited on the substrate surface. Then it was patterned into  $8 \mu\text{m}$  and  $10 \mu\text{m}$  wide Cr-strips parallel to crystallographic X-axis by optical lithography and wet chemical etching of Cr. These Cr stripes were used as masks during subsequent dry etching process.

**Definition of ridge structure by ICP-etching :** For ICP-etching of the Y-cut substrate the following recipe was used :  $\text{C}_4\text{F}_8:\text{He} = 15 \text{ sccm}:15 \text{ sccm}$ , Pressure - 10 mT, ICP power -

1000 W, RF power - 50 W. To avoid the re-deposition of LiF inhibitors the etching process

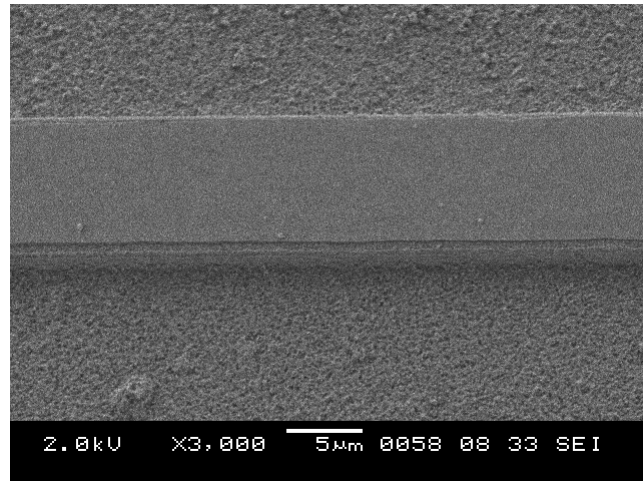


Figure 4.11: SEM micrograph fabricated ridge structure after ICP etching.

was continued in small steps (3-4 minutes) and in repetitive manner. The average etch rate was found to be  $\sim 300$ - $400$  nm/step. After etching the sample was cleaned using  $\text{NH}_4\text{OH}:\text{H}_2\text{O}_2:\text{H}_2\text{O} = 7:10:35$  solution for 30 sec to remove the etching residue. The final etch depth of the ridge structure was found  $\sim 4\mu\text{m}$ . After etching, waveguide cross-section was found to be trapezoidal in nature and also waveguide side-walls were found to be extremely rough (as shown in Fig. 4.11).

**Waveguide fabrication by Ti-indiffusion :** A 100 nm thick Ti-layer was deposited on top of fabricated ridge structures, and Ti-indiffusion was carried out at  $1060^\circ\text{C}$  for 8.5 hours in  $\text{O}_2$  environment. During the high temperature indiffusion process the sidewall roughness of waveguides reduced considerably (as shown in Figure 4.12).

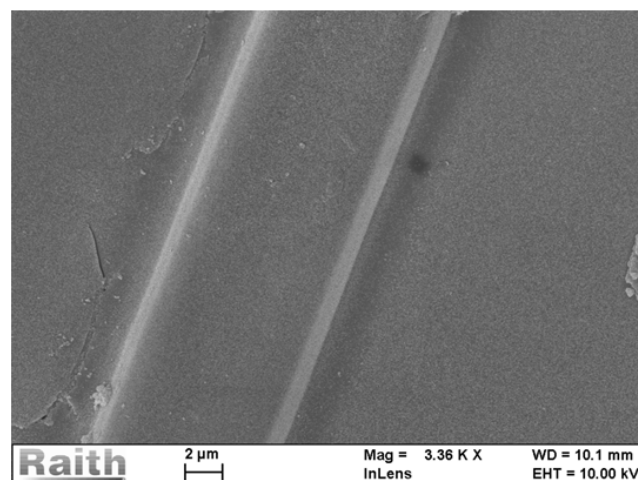


Figure 4.12: SEM picture of fabricated Ti-indiffused ridge waveguide



**Local periodic poling of Ti:LiNbO<sub>3</sub> ridge waveguides :** The spontaneous polarization of the fabricated Y-cut LiNbO<sub>3</sub> was oriented along the crystallographic Z-axis i.e. perpendicular to side walls of fabricated ridge waveguides. To use the highest nonlinear coefficient  $d_{33}$  of LiNbO<sub>3</sub> (which is oriented along Z-axis) in the phase-matching process, metal electrodes for periodic poling were deposited on side walls of ridge waveguides. For electrode structures, initially 100 nm thick Ti-layer was deposited on the entire substrate and subsequently it was patterned using optical lithography to fabricate comb-like electrodes on side walls of fabricated waveguides as shown in Figure 4.13. Waveguides were fabricated with

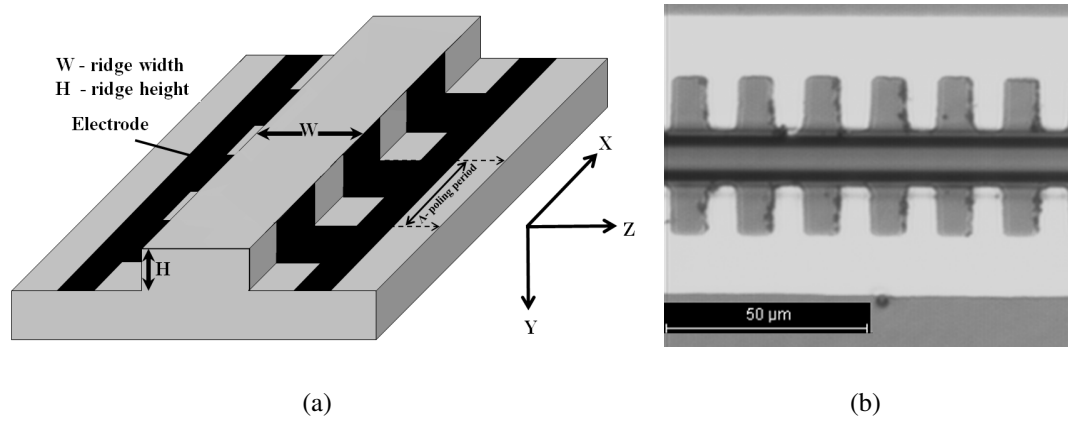


Figure 4.13: Local periodic poling : (a) scheme of the electrode pattern, (b) deposited comb-electrode structure.

two different poling periodicity ( $\Lambda$ ):  $16.1 \mu\text{m}$ . The spontaneous polarization of congruent LiNbO<sub>3</sub> at room temperature is,  $P_s = 0.72 \mu\text{C}/\text{mm}^2$ . The height of the ridge waveguide was  $4 \mu\text{m}$  ( $= 0.004 \text{ mm}$ ) and length of the electrode section -  $15 \text{ mm}$ . Since, a group of four ridge waveguides were poled together, corresponding total poling area,  $A_{pol} = (0.004 \text{ mm} \times 15 \text{ mm}) = 0.06 \text{ mm}^2$ . So, the total amount of charge needed to be transferred during the domain reversal process can be calculated according to the Equation (4.2):

$$Q_{pol} = \int i dt = 2 \cdot P_s \cdot A_{pol} \quad (4.2)$$

Here,  $i$  is the switching current and the total poling charge,  $Q_{pol} = (0.72 \mu\text{C}/\text{mm}^2 \times 0.12 \text{ mm}^2) = 0.0864 \mu\text{C} \approx 0.1 \mu\text{C}$ . The poling process was carried out in an oil bath to maintain a very high resistance between two electrodes and avoid any short-circuit current that could have been generated between electrodes during the application of a high-voltage pulse. At the beginning, voltage pulses were applied along -Z axis of the crystal to that all the ran-



domly oriented domains were oriented along Z-axis. A poling voltage  $V_{LN} = 0.7$  kV was applied across the sample using a DC voltage amplifier and the corresponding poling current  $I_{LN}$  can be written as:

$$V_{LN} = \frac{(R_2 + R_3)}{R_3} \cdot V_1 - V_2 \quad (4.3)$$

and

$$I_{LN} = \frac{V_2}{R_4} \quad (4.4)$$

A schematic of the poling circuit and a photograph of the poling setup is shown in the Fig. 4.14. Figure 4.15 shows the poling characteristics for a Ti-indiffused ridge waveguide

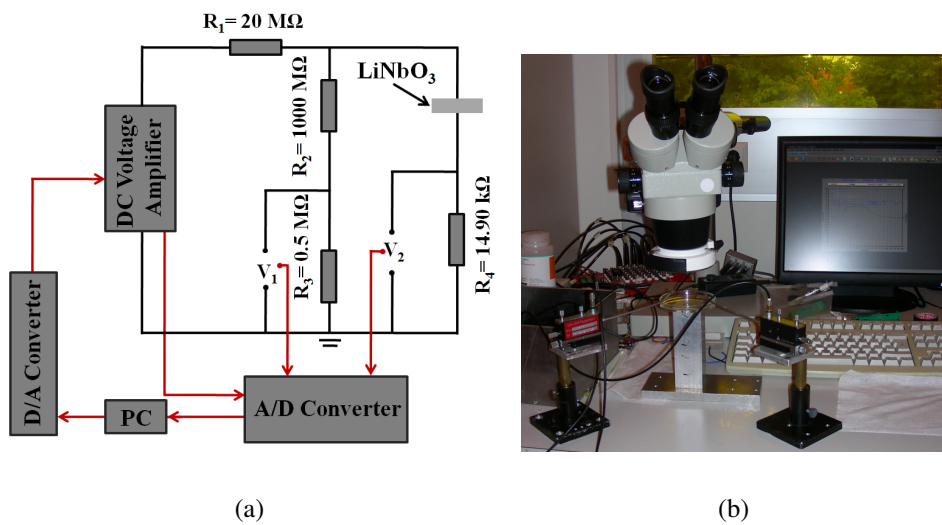


Figure 4.14: Periodic poling setup for ridge waveguide: (a) circuit diagram, (b) photograph of the setup (@ Integrated Optics Group, University of Paderborn).

with a single voltage pulse. The domain inversion process started at a voltage  $\sim 0.4$ kV

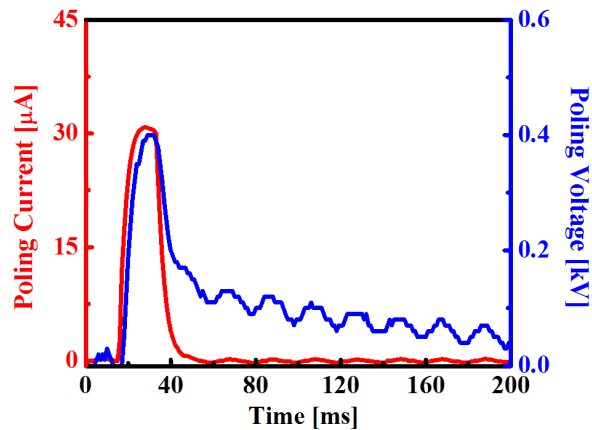


Figure 4.15: Poling characteristics of a Ti-indiffused PPLN ridge waveguide.

(as seen in 4.15). The switching current remained nearly constant as long as the constant voltage was applied and then it started dropping as soon as the applied voltage was ramped down. The total measured charge used to complete the polling process was  $1.01 \mu\text{C}$ . The difference between the calculated and the measured value can be attributed to the presence of surface leakage current during the polling process. To reveal the shape of the ferroelectric micro-domains, a periodically poled Y-cut ridge waveguide was immersed in  $\text{HF:HNO}_3$  solution for 30 minutes and then it was thoroughly cleaned under running flow of DI water and photograph of the etched sample was taken using a confocal microscope. In Figure 4.16

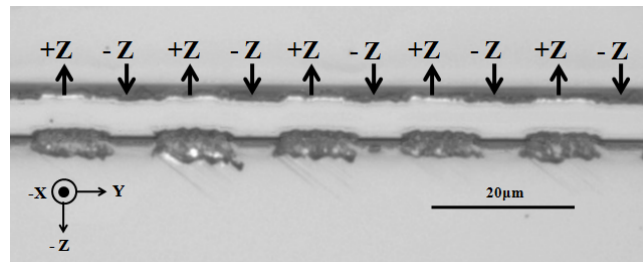
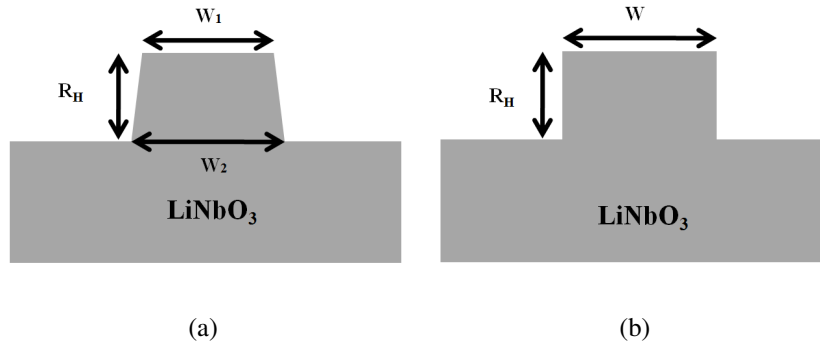


Figure 4.16: Visualization of micro-domains in a Y-cut PPLN ridge waveguide.

shows a periodical etching of ridge waveguide side walls. In the inverted domains both directions of Z-axis were rotated by  $180^\circ$ . Hence, side walls of ridge waveguides showed a sequence of +Z- and -Z-faces. Since, the differential etch along +Z and -Z faces of  $\text{LiNbO}_3$  are different from the etched structure the reversal of ferroelectric micro-domains could be identified.

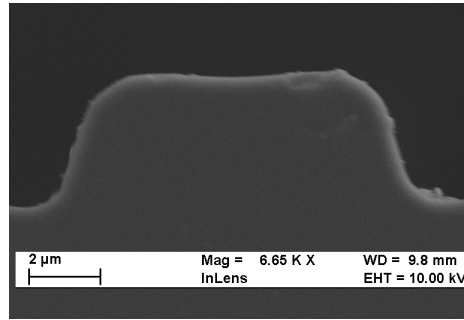
Reference PPLN channel waveguides used in the present investigations were fabricated using similar standard fabrication procedure as described in the literature [3]. After fabrication, waveguide endfaces were optically polished perpendicular to the waveguide length and then various optical characterizations were carried out.

**Measurement of waveguide dimensions :** Measurement of waveguide dimensions by microscope showed that the etching process was not completely anisotropic and waveguide cross-sections have become slightly trapezoidal (as shown in Figure 4.17a). According to the design waveguide cross-sections were considered to be rectangular (as shown in Figure 4.17b). Various waveguide parameters used to define trapezoidal and ridge waveguide cross-sections have been shown in Figure 4.17. SEM-micrograph of a fabricated ridge waveguide has been shown in Figure 4.17c and waveguide dimensions has been shown in



(a)

(b)



(c)

Figure 4.17: Ridge waveguide cross-sections : (a) rectangular ( $W$  - ridge width,  $R_H$  - ridge height), (b) trapezoidal ( $W_1$  - upper ridge width,  $W_2$  - lower ridge width,  $R_H$  - ridge height), (c) fabricated Y- cut ridge waveguide end-face.

Table 4.1.

Table 4.1: Dimensions of Fabricated Ridge Waveguides ( $W_1$  - upper ridge width,  $W_2$  - lower ridge width)

Waveguide No.	Mask Width $W$ [ $\mu\text{m}$ ]	Waveguide Width [ $\mu\text{m}$ ]	Ridge Height $R_H$ [ $\mu\text{m}$ ]
<b>Sample # Pb11Y (Y-cut Ridge Waveguide, Length - 15 mm)</b>			
1	8	$W_1 = 5.6, W_2 = 7.4$	4.0
2	10	$W_1 = 8.0, W_2 = 9.7$	4.0
<b>Sample # Pb349X (X-cut Ridge Waveguide, Length - 33 mm)</b>			
3	7	$W_1 = 5.6, W_2 = 6.7$	3.0

**Measurement of guided intensity profiles:** Guided intensity profiles for fabricated Ti-indiffused ridge waveguides were measured @  $\lambda \sim 1550$  nm using a free-space coupling setup (shown in Figure 4.18). A lens with higher magnification was used at the waveguide output for further magnification of the waveguide mode, which is essential for accurate

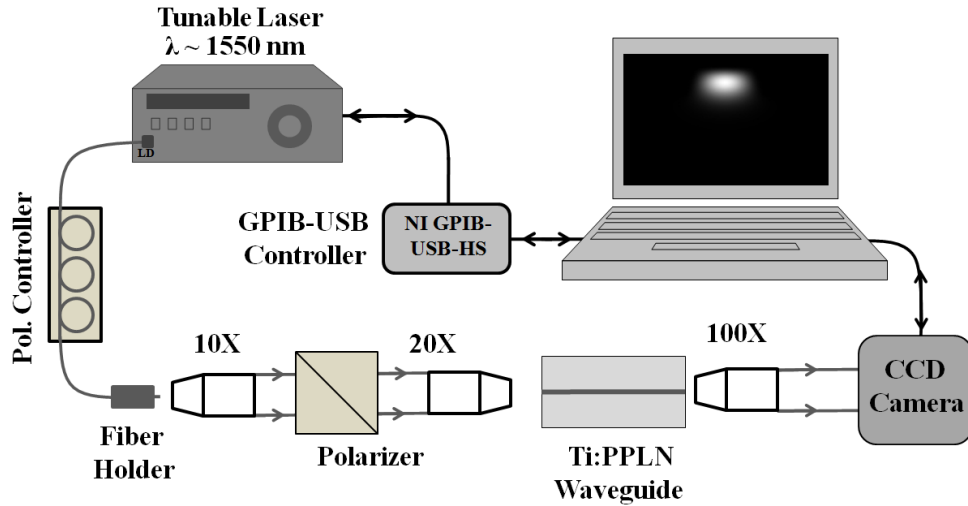


Figure 4.18: Schematic of the mode-profile measurement setup.

determination of modal-dimensions. Waveguide mode distributions were captured using a CCD camera kept at a distance ( $\sim 1$  m) away from the output lens. Figure 4.19 shows guided optical mode distributions for both TE- and TM-polarized waves in case of a Ti indiffused ridge waveguide fabricated on a Y-cut substrate having width  $8.2 \mu\text{m}$  ( $9.9 \mu\text{m}$ ) and ridge height  $\sim 4.2 \mu\text{m}$ . Fabricated waveguides were found to guide only the fundamental

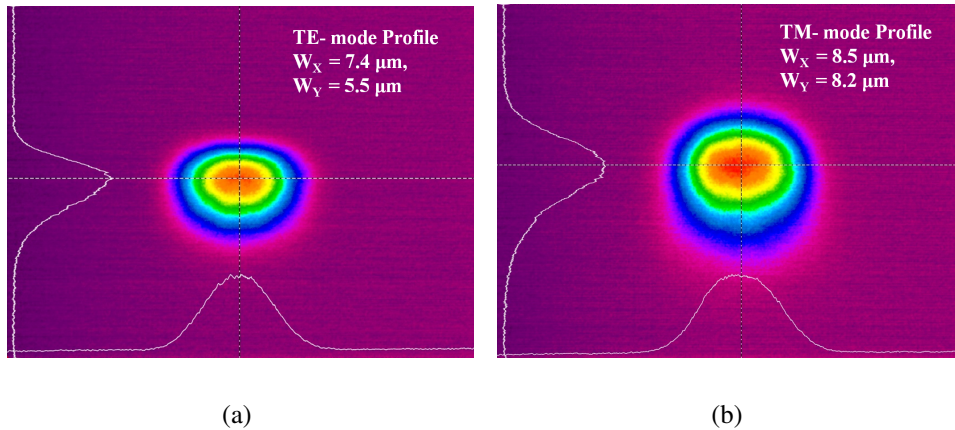


Figure 4.19: Guided intensity profiles for Y-cut PPLN ridge waveguide: (a) TE-polarized wave, (b) TM-polarized wave.

modes for our range of operation. For a ridge waveguide on a Y-cut  $\text{LiNbO}_3$  substrate, the index-contrast for the extra-ordinary polarized guided mode is much higher compared to ordinary-polarized guided mode, hence TE-polarized mode distribution is smaller in size compared to the TM-polarized mode distribution. Guided mode profiles for Ti-indiffused channel waveguides fabricated with similar parameters on Z-cut substrate (Ti-layer thick-

ness - 100 nm, diffusion temperature - 1060°C, diffusion time - 8.5 hours in O<sub>2</sub> environment) have been shown in Figure 4.20. At  $\lambda \sim 1550$  nm measured mode dimensions were: TE-pol ( $11.3 \mu\text{m} \times 7.9 \mu\text{m}$ ) and TM-pol ( $8.4 \mu\text{m} \times 3.7 \mu\text{m}$ ), which were much larger in size compared to ridge waveguide guided modes as expected from our calculations.

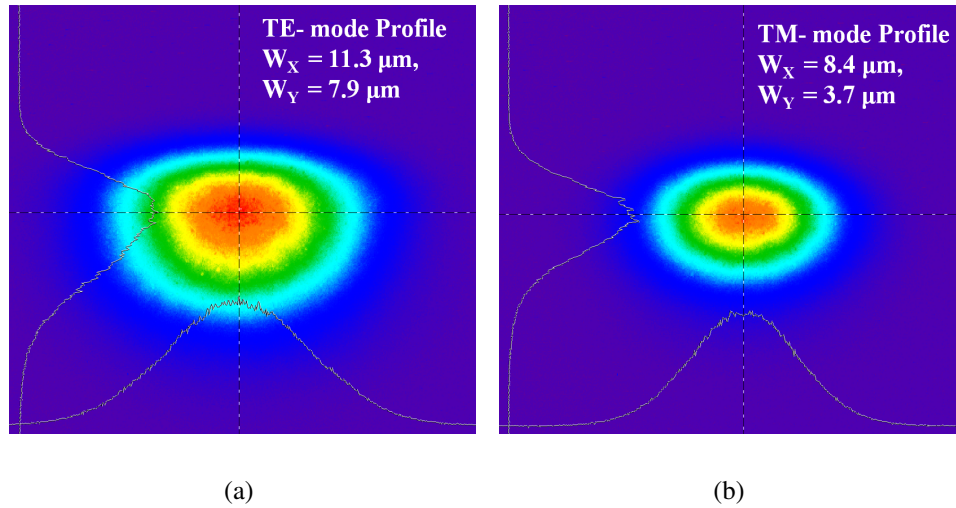


Figure 4.20: Guided intensity profiles for Z-cut PPLN channel waveguide: (a) TE-polarized wave, (b) TM-polarized wave.

**Measurement of propagation loss :** Propagation loss for fabricated PPLN ridge waveguides were calculated using the low-finesse Fabry-Perot resonance method [144]. Polished end faces of the waveguide formed a low-finesse cavity and the cavity was tuned by varying the input wavelength of the propagating wave. The propagation loss  $\alpha$  [dB/cm] of a waveguide of length “L” was calculated from the resonance-contrast of the low-finesse cavity using the Equ. (4.5):

$$\alpha = \frac{4.34}{L}(\ln R + \ln 2 - \ln K) \quad (4.5)$$

Here, R is the reflectivity of waveguide end-faces and K is the measured intensity contrast as shown in Equ. (4.6) :

$$K = \frac{I_{max} - I_{min}}{I_{max} + I_{min}} \quad (4.6)$$

$\alpha$  defines the upper limit of the propagation loss for a given waveguide. The schematic of the setup used for propagation loss measurement has been shown in Figure 4.21. The output fiber from the tunable laser source (Santec TSL 210V) was connected to a polarization controller and the output from the polarization controller was collimated using a 10X-lens. Then collimated beam was polarized with the help of a polarizer and

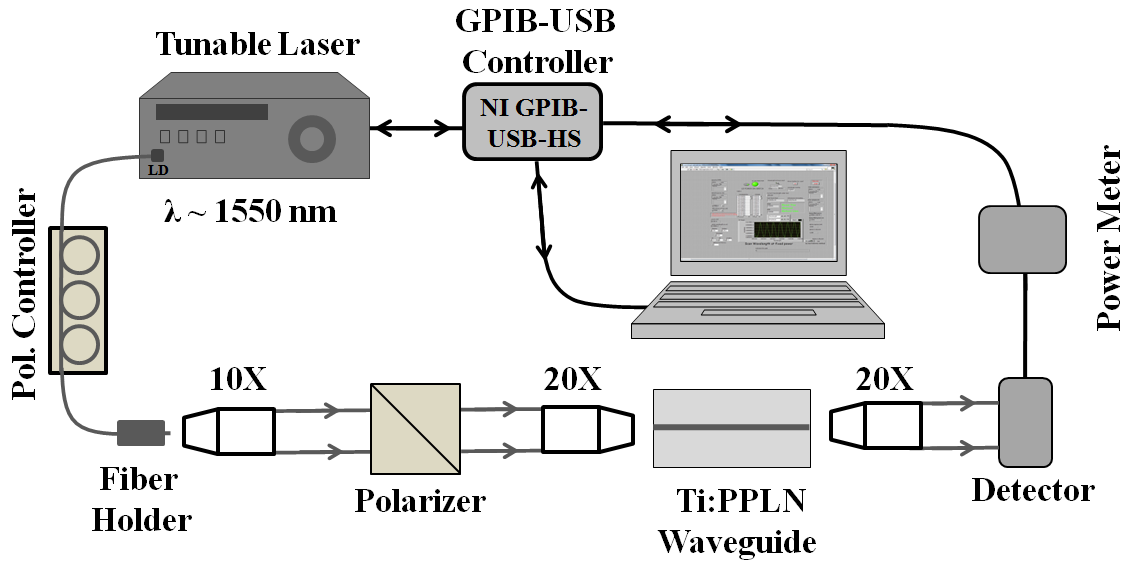


Figure 4.21: Schematic of waveguide propagation loss measurement setup.

the polarization controller. The polarized beam was then focussed at the waveguide input using a 20X focusing lens. The transmitted output from the waveguide was collected by a 20X output lens (20X-magnification) and it was directly coupled onto the detector (S132A). Transmitted output power of the waveguide was measured as a function of input wavelength. Experimental setup for propagation loss measurement is shown in Figure 4.22. In ridge

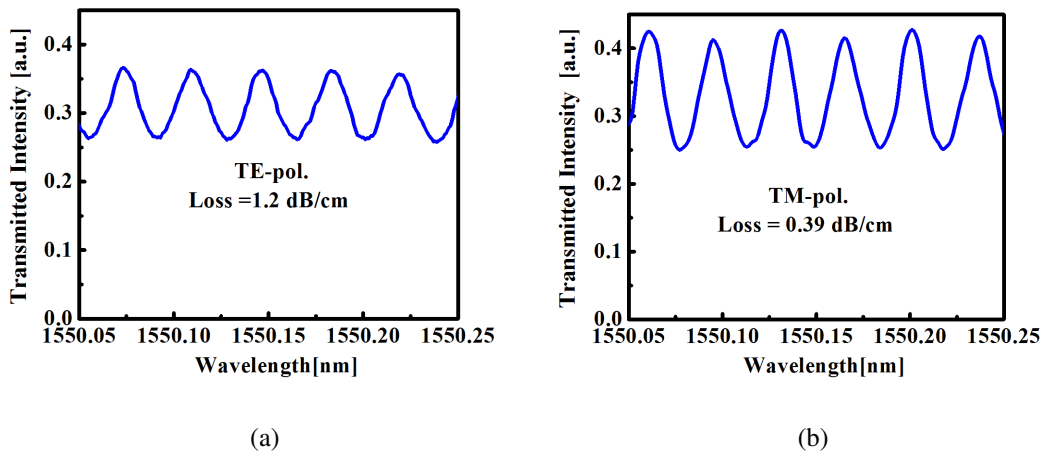


Figure 4.22: Experimentally measured waveguide propagation loss:(a) TE-pol;(b) TM-pol.

waveguides TE-polarized guided waves were found to have higher propagation loss due to direct interaction of the corresponding with waveguide side-walls. Table 4.2 summarizes propagation losses for different PPLN ridge waveguides investigated in this work.

Table 4.2: Propagation Loss for PPLN Ridge Waveguides

Waveguide No.	Loss (TE-pol.) [dB/cm]	Loss (TM-pol.) [dB/cm]
<b>Sample # Pb11Y (L - 15 mm)</b>		
1	1.81	0.91
2	1.2	0.39
<b>Sample # Pb349X (L - 33 mm)</b>		
3	1.19	0.55

### 4.3 Photorefractive Damage : Experimental Results

In this section various experimental results related to photorefractive damage and second harmonic generation in PPLN waveguides have been discussed. All investigations were carried out using an experimental setup developed at Integrated Optoelectronics Laboratory, IIT Madras.

#### 4.3.1 Photorefractive damage of guided modes at $\lambda - 635$ nm

Initially, the effect of photorefractive damage was investigated on fabricated channel and ridge waveguides  $\lambda \sim 635$  nm. The experimental setup used for this investigation is shown in Figure 4.23. To maximize the effect of photorefractive damage polarized input beam (TM-polarized in case of channel waveguide and TE-polarized in case of ridge waveguide) was coupled into the waveguide and resulting intensity distributions were recorded with the help of a CCD camera.

Figure 4.24 shows the photo-refraction induced catastrophic change in a Ti-indiffused channel waveguide fabricated on a Z-cut LiNbO<sub>3</sub> wafer (on -Z-surface). A red laser beam ( $\lambda_{PR} = 635$  nm) of  $P_{coup} \sim 210 \mu\text{W}$  was transmitted through the channel waveguide of 30 mm length. Intensity distributions of the transmitted beam were recorded at different intervals of time: (a) immediately after switching on the laser, (b) after 2 min of irradiation. Since, the waveguide under investigation was designed to support only the fundamental mode at  $\lambda \sim 1550$  nm, at  $\lambda_{PR} \sim 635$  nm it would generally support multiple modes. During the measurement effort was made to excite only the fundamental mode, but it can be seen from Figure 4.24a that multiple transverse modes were generated. The photorefractive damage in



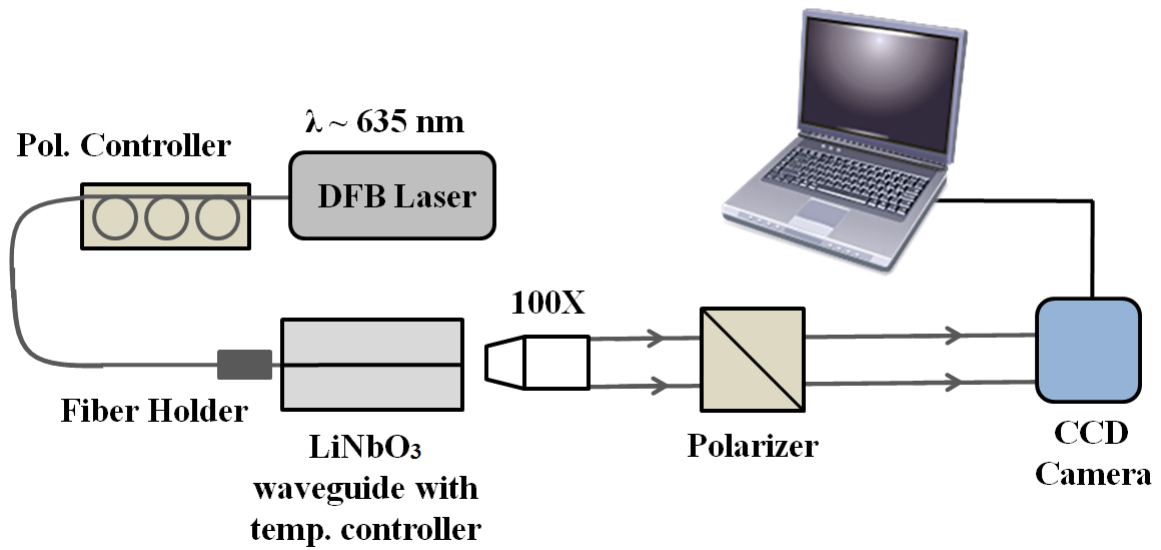


Figure 4.23: Experimental setup for investigating photorefractive damage in LiNbO<sub>3</sub> waveguides.

LiNbO<sub>3</sub> channel waveguide resulted in a catastrophic change in guided intensity profiles as shown in Figure 4.24b. Figure 4.25 shows intensity distributions of a red laser beam ( $\lambda =$

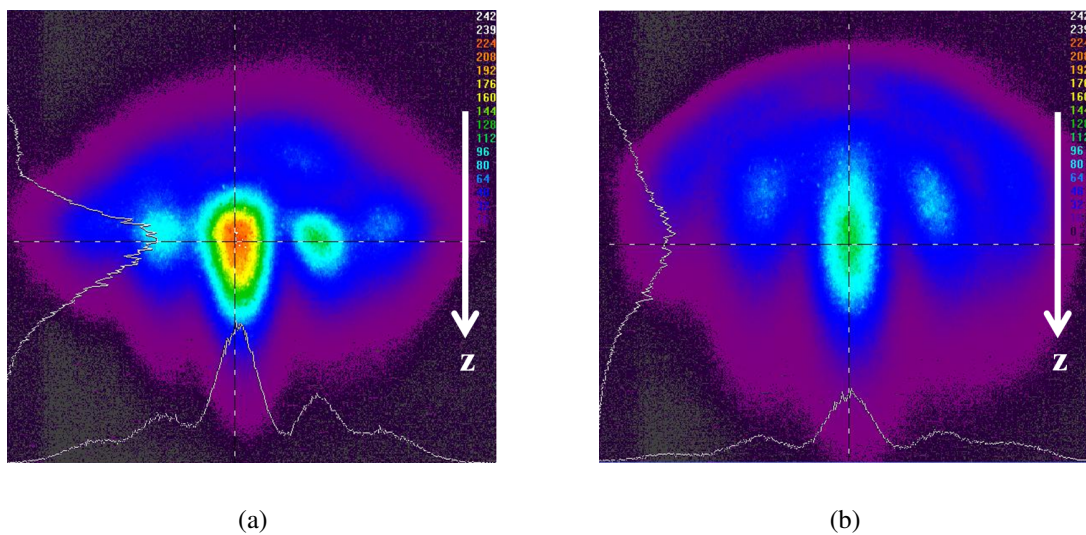


Figure 4.24: Evidence of catastrophic photorefractive damage of multimode-excited intensity distributions (extra-ordinarily polarized) in Ti-indiffused LiNbO<sub>3</sub> channel waveguide (L=30 mm) at  $\lambda_{PR} = 635$  nm ( $P_{coup} \sim 210$   $\mu$ W): (a) immediately after switching on the laser and (b) after 2 min of irradiation.

635 nm) with  $P_{coup} \sim 340$   $\mu$ W transmitted through a 30 mm long Ti-indiffused waveguide. During the measurement effort was made to excite only the fundamental mode, but it



could be possible that multiple waveguide modes might have been generated as the waveguide was designed as single-mode at  $\lambda \sim 1550$  nm. But, even then the ridge waveguide mode was found to be more stable against photorefractive damage. Thus the photorefractive

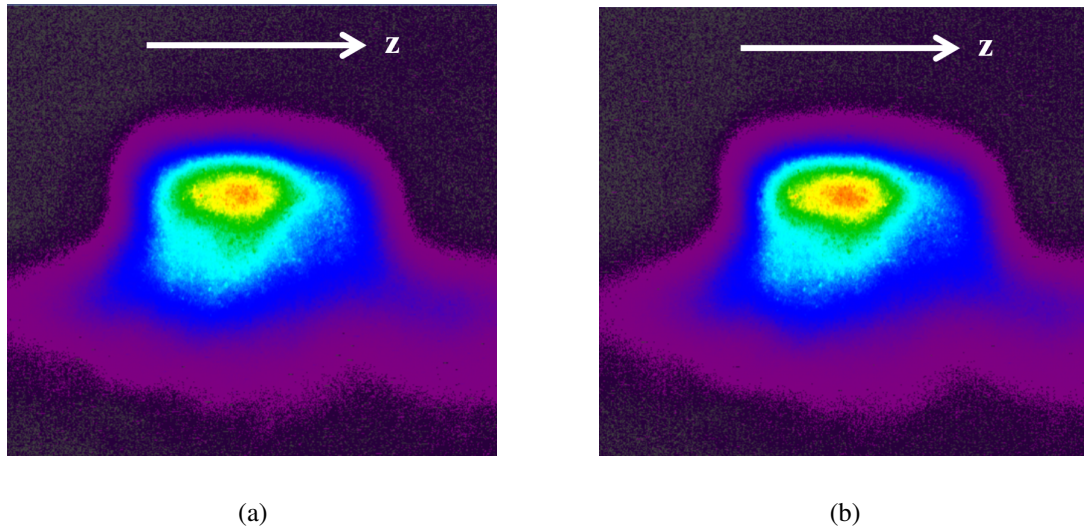


Figure 4.25: Stable intensity distributions (dominant fundamental mode and extra-ordinarily polarized) in LiNbO<sub>3</sub> ridge waveguide (L -30 mm) at  $\lambda_{PR} = 635$  nm ( $P_{coup} \sim 340$   $\mu$ W):(a) immediately after switching on the laser and (b) after 2 min of irradiation.

damage resistance of guided modes (@  $\lambda - 635$  nm) in PPLN ridge waveguides has been experimentally established and validating our theoretical prediction. The generation and detection of stable second harmonic power (@  $\lambda - 750$  nm) in PPLN ridge waveguide has been described in following section.

### 4.3.2 Second harmonic generation and characterizations

The experimental setup developed for demonstration of single-pass second harmonic generation (SHG) in PPLN waveguides has been schematically shown in Figure 4.26. An erbium-doped fiber amplifier (EDFA) pumped by a narrow-band tunable laser source ( $1510$  nm  $< \lambda_f < 1620$  nm, tunability 1 pm) was used at the waveguide input. The amplifier output was connected to a polarization controller and the polarized pump wave coming out from the polarization controller was coupled into the waveguide input using a single-mode fiber. A polarizer was placed at the waveguide output to maximize the transmission for the wave

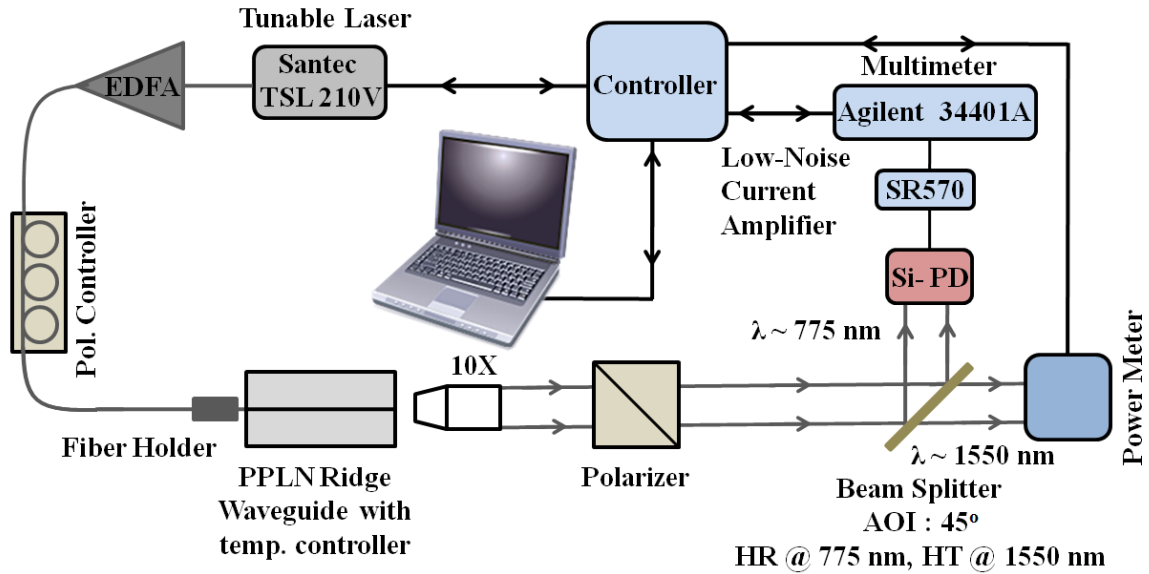


Figure 4.26: Scheme of the experimental setup used for second harmonic generation in PPLN waveguide and measurement of wavelength dependent characteristics.

with the desired polarization state by adjusting the polarization controller. At the waveguide output, the generated second harmonic wave and the residual pump wave were separated by a dichroic mirror kept after the polarizer. Both the residual pump wave and the generated second harmonic wave were simultaneously incident on the dichroic mirror at an angle  $45^\circ$ , and the residual pump wave was transmitted through the mirror, whereas the generated second harmonic wave was reflected and its power was measured by a silicon detector. The power of the transmitted residual pump wave was measured by a Si-Ge photo-detector. The backside of the dichroic mirror was coated with anti-reflection coating at 1550 nm to avoid the back-reflection of the high-power pump beam which can destabilize the laser source at the input. A stable temperature ( $\sim 30^\circ \text{C}$ ) was maintained across the entire sample, by mounting it on a temperature-controlled sample holder. Entire measurement process was controlled using a computer and the data acquisition was done with a LabVIEW program. Figure 4.27 shows the photograph of the fiber-butt coupling arrangement. Figure 4.28 shows the transmission characteristics of the dichroic mirror used for the separating the pump wave and the second harmonic wave. The curve shows high reflection for TE-polarized wave in the wavelength range  $700 \text{ nm} < \lambda < 900 \text{ nm}$  and TM-polarized wave in the range  $750 \text{ nm} < \lambda < 850 \text{ nm}$  and high transmission ( $< 98.66\%$ ) for both TE and TM-pol  $\sim 1500 \text{ nm} - 1600 \text{ nm}$ . A brief description of various samples used for second harmonic generation has been given in Table 4.3.

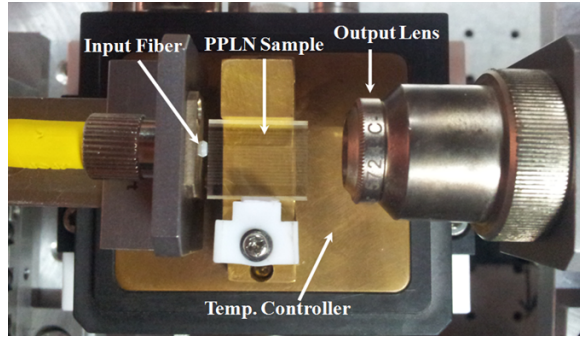


Figure 4.27: Fiber butt-coupling setup.

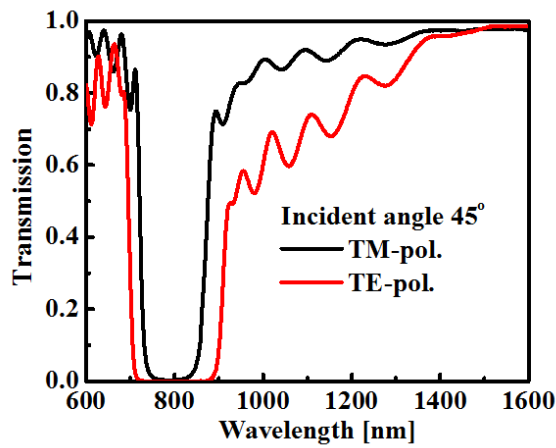


Figure 4.28: Transmission characteristics of dichroic mirror

Table 4.3: Descriptions of Ti:PPLN waveguides used for second harmonic generation.

Waveguide No.	Length [mm]	Waveguide Width [ $\mu\text{m}$ ]	$\Lambda_{QPM}$ [ $\mu\text{m}$ ]	Loss [dB/cm]
<b>Y-cut Ridge Waveguide : Pb11Y</b>				
RG1	15	$W_1 = 5.6, W_2 = 7.4,$ $R_H = 4.2$	16.1	1.80
RG2	15	$W_1 = 8.2, W_2 = 9.9,$ $R_H = 4.2$	16.1	1.20
<b>X-cut Ridge Waveguide: Pb349X</b>				
RG3	33	$W_1 = 5.6, W_2 = 6.7,$ $R_H = 3.0$	16.1	1.19
<b>Reference (Z-cut) Channel Waveguide</b>				
CH1	25	$W = 7.0$	16.5	0.5
CH2	36	$W = 7.0$	16.5	0.1

**Second Harmonic phase matching characteristics of PPLN ridge waveguides over wide pump wavelength range :** Figure 4.29 shows the second harmonic phase matching characteristics of ridge waveguides for a wider pump wavelength range. Figure 4.29a shows that

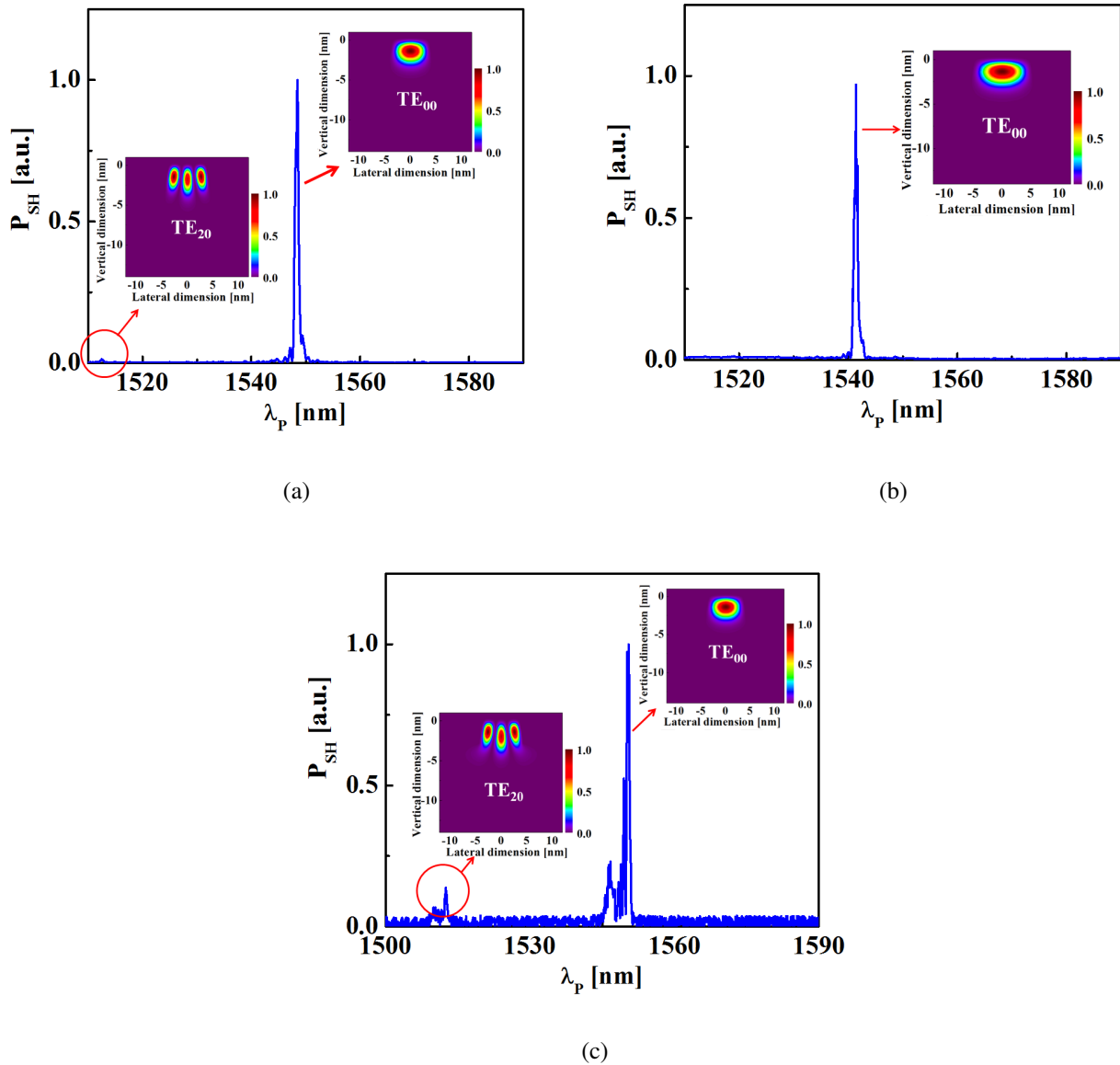
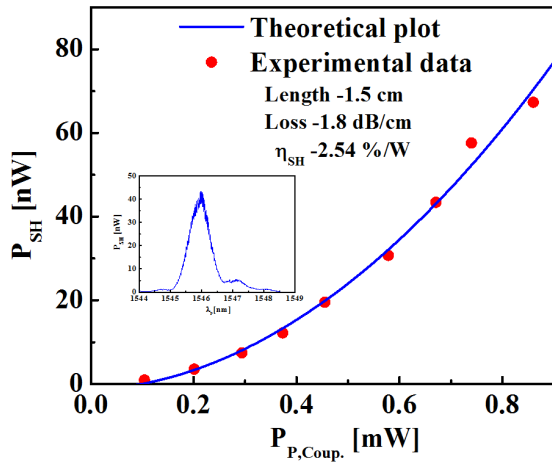


Figure 4.29: Second harmonic tuning characteristics of PPLN ridge waveguides for a broad pump wavelength range:(a) Waveguide # RG1 (Y-cut ridge waveguide);(b) Waveguide # RG2 (Y-cut ridge waveguide)and (c) Waveguide # RG3 (X-cut ridge waveguide).

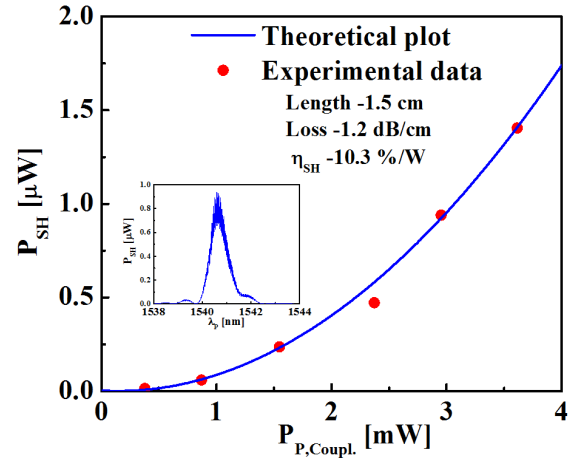
phase-matching curve for the X-cut ridge waveguide # RG3. The waveguide was phase-matched for second harmonic generation  $\lambda_p$  - 1550.5 nm at a temperature 30° C. Additionally, the waveguide was found to be phase-matched at  $\lambda_p$  - 1512.5 nm, but the generated

second harmonic power at the secondary peak as low as 13.8 % of the generated power at the main peak. The main peak is due to Pump( $TE_{00}$ )  $\rightarrow$  SH( $TE_{00}$ ) conversion, whereas the secondary peak is due to Pump( $TE_{00}$ )  $\rightarrow$  SH( $TE_{20}$ ) conversion. Since the effective area of mode overlap between the Pump( $TE_{00}$ ) mode and SH( $TE_{20}$ ) mode is very large compared to the same between Pump( $TE_{00}$ ) and SH( $TE_{00}$ ) modes, hence corresponding conversion efficiency is also very small. Similarly, Figure 4.29b shows that phase-matching curve for the Y-cut ridge waveguide # RG1. According to the curve, the waveguide is phase-matched at  $\lambda_p - 1548.5$  nm at a device temperature  $30^\circ$  C. A secondary phase-matched wavelength was also observed at  $\lambda_p \sim 1512.5$  nm, with the generated second harmonic power nearly 1.1 % of the generated power at the main peak. Figure 4.29c shows that phase-matching curve for the Y-cut ridge waveguide # RG2. The waveguide was found to be phase-matched for second harmonic generation only at  $\lambda_p - 1548.5$  nm at a temperature  $30^\circ$  C. It did not have any additional peak due to higher order second harmonic conversion. According to the design all waveguides should have unique second harmonic phase-matched wavelength for a given sample temperature. But, due to waveguide non-uniformity and fabrication errors existence of additional peaks due to conversion fundamental mode of the pump wave and higher order modes of the second harmonic wave was observed with very poor conversion efficiency.

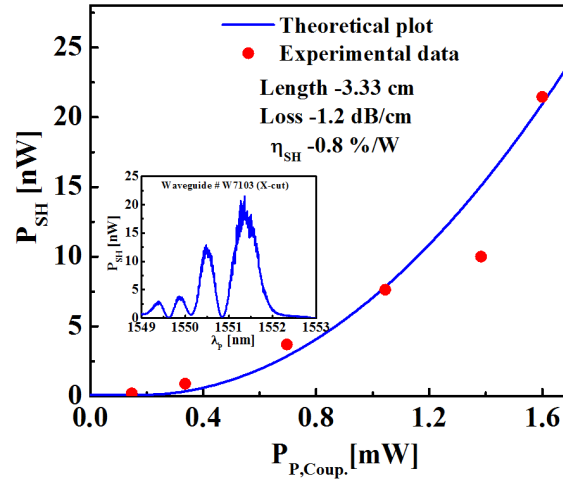
**Second Harmonic Tuning Characteristics at Low Pump Power :** Second harmonic wave generation was investigated in X-cut and Y-cut PPLN ridge waveguides near room temperature ( $\sim 25^\circ$  C). During the entire measurement process the device temperature was controlled and made stable using a temperature controller. Figure 4.30 shows the second harmonic tuning characteristics as a function of pump wavelength at low fundamental power level. In Figure 4.30a tuning characteristics for the waveguide # RG3 (X-cut ridge waveguide) has been shown. The waveguide was found to be phase-matched at  $\lambda_p \sim 1550.5$  nm at room temperature, but the conversion efficiency for the second harmonic generation was found to be very poor, as low as  $\sim 0.8$  %/W. Higher propagation loss of the pump beam within the waveguide, waveguide non-uniformity and non-ideal ferroelectric domain structures could be responsible for this. The waveguide non-uniformity was clearly evident from phase-matching curve as shown in inset of Figure 4.30a. Figure 4.30b and Figure 4.30c shows the phase-matching characteristics of Y-cut ridge waveguides RG1 and RG2 respectively. Waveguide # RG1 was found to be phase-matched at  $\lambda_p - 1548.5$  nm at room temperature and the conversion efficiency for the generated second harmonic power



(a)



(b)



(c)

Figure 4.30: Second harmonic tuning characteristics of PPLN ridge waveguides at 25° C : (a) Waveguide # RG1 (Y-cut ridge waveguide); (b) Waveguide # RG2 (Y-cut ridge waveguide) and (c) Waveguide # RG3 (X-cut ridge waveguide).

was 2.54%/W. Waveguide # RG2 was found to be phase-matched at  $\lambda_P$  - 1540.6 nm at room temperature and the conversion efficiency for the generated second harmonic power was relatively better  $\sim 10.3\%/W$ . Figure 4.31 shows the second harmonic tuning characteristics of reference channel waveguides as a function of pump wavelength at low fundamental power level at room temperature. The reference channel waveguides were found to have higher second harmonic conversion due to their low propagation losses and better domain quality.

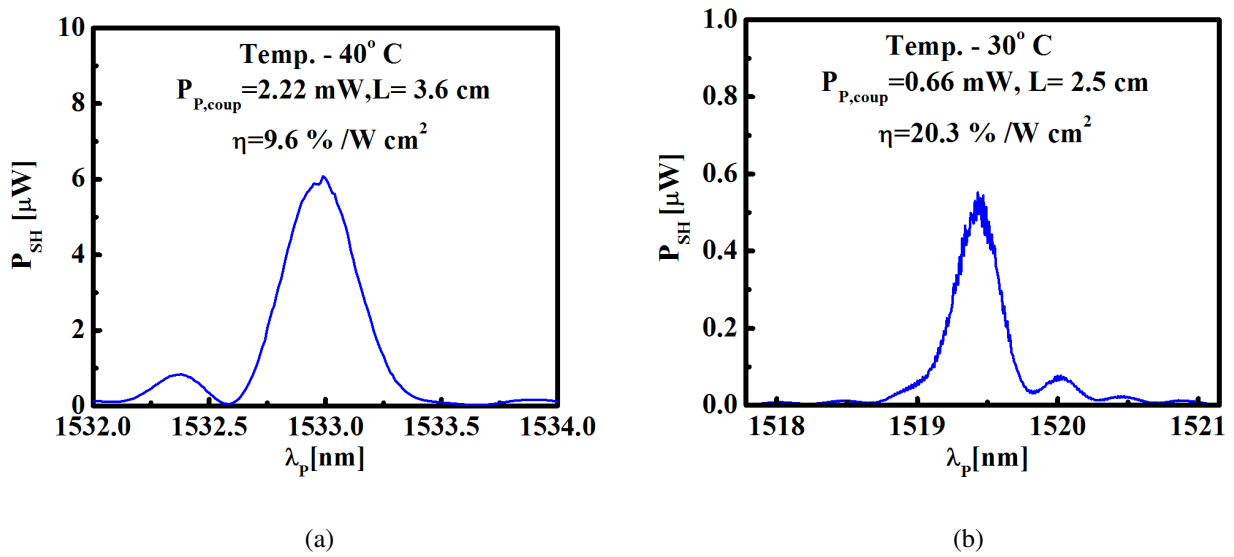


Figure 4.31: Second harmonic tuning characteristics of reference (Z-cut PPLN channel) waveguides at 30° C :(a) Waveguide # CH1; (a) Waveguide # CH2.

**Tuning characteristics of PPLN waveguides at higher pump power :** The spectral characteristics and stability of the generated SH-power in PPLN waveguides at higher pump power has been studied in detail. Figure 4.32 shows the photorefractive effect of the generated second harmonic power on the PPLN channel waveguide near room temperature. With

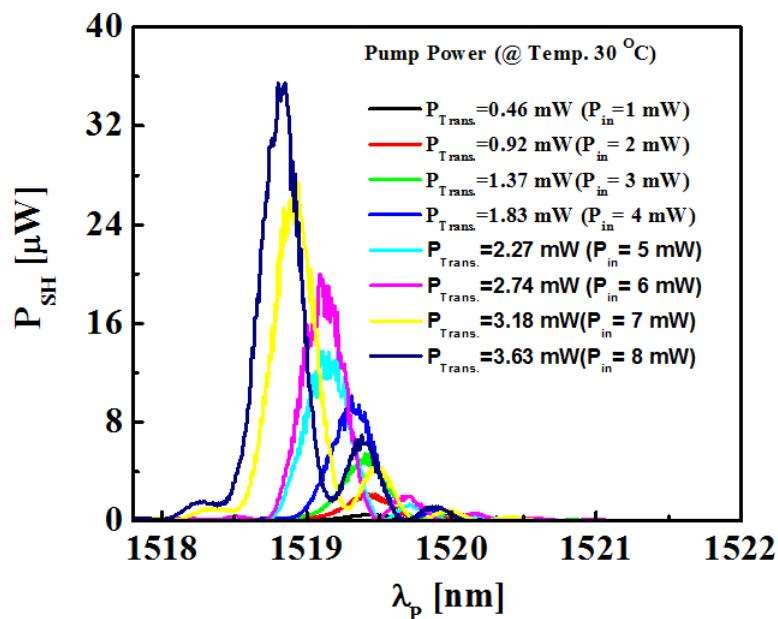
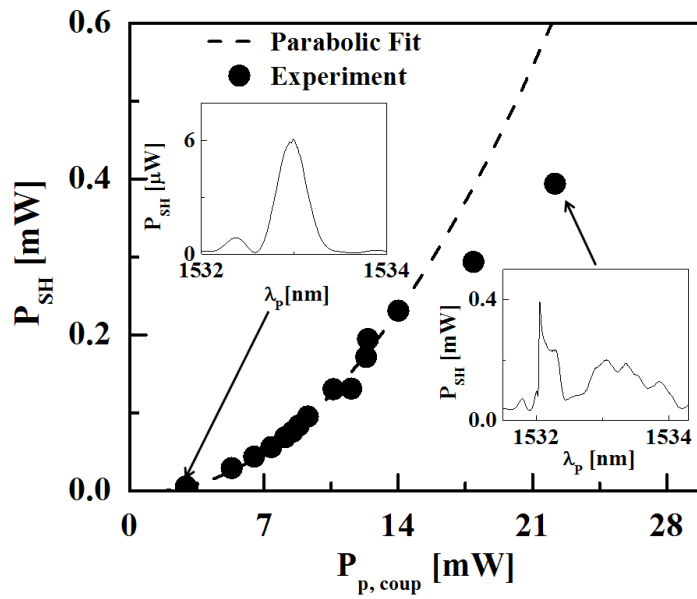
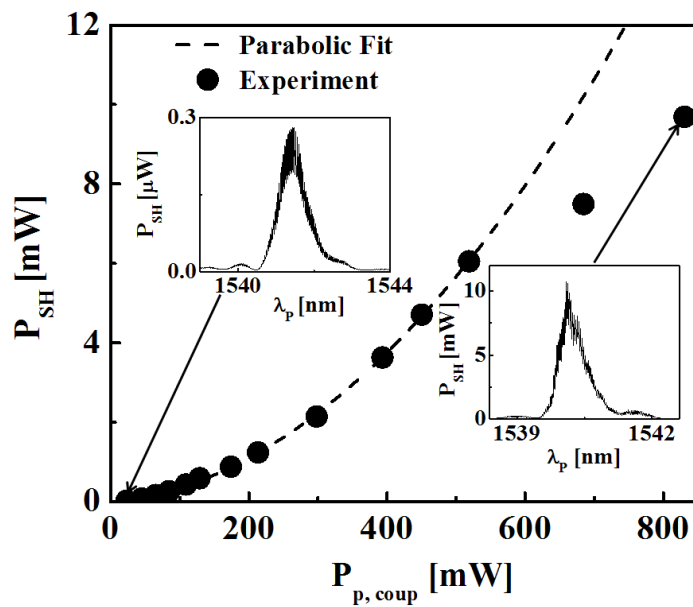


Figure 4.32: Photorefractive effect of increasing second harmonic power on PPLN channel waveguide at room temperature.

the increase in second harmonic power in the waveguide there was considerable blue-shift in the phase-matching wavelength due to photorefraction.  $P_{SH} \sim 35 \mu\text{W}$  was able to produce



(a)



(b)

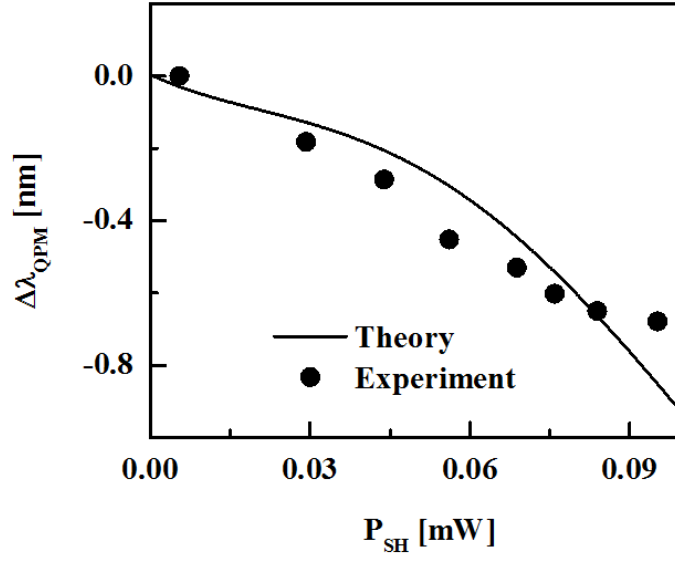
Figure 4.33: SHG power characteristics for Ti:PPLN waveguides as SH-power  $P_{SH}$  versus coupled pump power  $P_{p,coup}$  measured at  $40^\circ\text{C}$  (channel) and  $30^\circ\text{C}$  (ridge): (a) Ti:PPLN channel, (b) Ti:PPLN ridge guide. The insets show phase match characteristics at different power levels.



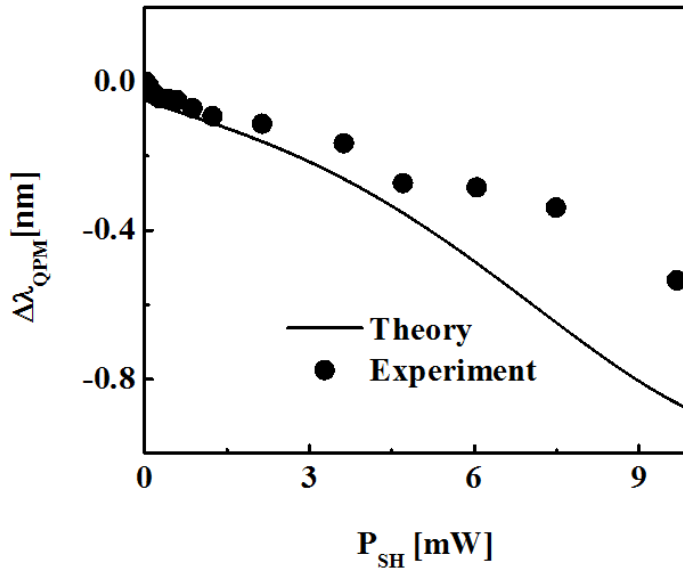
blue-shift nearly 1 nm. This shows the higher sensitivity of the PPLN channel waveguide to photorefractive damage near room temperature. This photorefractive damage increases considerably with the further increase in the second harmonic power.

Figure 4.33 shows the SH-power as function of the coupled pump power for both types of waveguides measured at 40°C (channel) and at 30°C (ridge) together with phase match characteristics as insets. The higher temperature of the channel guide was necessary to shift its phase match wavelength into the range accessible by the EDFA. The SH-power characteristics of the channel guide shows a parabolic dependence up to  $P_{SH} \sim 0.23$  mW (@  $P_{p,coup} \sim 14$  mW) in accordance with theory. At higher SH-power levels photorefractive damage set in, seriously deteriorating the phase match characteristics (shown at the right inset of Fig.4.33) and the generated SH-power could increase at a much reduced rate. On the other hand, the SH-power characteristics of the ridge guide showed a parabolic dependence with increasing pump power even up to  $P_{SH} \sim 6$  mW (@  $P_{p,coup} \sim 520$  mW). Moreover, the initial phase match characteristics remain nearly undistorted (see insets of Fig. 4.33), though a small initial blue-shift was observed in accordance with the result presented in Fig. 4.36. The Ti:PPLN ridge guide has at SH-power levels up to several milliWatts a much better temporal stability of the generated SH-power than a conventional channel waveguide.

The detuning of the phase-match wavelength  $\Delta\lambda_{QPM}$  due to the onset of photorefractive damage was investigated as function of the generated SH-power. It has been shown in Figure 4.34a for a channel waveguide (up to  $P_{SH} \sim 90$   $\mu$ W) and in Figure 4.34b for a ridge waveguide (up to  $P_{SH} \sim 9$  mW). The results were obtained by increasing the input pump power level in steps and subsequently scanning the pump wavelength around phase matching; the initial wavelength shift  $\Delta\lambda_{QPM}$  with respect to the phase match wavelength at very low pump power is displayed in Figure 4.34b. The blue-shifts of the phase-matched wavelengths, which are much stronger in the channel guide, are attributed to the change of the effective (extraordinary) refractive index of the waveguide due to photorefractive damage by the generated SH wave. These results are in qualitative agreement with our theoretical considerations demonstrating the substantially higher stability of the ridge guides: SH-power levels of about two orders of magnitude higher are required to induce a comparable shift of the phase match wavelength. The large deviation of experimental results from the theoretical predictions for the ridge waveguide is not due to a measurement error as we could determine the phase matching wavelength within  $\pm 1$  pm. The deviation has been attributed to the heating ef-



(a)



(b)

Figure 4.34: Detuning of the phase match wavelength  $\Delta\lambda_{QPM}$  due to the onset of photorefractive by the generated SH power  $P_{SH}$  for both types of waveguides: (a) Ti:PPLN channel and (b) Ti:PPLN ridge guide.

fects (at higher pump power levels) which were not considered in the theoretical model.

The detuning of the phase-matching wavelength as function of the sample temperature has been obtained experimentally for both channel and ridge waveguides as shown in Figure 4.35. Tuning slopes were found to be nearly identical; which are mainly determined by

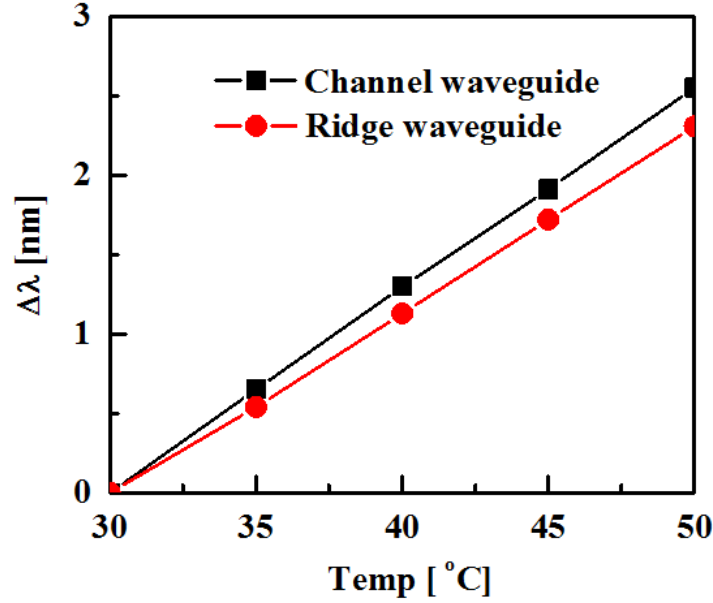
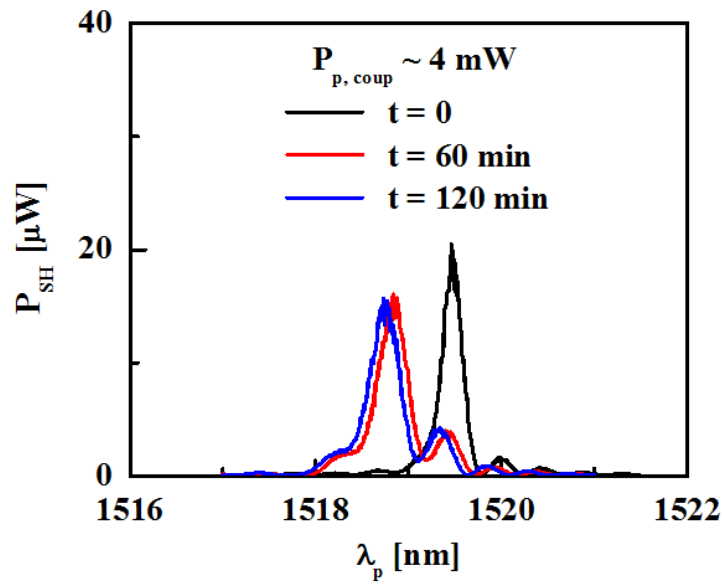


Figure 4.35: Detuning  $\Delta\lambda$  of the phase matching wavelength versus the sample temperature for both types of waveguides.

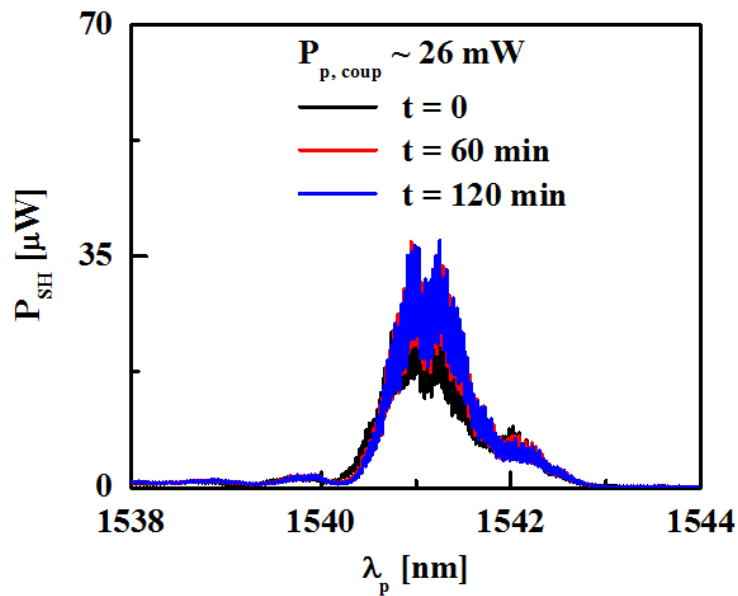
the temperature-dependence of the extraordinary index of refraction. Since, lithium niobate is a thermally insulating material, at higher pump power level there might be local generation of temperature gradient within the waveguide. The temperature measured during the experiment was actually the oven temperature, and there might be considerable difference between the actual temperature within the waveguide (which is difficult to measure very accurately) and the oven temperature. The difference between the theoretically obtained temperature detuning (as shown in Figure 3.11a) and the experimentally obtained value (shown in Figure 4.35) can be attributed to this.

**Effect of Photorefraction on Ridge Waveguides :** With increasing coupled pump power, the second harmonic conversion efficiency in Ti: PPLN channel waveguides deteriorates very rapidly due to the photorefractive effect. This effect is very serious in waveguides operated near room temperature; a second harmonic power in the micro-Watt range is sufficient to induce considerable photorefractive damage deteriorating the SHG-efficiency. This damage increases fast with increasing second harmonic power and may finally destroy the guiding characteristics completely. On the contrary, we observed that the photorefractive susceptibility of our ridge guides was much lower. It was possible to generate much higher SH-power levels (up to several mW) even at room temperature and maintain the phase matching condition. This is a consequence of the higher refractive index contrast of the

ridge guides. To quantify these observations we studied the temporal evolution of the pho-



(a)



(b)

Figure 4.36: SHG phase matching characteristics for Ti:PPLN waveguides as SH-power  $P_{SH}$  versus pump wavelength  $\lambda_p$  measured with different (coupled) pump power levels  $P_{p,coup}$  after 0, 60 and 120 mins. at room temperature ( $30^\circ\text{C}$ ): (a) Ti:PPLN channel, (b) Ti:PPLN ridge.

to refractive effects for both types of waveguides. At first, low pump power levels of  $P_{p,coup}$

$\sim 4$  mW (channel) and  $P_{p,coup} \sim 26$  mW (ridge) were used (different pump power levels were used to generate a same level of second harmonic power of  $\sim 20$   $\mu$ W). This study was done by observing the phase matching characteristics as a function of time keeping the samples nearly at room temperature ( $\sim 30^\circ$  C). Three different phase matching curves were measured with both, the channel and the ridge guide, by tuning the pump wavelength quickly around  $\lambda_{p,pm}$  after  $t = 0, 60,$  and  $120$  mins, respectively (see Figure 4.36a and 4.36b). The result clearly demonstrates a photorefractive damage induced blue-shift of the phase-matching wavelength of the PPLN channel waveguide (Fig. 4.36a), whereas for the ridge guide the corresponding characteristics remains stable as theoretically expected at low pump power levels (Fig. 4.36b). It was even possible to increase the pump power, coupled to the ridge guide, up to several hundred milliWatts without a significant immediate change of the phase matching characteristics. However, it was found to drift with time considerably. Figure 4.37

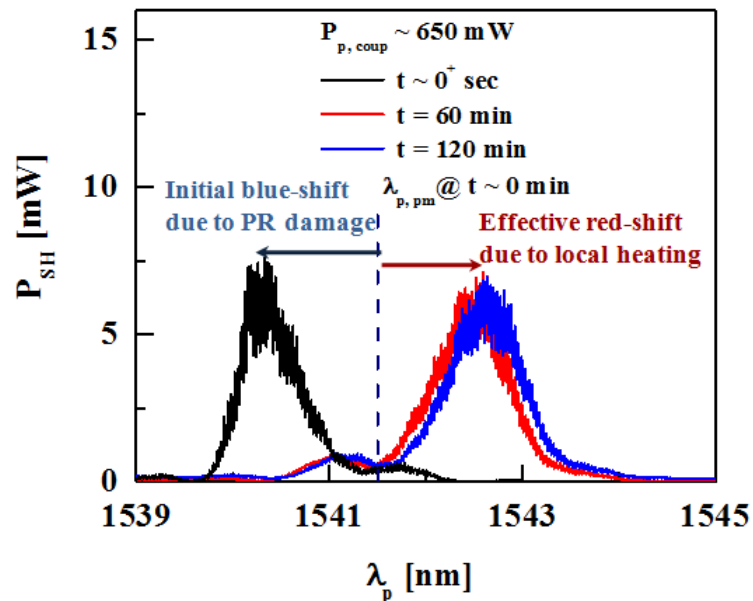


Figure 4.37: SHG phase matching characteristics for Ti:PPLN ridge guides as SH-power  $P_{SH}$  versus pump wavelength  $\lambda_p$  measured with a coupled pump power  $P_{p,coup} = 650$  mW after  $0^+$ , 60 and 120 min at room temperature ( $30^\circ$  C). Blue- and red-shifts were observed with time.

shows as example the photorefractive damage dynamics of a Ti:PPLN ridge guide for a coupled pump power of  $P_{p,coup} \sim 640$  mW. Initially (at  $t = 0^+$  sec) a relatively fast blue-shift ( $\sim 1.0$  nm) was observed shifting the phase match wavelength from  $\sim 1541.5$  nm Fig. 4.35 to  $\sim 1540.4$  nm (Fig.4.37). However, after 60 and 120 min, we noticed a considerable red-

shift of about  $\Delta\lambda \sim 1.5$  nm (with respect to room-temperature phase-matching wavelength). This is due to internal heat generation in the waveguide by partial absorption during high power pumping over a long period of time; the initial blue-shift was over-compensated by the red-shift due to local temperature increase of the waveguide. From the experimental data it can be estimated that this wavelength shift could correspond to a local rise in temperature inside the waveguide  $\sim 40^\circ$  C. Such a red-shift due to a local temperature rise in a PPLN waveguide was also reported earlier [91].

**Stability in Second Harmonic Power :** Figure 4.38 shows the stability of the generated second harmonic wave inside the waveguide as a function of time. The measurement was

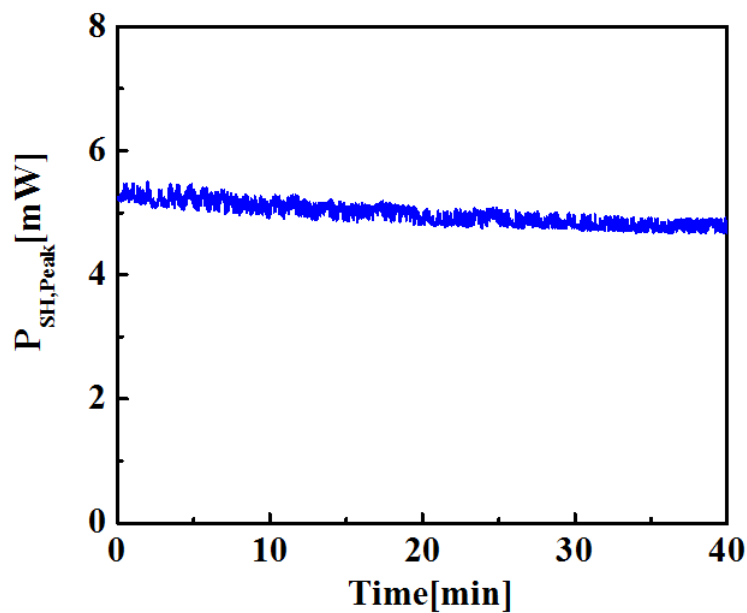


Figure 4.38: Room temperature stability of generated second harmonic power in ridge waveguide.

carried out by setting the pump laser at the peak phase-matched wavelength and recording the corresponding generated second harmonic power. The fluctuation in the second harmonic power during the measurement could be actually due to the fluctuation in the power level of the pump laser. Also slight downward slope of the measured second harmonic power could be due to change in the coupling condition over time.

## 4.4 Conclusions

In this chapter initially preliminary experimental studies related to of APE-waveguides have been discussed. APE-channel waveguides were fabricated on X-cut LiNbO<sub>3</sub>. These waveguides were found to have polarization extinction ratio  $> 35$  dB for the ordinarily polarized light. Then various etching techniques on X-cut LiNbO<sub>3</sub> have been discussed for the realization of the ridge structure. The wet-etching in X-cut LiNbO<sub>3</sub> was found not suitable for ridge waveguide fabrication as it is extremely slow process, also lateral etching was observed below the mask due to very long etching time. Then dry etching (RIE) of X-cut LiNbO<sub>3</sub> was investigated using CHF<sub>3</sub>:Ar and SF<sub>6</sub>:Ar combination. Initially, the etch rate was slower due to the generation of LiF. Subsequently, to reduce the generation of LiF and improve the etch rate, the substrate surface was activated using proton exchange prior to reactive ion etching (RIE). As a result, the etch rate was improved, but the surface activation process resulted in surface damage due to excessive stress generated on the surface. Also after dry etching, a white residue (Nb<sub>2</sub>O<sub>5</sub>) was found to be deposited on the surface which could not be removed even after HF/HNO<sub>3</sub> cleaning.

Subsequently, the fabrication flow of Ti-indiffused PPLN ridge waveguides have been discussed. Ridge structures were realized by ICP-RIE using C<sub>4</sub>F<sub>8</sub>/He chemistry. Subsequently, waveguides were fabricated by Ti-indiffusion only in the ridge region. Fabricated waveguides were periodically poled by applying voltage across the ridge using comb-like electrodes. PPLN ridge were found to have relatively higher propagation-loss ( $\sim 1.2$  dB/cm) due to their sidewall roughness. After waveguide fabrication, investigation of photorefractive damage resistance and second harmonic generation were carried out on fabricated PPLN ridge waveguides and reference PPLN channel waveguides. Initially photorefractive damage resistant characteristics was investigated on both channel and ridge waveguide @  $\lambda \sim 0.635$   $\mu\text{m}$ . As expected, the weak modal confinement in PPLN channel waveguide resulted in catastrophic change in waveguide characteristics, whereas the PPLN ridge waveguides showed much better modal stability due to its higher refractive index contrast. Subsequently, second harmonic generation experiments were carried out at in both PPLN ridge and also in reference channel waveguides. It has been observed that the PPLN ridge waveguide (length - 15 mm) could generate and sustain  $P_{SH} > 10$  mW at room temperature without significant degradation of the phase-matching characteristics, whereas in case of channel

waveguide (length - 36 mm)  $P_{SH} \sim 0.4$  mW could completely destroy the phase matching characteristics under similar experimental conditions. Hence, it can be concluded that PPLN ridge waveguides are far more superior in terms of tolerance against photorefractive damage compared to PPLN channel waveguides.



# CHAPTER 5

## Conclusions

In this work, titanium-indiffused PPLN channel and ridge waveguides have been theoretically analyzed for efficient second harmonic generation and the photorefractive damage-resistant characteristics in PPLN ridge waveguide has been explained. The theoretical prediction has been validated by carrying out various experimental investigations on PPLN ridge and channel waveguides. The chapter-wise summary of the thesis outcome and future scope of work have been discussed below.

### 5.1 Summary

In chapter 1, a detailed literature survey on  $\text{LiNbO}_3$  integrated optical devices has revealed that PPLN channel waveguides are very much interesting for all-optical signal processing and various other practical applications due to their lower propagation-loss and very high conversion efficiency. But, these waveguides are sensitive to photorefractive damage at near-IR wavelengths ( $< 900$  nm) which inhibits their high power applications. Prior to this thesis work it was observed that the PPLN ridge waveguides have very high threshold against photorefractive damage near room temperature and these can generate and sustain very high power second harmonic waves without significant degradation. However, there was no literature available explaining work till date explaining the physics and mechanism of the damage resistant characteristics.

In chapter 2, the origin of photorefractive effect has been reviewed to quantify the photorefraction in bulk  $\text{LiNbO}_3$  and then an analytical formula has been proposed to model the modified refractive index profile of ridge/channel waveguides.

In chapter 3, Ti-indiffused PPLN ridge and channel waveguides have been theoretically analyzed for single-mode guidance and optimum modal confinement. For the ridge

waveguide the effective modal area has been found to be  $A_{eff} \sim 23 \mu\text{m}^2$  (width -  $7 \mu\text{m}$ , ridge height -  $4 \mu\text{m}$ ) and that for the channel waveguide is  $\sim 54 \mu\text{m}^2$  (width -  $7 \mu\text{m}$ ) @  $\lambda \sim 1550 \text{ nm}$  when fabricated with standard fabrication parameters (Ti-layer thickness -  $100 \text{ nm}$ , diffusion time -  $8.5 \text{ hours}$ , temperature -  $1060^\circ \text{ C}$ ). Thus it has been shown that with the same input power level much higher pump intensity can be generated inside a ridge waveguide in comparison to that of single-mode optimized Ti-indiffused channel waveguide. Afterwards, the photorefractive damage resistance in PPLN ridge and channel waveguides have been theoretically analyzed using two-center model. It has been shown that, in case of a PPLN channel waveguide the pump mode nearly reaches the cut-off condition at  $P_{SH} - 200 \mu\text{W}$  due to photorefractive index change, whereas the in case of ridge waveguide the pump mode remained well confined even at  $P_{SH} - 50 \text{ mW}$ . As expected, the detuning of the phase-matched wavelength in case of PPLN channel waveguide ( $\Delta \lambda_{QPM} \sim 1 \text{ nm}$  @  $P_{SH} - 100 \mu\text{W}$ ) was also found to much larger compared to the PPLN ridge waveguide ( $\Delta \lambda_{QPM} \sim 1 \text{ nm}$  @  $P_{SH} - 10 \text{ mW}$ ). Better modal stability as well as higher photorefractive damage threshold in PPLN ridge waveguides can be attributed to its stronger modal confinement.

In chapter 4, initially the fabrication process flow for the APE-channel waveguides have been discussed. Then preliminary studies on various etching techniques in  $\text{LiNbO}_3$  have been presented and different challenges faced towards realization of  $\text{LiNbO}_3$  ridge structures have been discussed. Finally, Ti:PPLN waveguide fabrication process carried out at Technology Laboratory, Integrated Optics Group in University of Paderborn have been discussed. Then various second harmonic generation and photorefractive damage related experiments carried using fabricated Ti:PPLN waveguides at IIT Madras have been presented. From second harmonic measurement results it was observed that the PPLN ridge waveguide have indeed much higher photorefractive damage threshold near room temperature, it could sustain  $P_{SH} \sim 10 \text{ mW}$  (@  $\lambda 775 \text{ nm}$ ) without significant degradation of the phase-matching characteristics, and also the generated second harmonic power was stable over time. But, the phase matching characteristics of the PPLN channel waveguide was completely destroyed at  $P_{SH} \sim 0.4 \text{ mW}$  due to its poor photorefractive damage threshold. As expected the photorefractive wavelength detuning was also found to be much higher in case of PPLN channel waveguide compared to the ridge waveguide.

## 5.2 Future Scope of Work

Within the scope of present thesis work, it has been shown that PPLN ridge waveguides have much higher threshold for photorefractive damage compared to diffused channel waveguides by both theoretical calculations and subsequent experimental investigations. All calculations related to photorefractive damage inside PPLN waveguides have been carried out assuming quasi-steady state condition i.e. any change in modal characteristics due to photorefraction is essentially a function of the incident intensity. But, according to two-center model the photo-refractive space-charge field is also a function of time. For an accurate estimation of the space-charge field in PPLN waveguides, the time-dependence part has to be included. The space-charge field in PPLN ridge waveguides also depends on the surface conductivity and density of surface states, which could play a role in the photorefractive damage threshold. The surface charge recombination velocity needs to be considered in the estimation of actual refractive index change due to photorefractive effect. The photorefractive damage threshold for a given waveguide depends on the waveguide quality (e.g. waveguide uniformity, propagation-loss etc.), domain structures and their orientations. The quality of fabricated PPLN ridge waveguides can be improved further by reducing propagation losses, quality of inverted ferroelectric domains. Optimized and photorefractive damage resistant PPLN ridge waveguides can be used to realize highly efficient, ultra-compact and versatile wavelength converter for high-power applications near room temperatures.

# APPENDIX A

## Nonlinear Propagation Equations for Three-Wave Mixing

### A.0.1 Nonlinear Propagation Equations for Three-Wave Mixing

The following derivation nonlinear propagation equation is based on the work available from various literature [145, 146, 147]. An electromagnetic wave propagates in a waveguide as a collection of oscillating fields, which interfere constructively and destructively. Whenever these oscillating fields interfere constructively within the waveguide and certain boundary conditions are fulfilled, a guided optical mode is generated. The propagation equation of an electromagnetic wave in a linear, isotropic, homogeneous, charge-free and lossy dielectric medium can be written as:

$$\nabla \cdot \vec{D} = 0 \quad (\text{A.1a})$$

$$\nabla \cdot \vec{B} = 0 \quad (\text{A.1b})$$

$$\nabla \times \vec{E} = -\frac{\partial \vec{B}}{\partial t} \quad (\text{A.1c})$$

$$\begin{aligned} \nabla \times \vec{B} &= \mu_0 \vec{J} + \mu_0 \frac{\partial \vec{D}}{\partial t} \\ &= \mu_0 \sigma \vec{E} + \mu_0 \frac{\partial \vec{D}}{\partial t} \end{aligned} \quad (\text{A.1d})$$

Here,  $\vec{E}$ ,  $\vec{D}$ ,  $\vec{H}$ ,  $\vec{B}$  and  $\vec{J}$  are electric field, electric displacement, magnetic field, magnetic induction and current density respectively. It has been assumed that the lossy dielectric material behaves as a partially conducting material i.e  $\sigma \neq 0$  and the medium is non-magnetic.

Hence, it can be written as:

$$\vec{B} = \mu_0 \vec{H} \quad (\text{A.1e})$$

and

$$\vec{D} = \epsilon \vec{E} + \vec{P}_{NL} \quad (\text{A.1f})$$

Here,  $\vec{P}_{NL}$  is the nonlinear polarization vector and  $\epsilon$  is the permittivity of the medium. Using Equation (A.1a) to (A.1f), the nonlinear wave equation can be written as:

$$\nabla^2 \vec{E} - \mu_0 \epsilon \frac{\partial^2 \vec{E}}{\partial t^2} - \mu_0 \sigma \frac{\partial \vec{E}}{\partial t} - \mu_0 \frac{\partial^2 \vec{P}_{NL}}{\partial t^2} = 0 \quad (\text{A.2})$$

The nonlinear polarization term can be written as:

$$\vec{P}_{NL} = \epsilon_0 [\chi^{(2)} \cdot \vec{E}\vec{E} + \chi^{(3)} \cdot \vec{E}\vec{E}\vec{E} + \chi^{(4)} \cdot \vec{E}\vec{E}\vec{E}\vec{E} + \dots] \quad (\text{A.3})$$

If all interacting waves are linearly polarized in a particular direction and these waves are propagating along z-axis in a linearly isotropic medium, the wave equation Equation (A.2), and the nonlinear susceptibility tensors of Equation (A.3) can be written in scalar form. For LiNbO<sub>3</sub>, second-order nonlinear susceptibility is most prominent term. Hence, ignoring all higher-order nonlinear susceptibilities, the nonlinear polarization vector  $\vec{P}_{NL}$  can be written as:

$$\vec{P}_{NL} = \epsilon_0 [\chi^{(2)} \cdot \vec{E}\vec{E}] \quad (\text{A.4})$$

For generalized three-wave mixing, the total electric field can be written as:

$$E = E_1 + E_2 + E_3 \quad (\text{A.5})$$

where

$$E_i = \frac{1}{2} \left[ \tilde{E}_i(x, y, z, t) \exp[j(\omega_i t - \beta_{0,i} z)] + c.c. \right] \quad (\text{A.6})$$

Substituting Equation (A.5) into Equation (A.2) and then using the permutation symmetry in  $\chi_{ijk}^{(2)}$  along with the frequency matching condition  $\omega_3 = \omega_1 + \omega_2$ , the second-order nonlinear polarization term  $P_{NL,i}^{(2)}$  can be written as:

$$P_{NL,1} = \epsilon_0 \chi^{(2)} \cdot \tilde{E}_2^* \tilde{E}_3 \quad (\text{A.7a})$$

$$P_{NL,2} = \epsilon_0 \chi^{(2)} \cdot \tilde{E}_1^* \tilde{E}_3 \quad (\text{A.7b})$$

$$P_{NL,3} = \epsilon_0 \chi^{(2)} \cdot \tilde{E}_1 \tilde{E}_1 \quad (\text{A.7c})$$

Under the plane wave approximation, Equation (A.2) is converted into a scalar equation and it can be written as:

$$\frac{\partial^2 \tilde{E}_i}{\partial z^2} - \mu_0 \epsilon \frac{\partial^2 \tilde{E}_i}{\partial t^2} - \mu_0 \sigma \frac{\partial \tilde{E}_i}{\partial t} - \mu_0 \frac{\partial^2 \tilde{P}_{NL,i}^{(2)}}{\partial t^2} = 0 \quad (i = 1, 2, 3) \quad (\text{A.8})$$

Taking Fourier Transform of Equation (A.8) one can write:

$$\frac{\partial^2 \hat{E}_i}{\partial z^2} + \mu_0 \epsilon(\omega) \omega^2 \hat{E}_i - j \mu_0 \sigma \omega \hat{E}_i + \mu_0 \omega^2 \hat{P}_{NL,i}^{(2)} = 0 \quad (i = 1, 2, 3) \quad (\text{A.9})$$

If the nonlinear effect is weak enough such that the waveguide transverse mode does not change much during it's propagation, the electric field  $\hat{E}_i$  can be written as:

$$\hat{E}_i(x, y, z, \omega - \omega_i) = \gamma_i F_i(x, y) \hat{A}_i(z, \omega - \omega_i) \exp[-j \beta_{0,i} z] \quad (\text{A.10})$$

where  $F_i(x, y)$  is the mode distribution,  $\hat{A}_i(z, \omega - \omega_i)$  is the spectral envelope and

$$\gamma_i = \left[ \frac{2}{c \epsilon_0 n_i} \right]^{\frac{1}{2}} \quad (\text{A.11})$$

F is in general a complex parameter and it can be normalized as follows:

$$\int_{-\infty}^{\infty} \int_{-\infty}^{\infty} |F_i(x, y)|^2 dx dy = 1 \quad (\text{A.12})$$

$\hat{A}_i(z, \omega - \omega_i)$  represents the power of the envelope and it has an unit  $W^{\frac{1}{2}}$ . Then substituting Equation (A.10) into Equation (A.9) and using the slowly varying envelop approximation and dispersive nature of the material one can write that:

$$F_i \left[ \frac{\partial \hat{A}_i}{\partial z} + j \beta_{1,i}(\omega - \omega_i) \hat{A}_i + j \frac{1}{2} \beta_{2,i}(\omega - \omega_i)^2 \hat{A}_i + \frac{\mu_0 \sigma \omega}{2 \beta_{0,i}} \hat{A}_i \right] + j \frac{\mu_0 \omega^2}{2 \gamma_i \beta_{0,i}} \hat{P}_{NL,i}^{(2)} = 0 \quad (\text{A.13})$$

Converting Equation (A.13) into time domain and rearranging various terms one can write:

$$F_i \left[ \frac{\partial A_i}{\partial z} + \beta_{1,i} \frac{\partial A_i}{\partial t} - j \frac{1}{2} \beta_{2,i} \frac{\partial^2 A_i}{\partial t^2} + \frac{\alpha_{0,i}}{2} A_i \right] + j \frac{\mu_0 \omega_i^2}{2 \gamma_i \beta_{0,i}} (P_{NL,i}^{(2)}) \exp[j \beta_{0,i} z] = 0 \quad (\text{A.14})$$

where  $\alpha_{0,i}$  is the linear loss coefficient and it is defined as:

$$\alpha_{0,i} = \frac{\mu_0 \sigma c}{n_{0,i}} \quad (\text{A.15})$$

Various second-order nonlinear terms can be written (taking inverse Fourier transform of Equation (A.10)) as:

$$P_{NL,1} = \epsilon_0 \chi^{(2)} \gamma_2 \gamma_3 F_2^* F_3 A_2^* A_3 \exp[-j(\beta_{0,3} - \beta_{0,2})z] \quad (\text{A.16a})$$

$$P_{NL,2} = \epsilon_0 \chi^{(2)} \gamma_1 \gamma_3 F_1^* F_3 A_1^* A_3 \exp[-j(\beta_{0,3} - \beta_{0,1})z] \quad (\text{A.16b})$$

$$P_{NL,3} = \epsilon_0 \chi^{(2)} \gamma_1 \gamma_2 F_1 F_2 A_1 A_1 \exp[-j(\beta_{0,1} + \beta_{0,2})z] \quad (\text{A.16c})$$

Substituting all second-order nonlinear terms from Equation (A.16a) - (A.16c) in Equation (A.14) following coupled mode equations are obtained:

$$F_1 \left[ \frac{\partial A_1}{\partial z} + \beta_{1,1} \frac{\partial A_1}{\partial t} - j \frac{1}{2} \beta_{2,1} \frac{\partial^2 A_1}{\partial t^2} + \frac{\alpha_{0,1}}{2} A_1 \right] + j \frac{2\pi \chi^{(2)}}{\lambda_1 \sqrt{2c\epsilon_0 n_{0,1} n_{0,2} n_{0,3}}} F_2^* F_3 A_2^* A_3 \exp[-j \Delta \beta z] = 0 \quad (\text{A.17a})$$

$$F_2 \left[ \frac{\partial A_2}{\partial z} + \beta_{1,2} \frac{\partial A_2}{\partial t} - j \frac{1}{2} \beta_{2,2} \frac{\partial^2 A_2}{\partial t^2} + \frac{\alpha_{0,2}}{2} A_2 \right] + j \frac{2\pi \chi^{(2)}}{\lambda_2 \sqrt{2c\epsilon_0 n_{0,1} n_{0,2} n_{0,3}}} F_1^* F_3 A_1^* A_3 \exp[-j \Delta \beta z] = 0 \quad (\text{A.17b})$$

and

$$F_3 \left[ \frac{\partial A_3}{\partial z} + \beta_{1,3} \frac{\partial A_3}{\partial t} - j \frac{1}{2} \beta_{2,3} \frac{\partial^2 A_3}{\partial t^2} + \frac{\alpha_{0,3}}{2} A_3 \right] + j \frac{2\pi \chi^{(2)}}{\lambda_3 \sqrt{2c\epsilon_0 n_{0,1} n_{0,2} n_{0,3}}} F_1 F_2 A_1 A_2 \exp[j\Delta\beta z] = 0 \quad (\text{A.17c})$$

where  $\Delta\beta = \beta_{0,3} - \beta_{0,2} - \beta_{0,1}$  is the phase mismatch. Multiplying each equation by  $F_i^*$ , and integrating over x and y and then using Equation (A.12) one can write:

$$\frac{\partial A_1}{\partial z} + \beta_{1,1} \frac{\partial A_1}{\partial t} - j \frac{1}{2} \beta_{2,1} \frac{\partial^2 A_1}{\partial t^2} + \frac{\alpha_{0,1}}{2} A_1 + j \frac{\kappa_1}{\lambda_1} A_2^* A_3 \exp[-j\Delta\beta z] = 0 \quad (\text{A.18a})$$

$$\frac{\partial A_2}{\partial z} + \beta_{1,2} \frac{\partial A_2}{\partial t} - j \frac{1}{2} \beta_{2,2} \frac{\partial^2 A_2}{\partial t^2} + \frac{\alpha_{0,2}}{2} A_2 + j \frac{\kappa_2}{\lambda_2} A_1^* A_3 \exp[-j\Delta\beta z] = 0 \quad (\text{A.18b})$$

and

$$\frac{\partial A_3}{\partial z} + \beta_{1,3} \frac{\partial A_3}{\partial t} - j \frac{1}{2} \beta_{2,3} \frac{\partial^2 A_3}{\partial t^2} + \frac{\alpha_{0,3}}{2} A_3 + j \frac{\kappa_3}{\lambda_3} A_1 A_2 \exp[j\Delta\beta z] = 0 \quad (\text{A.18c})$$

where the second-order nonlinear coupling co-efficients are

$$\kappa_i = \frac{2\pi}{\sqrt{2c\epsilon_0 n_{0,1} n_{0,2} n_{0,3}}} f_i^{(2)} \quad (\text{A.19})$$

and the complex second-order overlap integral for waves 1 and 2 is ,

$$f_{1,2}^{(2)} = \int_{-\infty}^{\infty} \int_{-\infty}^{\infty} \chi^{(2)}(x, y) F_1^* F_2^* F_3 \, dx \, dy \quad (\text{A.20a})$$

and for the wave 3 is ,

$$f_3^{(2)} = \int_{-\infty}^{\infty} \int_{-\infty}^{\infty} \chi^{(2)}(x, y) F_1 F_2 F_3 \, dx \, dy \quad (\text{A.20b})$$



For a continuous wave propagating in a medium, propagation equations Equation (A.18a) to Equation (A.18c) can be simplified as:

$$\frac{\partial A_1}{\partial z} + \frac{\alpha_{0,1}}{2} A_1 - j \frac{\kappa_1}{\lambda_1} A_2^* A_3 \exp[-j \Delta \beta z] = 0 \quad (\text{A.21a})$$

$$\frac{\partial A_2}{\partial z} + \frac{\alpha_{0,2}}{2} A_2 - j \frac{\kappa_2}{\lambda_2} A_1^* A_3 \exp[-j \Delta \beta z] = 0 \quad (\text{A.21b})$$

$$\frac{\partial A_3}{\partial z} + \frac{\alpha_{0,3}}{2} A_3 - j \frac{\kappa_3}{\lambda_3} A_1 A_2 \exp[j \Delta \beta z] = 0 \quad (\text{A.21c})$$

### Effective Areas and Nonlinear Coefficients

In a waveguide the second- order effective area can be written in terms of non-normalized distributions  $\hat{F}_i$  as shown below :

$$S_{eff,1}^{(2)} = \frac{\left[ \int_{-\infty}^{\infty} \int_{-\infty}^{\infty} |\tilde{F}_1|^2 dx dy \right] \left[ \int_{-\infty}^{\infty} \int_{-\infty}^{\infty} |\tilde{F}_2|^2 dx dy \right] \left[ \int_{-\infty}^{\infty} \int_{-\infty}^{\infty} |\tilde{F}_3|^2 dx dy \right]}{\left[ \int_{-\infty}^{\infty} \int_{-\infty}^{\infty} \tilde{F}_1^* \tilde{F}_2^* \tilde{F}_3 dx dy \right]^2} \quad (\text{A.22})$$

Here, for waves 1 and 2,  $S_{eff,1}^{(2)} = S_{eff,2}^{(2)}$  and for wave 3,  $S_{eff,3}^{(2)} = S_{eff,1}^{(2)*}$ . Hence, second-order coupling coefficients can be written as:

$$\kappa_i = \frac{2\pi}{\sqrt{2c\epsilon_0 n_{0,1} n_{0,2} n_{0,3} S_{eff,i}^{(2)}}} \chi^{(2)} \quad (\text{A.23})$$

## Second-Harmonic Generation

In case of second-harmonic generation, the pump wave (frequency -  $\omega$ ) interacts with the second-harmonic wave (frequency -  $2\omega$ ) and corresponding nonlinear polarizations become:

$$P_{NL,\omega}^{(2)} = \epsilon_0 \chi^{(2)} \tilde{E}_\omega^* \tilde{E}_{2\omega} \quad (\text{A.24a})$$

$$P_{NL,2\omega}^{(2)} = \frac{1}{2} \epsilon_0 \chi^{(2)} \tilde{E}_\omega \tilde{E}_\omega \quad (\text{A.24b})$$

Hence, coupled wave equations for second harmonic generation becomes,

$$\frac{\partial A_\omega}{\partial z} + \beta_{1,\omega} \frac{\partial A_\omega}{\partial t} - j \frac{1}{2} \beta_{2,\omega} \frac{\partial^2 A_\omega}{\partial t^2} + \frac{\alpha_{0,\omega}}{2} A_\omega + j \frac{\kappa_\omega}{\lambda_\omega} A_\omega^* A_{2\omega} \exp[-j \Delta \beta z] = 0 \quad (\text{A.25a})$$

$$\frac{\partial A_{2\omega}}{\partial z} + \beta_{1,2\omega} \frac{\partial A_{2\omega}}{\partial t} - j \beta_{2,2\omega} \frac{\partial^2 A_{2\omega}}{\partial t^2} + \frac{\alpha_{0,2\omega}}{2} A_{2\omega} + j \frac{\kappa_{2\omega}}{\lambda_\omega} A_\omega A_\omega \exp[j \Delta \beta z] = 0 \quad (\text{A.25b})$$

where  $\Delta \beta = \beta_{2\omega} - 2\beta_\omega$ , and

$$\kappa_\omega = \pi \chi^{(2)} \sqrt{\frac{2}{c \epsilon_0 n_\omega^2 n_{2\omega} S_{eff}^{(2)}}} \quad (\text{A.26a})$$

$$\kappa_{2\omega} = \pi \chi^{(2)} \sqrt{\frac{2}{c \epsilon_0 n_\omega^2 n_{2\omega} S_{eff}^{(2)*}}} \quad (\text{A.26b})$$

which can be further simplified as:

$$\frac{\partial A_\omega}{\partial z} + \frac{\alpha_{0,\omega}}{2} A_\omega + j \sqrt{\eta_\omega} A_\omega^* A_{2\omega} \exp[-j \Delta \beta z] = 0 \quad (\text{A.27a})$$

and

$$\frac{\partial A_{2\omega}}{\partial z} + \frac{\alpha_{0,2\omega}}{2} A_{2\omega} + j \sqrt{\eta_{2\omega}^*} A_\omega A_\omega \exp[j \Delta \beta z] = 0 \quad (\text{A.27b})$$

Here,  $\chi^{(2)} = (d_{eff}/2\pi)$  is the effective non-linear co-efficient within the waveguide and  $\eta$  is the conversion efficiency for second harmonic generation.

$$\eta_{\omega} = \frac{k_{\omega}^2}{\lambda_{\omega}^2} = \frac{8\pi^2}{\epsilon_0 c} \left[ \frac{d_{eff}^2}{n_{\omega}^2 n_{2\omega} \lambda_{\omega}^2 S_{eff}^{(2)}} \right] \quad (\text{A.28a})$$

and

$$\eta_{2\omega}^* = \frac{k_{2\omega}^2}{\lambda_{\omega}^2} = \frac{8\pi^2}{\epsilon_0 c} \left[ \frac{d_{eff}^2}{n_{\omega}^2 n_{2\omega} \lambda_{\omega}^2 S_{eff}^{(2)*}} \right] \quad (\text{A.28b})$$

In general, the imaginary component of the overlap area is very small compared to the real part for a dielectric waveguide and the fundamental mode of propagation. Hence, it can be written as:  $S_{eff}^{(2)} = S_{eff}^{(2)*}$  and  $\eta_{\omega} = \eta_{2\omega}^* = \eta$ . Final coupled mode equations for second-harmonic generation can be written as:

$$\frac{\partial A_{\omega}}{\partial z} + \frac{\alpha_{0,\omega}}{2} A_{\omega} + j\sqrt{\eta} A_{\omega}^* A_{2\omega} \exp[-j\Delta\beta z] = 0 \quad (\text{A.29a})$$

$$\frac{\partial A_{2\omega}}{\partial z} + \frac{\alpha_{0,2\omega}}{2} A_{2\omega} + j\sqrt{\eta} A_{\omega} A_{\omega} \exp[j\Delta\beta z] = 0 \quad (\text{A.29b})$$

$$\eta = \frac{k_{\omega}^2}{\lambda_{\omega}^2} = \frac{8\pi^2}{\epsilon_0 c} \left[ \frac{d_{eff}^2}{n_{\omega}^2 n_{2\omega} \lambda_{\omega}^2 S_{eff}^{(2)}} \right] \quad (\text{A.29c})$$

and

$$S_{eff}^{(2)} = \frac{\left[ \int_{-\infty}^{\infty} \int_{-\infty}^{\infty} |\tilde{F}_1|^2 dx dy \right]^2 \left[ \int_{-\infty}^{\infty} \int_{-\infty}^{\infty} |\tilde{F}_2|^2 dx dy \right]}{\left[ \int_{-\infty}^{\infty} \int_{-\infty}^{\infty} |\tilde{F}_1|^2 \tilde{F}_2^* dx dy \right]^2} \quad (\text{A.29d})$$

## REFERENCES

- [1] R. S. Weis and T. K. Gaylord, "Lithium niobate: Summary of physical properties and crystal structure," *Applied Physics A*, vol. 37, no. 4, pp. 191–203, Aug. 1985.
- [2] L. Arizmendi, "Photonic Applications of Lithium Niobate Crystals," *Physica Status Solidi (a)*, vol. 201, no. 2, pp. 253 – 283, Jan. 2004.
- [3] G. Schreiber, D. Hofmann, W. Grundkoetter, Y. L. Lee, H. Suche, V. Quiring, R. Ricken, and W. Sohler, "Nonlinear integrated optical frequency converters with periodically poled Ti: LiNbO<sub>3</sub> waveguides," in *Proc. SPIE, Integrated Optics Devices V*, vol. 4277, 2001, pp. 144–160.
- [4] Y. Lee, C. Jung, Y. Noh, D. Ko, and J. Lee, "Photorefractive Effect in a Periodically Poled Ti:LiNbO<sub>3</sub> Channel Waveguide," *Journal of the Korean Physical Society*, vol. 44, no. 2, pp. 267–270, Feb. 2004.
- [5] J. Webjorn, V. Pruneri, P. Russell, J. Barr, and D. Hanna, "Quasi-phase-matched blue light generation in bulk lithium niobate, electrically poled via periodic liquid electrodes," *Electronics Letters*, vol. 30, no. 11, pp. 894–895, May 1994.
- [6] Y. S. Luh, M. Fejer, R. L. Byer, and R. Feigelson, "Stoichiometric LiNbO<sub>3</sub> single-crystal fibers for nonlinear optical applications," *Journal of Crystal Growth*, vol. 85, no. 1, pp. 264 – 269, 1987.
- [7] A. Yamada, H. Tamada, and M. Saitoh, "Liquid phase epitaxial growth of LiNbO<sub>3</sub> thin film using Li<sub>2</sub>O-B<sub>2</sub>O<sub>3</sub> flux system ," *Journal of Crystal Growth*, vol. 132, no. 1-2, pp. 48 – 60, Sep. 1993.
- [8] W. Sohler, H. Hu, R. Ricken, V. Quiring, C. Vannahme, H. Herrmann, D. Büchter, S. Reza, W. Grundkötter, S. Orlov, H. Suche, R. Nouroozi, and Y. Min, "Integrated Optical Devices in Lithium Niobate," *Optics and Photonics News*, vol. 19, no. 1, pp. 24–31, Jan. 2008.
- [9] W. K. Burns, P. H. Klein, E. J. West, and L. E. Plew, "Ti diffusion in Ti:LiNbO<sub>3</sub> planar and channel optical waveguides," *Journal of Applied Physics*, vol. 50, no. 10, pp. 6175–6182, Oct. 1979.
- [10] M. Bortz and M. M. Fejer, "Annealed proton-exchanged LiNbO<sub>3</sub> waveguides," *Optics Letters*, vol. 16, no. 23, pp. 1844–1846, Dec 1991.
- [11] R. Nevado and G. Lifante, "Low-loss, damage-resistant optical waveguides in Zn-diffused LiNbO<sub>3</sub> by a two-step procedure," *Applied Physics A*, vol. 72, no. 6, pp. 725–728, Jun. 2001.
- [12] F. Chen, Y. Tan, L. Wang, Q.-M. Lu, and H.-J. Ma, "Oxygen ion-implanted optical channel waveguides in Nd:MgO:LiNbO<sub>3</sub> : fabrication, characterization and simulation," *Journal of Physics D: Applied Physics*, vol. 40, no. 19, p. 5824, Sep. 2007.

- [13] O. Mikami, "LiNbO<sub>3</sub> coupled-waveguided TE/TM mode splitter," *Applied Physics Letters*, vol. 36, no. 7, pp. 491–493, Apr. 1980.
- [14] J. Ctyroky and H.-J. Henning, "Thin-film polariser for Ti:LiNbO<sub>3</sub> waveguides at  $\lambda=1.3 \mu\text{m}$ ," *Electronics Letters*, vol. 22, no. 14, pp. 756–757, Jul. 1986.
- [15] A. Neyer, "Low-crosstalk passive polarization splitters using Ti:LiNbO<sub>3</sub> waveguide crossings," *Applied Physics Letters*, vol. 55, no. 10, pp. 927–929, Sep. 1989.
- [16] K. D. Choquette, L. McCaughan, and W. K. Smith, "Improved optical switching extinction in three-electrode Ti:LiNbO<sub>3</sub> directional couplers," *Applied Physics Letters*, vol. 51, no. 25, pp. 2097–2099, Dec. 1987.
- [17] H. Hu, F. Lu, X. L. Wang, F. Chen, and K. M. Wang, "Low-loss optical waveguides and Y-branch splitters in lithium niobate fabricated by MeV oxygen ions with low dose," *Optics Express*, vol. 20, no. 19, pp. 21 114–21 118, Sep. 2012.
- [18] F. Rottmann, A. Neyer, W. Mevenkamp, and E. Voges, "Integrated-optic wavelength multiplexers on lithium niobate based on two-mode interference," *IEEE Journal of Lightwave Technology*, vol. 6, no. 6, pp. 946–952, Jun. 1988.
- [19] E. L. Wooten, R. L. Stone, E. W. Miles, and E. M. Bradley, "Rapidly tunable narrowband wavelength filter using LiNbO<sub>3</sub> unbalanced Mach-Zehnder interferometers," *IEEE Journal of Lightwave Technology*, vol. 14, no. 11, pp. 2530–2536, Nov. 1996.
- [20] C. Hussell and R. Ramaswamy, "High-index overlay for high reflectance DBR gratings in LiNbO<sub>3</sub> channel waveguides," *IEEE Photonics Technology Letters*, vol. 9, no. 5, pp. 636–638, May 1997.
- [21] B.-E. Benkelfat, R. Ferriere, B. Wacogne, and P. Mollier, "Technological implementation of Bragg grating reflectors in Ti:LiNbO<sub>3</sub> waveguides by proton exchange," *IEEE Photonics Technology Letters*, vol. 14, no. 10, pp. 1430–1432, Oct. 2002.
- [22] S. Kawanishi, M. H. Chou, K. Fujiura, M. M. Fejer, and T. Morioka, "All-optical modulation and time-division-multiplexing of 100 Gbit/s signal using quasi-phase matched mixing in LiNbO<sub>3</sub> waveguides," *Electronics Letters*, vol. 36, no. 18, pp. 1568–1569, Aug. 2000.
- [23] K. Noguchi, *Ultra-high-speed LiNbO<sub>3</sub> modulators*, *Ultrahigh-Speed Optical Transmission Technology*, ser. Optical and Fiber Communications Reports, H.-G. Weber and M. Nakazawa, Eds. Springer Berlin Heidelberg, 2007, vol. 3.
- [24] N. Kuwabara, K. Tajima, R. Kobayashi, and F. Amemiya, "Development and analysis of electric field sensor using LiNbO<sub>3</sub> optical modulator," *IEEE Transactions on Electromagnetic Compatibility*, vol. 34, no. 4, pp. 391–396, Nov. 1992.
- [25] G. L. Li and P. K. L. Yu, "Optical intensity modulators for digital and analog applications," *IEEE Journal of Lightwave Technology*, vol. 21, no. 9, pp. 2010–2030, Sep. 2003.
- [26] R.-C. Twu, H.-Y. Hong, and H.-H. Lee, "An optical homodyne technique to measure photorefractive-induced phase drifts in lithium niobate phase modulators," *Optics Express*, vol. 16, no. 6, pp. 4366–4374, Mar. 2008.

- [27] D. Janner, D. Tulli, M. Jofre, D. Yudistira, S. Balsamo, M. Belmonte, and V. Pruneri, "Domain Inverted Acousto- and Electrooptic Devices and Their Application to Optical Communication, Sensing, Laser Sources, and Quantum Key Distribution," *IEEE Journal of Selected Topics in Quantum Electronics*, vol. 19, no. 6, pp. 54–63, Nov. 2013.
- [28] F. Lucchi, D. Janner, M. Belmonte, S. Balsamo, M. Villa, S. Giurgola, P. Vergani, and V. Pruneri, "Very low voltage single drive domain inverted LiNbO<sub>3</sub> integrated electro-optic modulator," *Optics Express*, vol. 15, no. 17, pp. 10 739–10 743, Aug. 2007.
- [29] N. Courjal, H. Porte, J. Hauden, P. Mollier, and N. Grossard, "Modeling and optimization of low chirp LiNbO<sub>3</sub> Mach-Zehnder modulators with an inverted ferroelectric domain section," *IEEE Journal of Lightwave Technology*, vol. 22, no. 5, pp. 1338–1343, May 2004.
- [30] H. Murata and Y. Okamura, "Guided-Wave Optical Wavelength-Manipulating Devices Using Electrooptic Effect," *Photonics Based on Wavelength Integration and Manipulation, IPAP Books 2*, pp. 213–224, 2005.
- [31] F. Wehrmann, C. Harizi, H. Herrmann, U. Rust, W. Sohler, and S. Westenhofer, "Integrated optical, wavelength selective, acoustically tunable 2×2 switches (add-drop multiplexers) in LiNbO<sub>3</sub>," *IEEE Journal of Selected Topics in Quantum Electronics*, vol. 2, no. 2, pp. 263–269, Jun. 1996.
- [32] S. K. Dubey, T. Anna, C. Shakher, and D. S. Mehta, "Fingerprint detection using full-field swept-source optical coherence tomography," *Applied Physics Letters*, vol. 91, no. 18, pp. 181 106–3, Oct. 2007.
- [33] T. Xie, Z. Wang, and Y. Pan, "Dispersion compensation in high-speed optical coherence tomography by acousto-optic modulation," *Applied Optics*, vol. 44, no. 20, pp. 4272–4280, Jul. 2005.
- [34] N. Gupta and R. Dahmani, "Acousto-optic sensing and imaging for biomedical applications," in *Engineering in Medicine and Biology Society, 1997. Proceedings of the 19th Annual International Conference of the IEEE*, vol. 2, Oct. 1997, pp. 702–703.
- [35] J. F. Heanue, M. C. Bashaw, and L. Hesselink, "Volume holographic storage and retrieval of digital data," *Science*, vol. 265, no. 5173, pp. 749–752, Aug. 1994.
- [36] R. M. Shelby, J. A. Hoffnagle, G. W. Burr, C. M. Jefferson, M.-P. Bernal, H. Coufal, R. K. Grygier, H. Günther, R. M. Macfarlane, and G. T. Sincerbox, "Pixel-matched holographic data storage with megabit pages," *Optics Letters*, vol. 22, no. 19, pp. 1509–1511, Oct. 1997.
- [37] K. Buse, A. Adibi, and D. Psaltis, "Non-volatile holographic storage in doubly doped lithium niobate crystals," *Nature*, vol. 393, no. 6686, pp. 665–668, Jun. 1998.
- [38] X. Tan, O. Matoba, T. Shimura, K. Kuroda, and B. Javidi, "Secure optical storage that uses fully phase encryption," *Applied Optics*, vol. 39, no. 35, pp. 6689–6694, Dec. 2000.

- [39] S. Breer, K. Buse, K. Peithmann, H. Vogt, and E. Kratzig, “Stabilized recording and thermal fixing of holograms in photorefractive lithium niobate crystals,” *Review of Scientific Instruments*, vol. 69, no. 4, pp. 1591–1594, Apr. 1998.
- [40] R. Muller, M. T. Santos, L. Arizmendi, and J. M. Cabrera, “A narrow-band interference filter with photorefractive LiNbO<sub>3</sub>,” *Journal of Physics D Applied Physics*, vol. 27, 1994.
- [41] E. M. de Miguel-Sanz, M. Carrascosa, and L. Arizmendi, “Effect of the oxidation state and hydrogen concentration on the lifetime of thermally fixed holograms in LiNbO<sub>3</sub>:Fe,” *Physical Review B*, vol. 65, no. 16, pp. 165 101–7, Mar. 2002.
- [42] G. Barbastathis, M. Balberg, and D. J. Brady, “Confocal microscopy with a volume holographic filter,” *Optics Letters*, vol. 24, no. 12, pp. 811–813, Jun. 1999.
- [43] I. Nee, O. Beyer, M. Müller, and K. Buse, “Multichannel wavelength-division multiplexing with thermally fixed Bragg gratings in photorefractive lithium niobate crystals,” *Journal of the Optical Society of America B*, vol. 20, no. 8, pp. 1593–1602, Aug. 2003.
- [44] R. Brinkmann, W. Sohler, and H. Suche, “Continuous-wave erbium-diffused LiNbO<sub>3</sub> waveguide laser,” *Electronics Letters*, vol. 27, no. 5, pp. 415–417, Feb. 1991.
- [45] S. Helmfrid, G. Arvidsson, J. Webjorn, M. Linnarsson, and T. Pihl, “Stimulated emission in Er:Ti:LiNbO<sub>3</sub> channel waveguides close to 1.53  $\mu\text{m}$  transition,” *Electronics Letters*, vol. 27, no. 11, pp. 913–914, May 1991.
- [46] P. Becker, R. Brinkmann, M. Dinand, W. Sohler, and H. Suche, “Er-diffused Ti:LiNbO<sub>3</sub> waveguide laser of 1563 and 1576 nm emission wavelengths,” *Applied Physics Letters*, vol. 61, no. 11, pp. 1257–1259, Sep. 1992.
- [47] I. Baumann, R. Brinkmann, M. Dinand, W. Sohler, and S. Westenhofer, “Ti:Er:LiNbO<sub>3</sub> waveguide laser of optimized efficiency,” *IEEE Journal of Quantum Electronics*, vol. 32, no. 9, pp. 1695–1706, Sep. 1996.
- [48] I. Baumann, S. Bosso, R. Brinkmann, R. Corsini, M. Dinand, A. Greiner, K. Schafer, J. Sochtig, W. Sohler, H. Suche, and R. Wessel, “Er-doped integrated optical devices in LiNbO<sub>3</sub>,” *IEEE Journal of Selected Topics in Quantum Electronics*, vol. 2, no. 2, pp. 355–366, Jun. 1996.
- [49] R. Brinkmann, M. Dinand, I. Baumann, C. Harizi, W. Sohler, and H. Suche, “Acoustically tunable wavelength filter with gain,” *IEEE Photonics Technology Letters*, vol. 6, no. 4, pp. 519–521, Apr. 1994.
- [50] H. Suche, S. Bosso, C. Carmannini, R. Wessel, S. Westenhöfer, R. Corsini, and W. Sohler, “Harmonically mode-locked Ti:Er:LiNbO<sub>3</sub> waveguide laser,” *Optics Letters*, vol. 20, no. 6, pp. 596–598, Mar. 1995.
- [51] W. Sohler, “Integrated optical circuits with Er:LiNbO<sub>3</sub> amplifiers and lasers,” in *Optical Fiber Communications, 1996. OFC '96*, Feb. 1996, pp. 251–254.

- [52] H. Suche, T. Oesselke, J. Pandavenes, R. Ricken, K. Rochhausen, W. Sohler, S. Balsamo, I. Montrosset, and K. Wong, "Efficient Q-switched Ti:Er:LiNbO<sub>3</sub> waveguide laser," *Electronics Letters*, vol. 34, no. 12, pp. 1228–1230, Jun. 1998.
- [53] D. A. Smith, M. W. Maeda, J. J. Johnson, J. S. Patel, M. A. Saifi, and A. Von Lehman, "Acoustically tuned erbium-doped fiber ring laser," *Optics Letters*, vol. 16, no. 6, pp. 387–389, Mar 1991.
- [54] B. Das, H. Suche, and W. Sohler, "Single-frequency Ti:Er:LiNbO<sub>3</sub> distributed Bragg reflector waveguide laser with thermally fixed photorefractive cavity," *Applied Physics B*, vol. 73, no. 5-6, pp. 439–442, Oct. 2001.
- [55] C. Becker, T. Oesselke, J. Pandavenes, R. Ricken, K. Rochhausen, G. Schreiber, W. Sohler, H. Suche, R. Wessel, S. Balsamo, I. Montrosset, and D. Sciancalepore, "Advanced Ti:Er:LiNbO<sub>3</sub> waveguide lasers," *IEEE Journal of Selected Topics in Quantum Electronics*, vol. 6, no. 1, pp. 101–113, Jan. 2000.
- [56] J. Fonseca-Campos, Y. Wang, B. Chen, C.-Q. Xu, S. Yang, E. A. Ponomarev, and X. Bao, "40-GHz picosecond-pulse second-harmonic generation in an MgO-doped PPLN waveguide," *IEEE Journal of Lightwave Technology*, vol. 24, no. 10, pp. 3698–3708, Oct. 2006.
- [57] Y. L. Lee, C. Jung, Y.-C. Noh, I. W. Choi, D.-K. Ko, J. Lee, H.-Y. Lee, and H. Suche, "Wavelength selective single and dual-channel dropping in a periodically poled Ti:LiNbO<sub>3</sub> waveguide," *Optics Express*, vol. 12, no. 4, pp. 701–707, Feb. 2004.
- [58] B. Zhou, C.-Q. Xu, and B. Chen, "Comparison of difference-frequency generation and cascaded  $\chi^{(2)}$  based wavelength conversions in LiNbO<sub>3</sub> quasi-phase-matched waveguides," *Journal of the Optical Society of America B*, vol. 20, no. 5, pp. 846–852, May 2003.
- [59] C.-Q. Xu, J. Bracken, and B. Chen, "Intracavity wavelength conversions employing a MgO-doped LiNbO<sub>3</sub> quasi-phase-matched waveguide and an erbium-doped fiber amplifier," *Journal of the Optical Society of America B*, vol. 20, no. 10, pp. 2142–2149, Oct. 2003.
- [60] Y. L. Lee, B.-A. Yu, C. Jung, Y.-C. Noh, J. Lee, and D.-K. Ko, "All-optical wavelength conversion and tuning by the cascaded sum- and difference frequency generation (cSFG/DFG) in a temperature gradient controlled Ti:PPLN channel waveguide," *Optics Express*, vol. 13, no. 8, pp. 2988–2993, Apr. 2005.
- [61] W. Sohler and H. Suche, "Optical parametric amplification in Ti-diffused LiNbO<sub>3</sub> waveguides," *Applied Physics Letters*, vol. 37, no. 3, pp. 255–257, Aug. 1980.
- [62] J. Yamawaku, H. Takara, T. Ohara, A. Takada, T. Morioka, O. Tadanaga, H. Miyazawa, and M. Asobe, "Low-Crosstalk 103 Channel  $\times$ , 10 Gb/s (1.03 Tb/s) Wavelength Conversion With a Quasi-Phase-Matched LiNbO<sub>3</sub> Waveguide," *IEEE Journal of Selected Topics in Quantum Electronics*, vol. 12, no. 4, pp. 521–528, July 2006.



- [63] D. J. L. Birkin, E. U. Rafailov, G. S. Sokolovskii, W. Sibbett, G. W. Ross, P. G. R. Smith, and D. C. Hanna, “3.6 mw blue light by direct frequency doubling of a diode laser using an aperiodically poled lithium niobate crystal,” *Applied Physics Letters*, vol. 78, no. 21, pp. 3172–3174, May 2001.
- [64] P. Loza-Alvarez, M. Ebrahimzadeh, W. Sibbett, D. T. Reid, D. Artigas, and M. Missey, “Femtosecond second-harmonic pulse compression in aperiodically poled lithium niobate: a systematic comparison of experiment and theory,” *Journal of the Optical Society of America B*, vol. 18, no. 8, pp. 1212–1217, Aug. 2001.
- [65] J. Capmany, “Simultaneous generation of red, green, and blue continuous-wave laser radiation in Nd<sup>3+</sup>-doped aperiodically poled lithium niobate,” *Applied Physics Letters*, vol. 78, no. 2, pp. 144–146, Jan. 2001.
- [66] W. Sohler, “Integrated Optical Parametric Oscillators with Ti:PPLN Waveguides,” in *Conference on Lasers and Electro-Optics /Quantum Electronics and Laser Science and Photonic Applications Systems Technologies*. Optical Society of America, 2005.
- [67] J. Webjorn, S. Siala, D. Nam, R. Waarts, and R. J. Lang, “Visible laser sources based on frequency doubling in nonlinear waveguides,” *IEEE Journal of Quantum Electronics*, vol. 33, no. 10, pp. 1673–1686, Oct. 1997.
- [68] K. Petrov, S. Waltman, E. Dlugokencky, M. Arbore, M. Fejer, F. Tittel, and L. Hollberg, “Precise measurement of methane in air using diode-pumped 3.4  $\mu\text{m}$  difference-frequency generation in PPLN,” *Applied Physics B*, vol. 64, no. 5, pp. 567–572, Apr. 1997.
- [69] S. Tanzilli, W. Tittel, H. De Riedmatten, H. Zbinden, P. Baldi, M. DeMicheli, D. Ostrowsky, and N. Gisin, “Ppln waveguide for quantum communication,” *The European Physical Journal D*, vol. 18, no. 2, pp. 155–160, Feb. 2002.
- [70] A. C. Busacca, C. L. Sones, R. W. Eason, and S. Mailis, “First-order quasi-phase-matched blue light generation in surface-poled Ti:indiffused lithium niobate waveguides,” *Applied Physics Letters*, vol. 84, no. 22, pp. 4430–4432, May 2004.
- [71] H. Jin, F. M. Liu, P. Xu, J. L. Xia, M. L. Zhong, Y. Yuan, J. W. Zhou, Y. X. Gong, W. Wang, and S. N. Zhu, “On-Chip Generation and Manipulation of Entangled Photons Based on Reconfigurable Lithium-Niobate Waveguide Circuits,” *Physical Review Letters*, vol. 113, no. 10, pp. 103 601–5, Sep. 2014.
- [72] M. Chou, I. Brener, M. Fejer, E. Chaban, and S. Christman, “1.5-  $\mu\text{m}$ -band wavelength conversion based on cascaded second-order nonlinearity in LiNbO<sub>3</sub> waveguides,” *IEEE Photonics Technology Letters*, vol. 11, no. 6, pp. 653–655, Jun. 1999.
- [73] C. Langrock, S. Kumar, J. E. McGeehan, A. E. Willner, and M. M. Fejer, “All-optical signal processing using  $\chi^{(2)}$  nonlinearities in guided-wave devices,” *IEEE Journal of Lightwave Technology*, vol. 24, no. 7, pp. 2579–2592, July 2006.
- [74] J. Wang, J. Sun, X. Zhang, and D. Huang, “All-Optical Tunable Wavelength Conversion With Extinction Ratio Enhancement Using Periodically Poled Lithium Niobate Waveguides,” *IEEE Journal of Lightwave Technology*, vol. 26, no. 17, pp. 3137–3148, Sep. 2008.

- [75] T. Fujiwara, R. Srivastava, X. Cao, and R. V. Ramaswamy, “Comparison of photorefractive index change in proton-exchanged and Ti-diffused LiNbO<sub>3</sub> waveguides,” *Optics Letters*, vol. 18, no. 5, pp. 346–348, Mar. 1993.
- [76] M. Rottschalk, T. Bachmann, S. Steinberg, and J.-P. Ruske, “Annealed proton-implanted channel waveguides in LiNbO<sub>3</sub> and their photorefractive properties,” *Optics Communications*, vol. 106, no. 4-6, pp. 187–192, Mar. 1994.
- [77] M. Jubera, A. G. Cabanes, M. Carrascosa, J. Olivares, and F. Luedtke, “Characterization and inhibition of photorefractive optical damage of swift heavy ion irradiation waveguides in LiNbO<sub>3</sub>,” *Journal of the Optical Society of America B*, vol. 29, no. 11, pp. 3000–3005, Nov 2012.
- [78] J. Rams, A. Alcazar-de Velasco, M. Carrascosa, J. M. Cabrera, and F. Agulla-Lopez, “Optical damage inhibition and thresholding effects in lithium niobate above room temperature,” *Optics Communications*, vol. 178, no. 1-3, pp. 211 – 216, 2000.
- [79] H. Liu, X. Xie, Y. Kong, W. Yan, X. Li, L. Shi, J. Xu, and G. Zhang, “Photorefractive properties of near-stoichiometric lithium niobate crystals doped with iron,” *Optical Materials*, vol. 28, no. 3, pp. 212 – 215, 2006.
- [80] P. Günter and J. P. Huignard, Eds., *Photorefractive Materials and Their Applications 2*, 1st ed., ser. Springer Series in Optical Sciences. Springer New York, 2007, vol. 114.
- [81] T. Volk, N. Rubinina, and M. Wohlecke, “Optical-damage-resistant impurities in Lithium Niobate,” *Journal of the Optical Society of America B*, vol. 11, no. 9, pp. 1681–1687, Sep. 1994.
- [82] D. A. Bryan, R. Gerson, and H. E. Tomaschke, “Increased optical damage resistance in lithium niobate,” *Applied Physics Letters*, vol. 44, no. 9, pp. 847–849, May 1984.
- [83] M. Asobe, O. Tadanaga, T. Yanagawa, H. Itoh, and H. Suzuki, “Reducing photorefractive effect in periodically poled ZnO- and MgO-doped LiNbO<sub>3</sub> wavelength converters,” *Applied Physics Letters*, vol. 78, no. 21, pp. 3163–3165, Mar. 2001.
- [84] M. Falk, T. Woike, and K. Buse, “Reduction of optical damage in lithium niobate crystals by thermo-electric oxidization,” *Applied Physics Letters*, vol. 90, no. 25, pp. 2519–2521, Jun. 2007.
- [85] J. Carnicero, M. Carrascosa, A. Mendez, A. G. Cabanes, and J. M. Cabrera, “Optical damage control via the Fe<sup>2+</sup>/Fe<sup>3+</sup> ratio in proton-exchanged LiNbO<sub>3</sub> waveguides,” *Optics Letters*, vol. 32, no. 16, pp. 2294–2296, Aug. 2007.
- [86] M. Kusters, B. Sturman, P. Werheit, D. Haertle, and K. Buse, “Optical cleaning of congruent lithium niobate crystals,” *Nature Photonics*, vol. 3, no. 9, pp. 510–513, Sep 2009.
- [87] Y. Nishida, H. Miyazawa, M. Asobe, O. Tadanaga, and H. Suzuki, “Direct-bonded QPM-LN ridge waveguide with high damage resistance at room temperature,” *Electronics Letters*, vol. 39, no. 7, pp. 609–611, Apr. 2003.

- [88] T. Sugita, K. Mizuuchi, K. Yamamoto, K. Fukuda, T. Kai, I. Nakayama, and K. Takahashi, "Highly efficient second-harmonic generation in direct-bonded MgO:LiNbO<sub>3</sub> pure crystal waveguide," *Electronics Letters*, vol. 40, no. 21, pp. 1359–1361, Oct. 2004.
- [89] Y. Nishida, H. Miyazawa, M. Asobe, O. Tadanaga, and H. Suzuki, "0-dB wavelength conversion using direct-bonded QPM-Zn:LiNbO<sub>3</sub> ridge waveguide," *IEEE Photonics Technology Letters*, vol. 17, no. 5, pp. 1049–1051, May 2005.
- [90] L. Gui, "Periodically poled ridge waveguides and photonic wires in linbo<sub>3</sub> for efficient nonlinear interactions," Ph.D. dissertation, Department of Physics, University of Paderborn, 2010.
- [91] D. Jedrzejczyk, R. Güther, K. Paschke, G. Erbert, and G. Tränkle, "Diode laser frequency doubling in a ppMgO:LN ridge waveguide: influence of structural imperfection, optical absorption and heat generation," *Applied Physics B*, vol. 109, no. 1, pp. 33–42, Sep 2012.
- [92] J. Sun and C. Xu, "466 mW green light generation using annealed proton-exchanged periodically poled MgO:LiNbO<sub>3</sub> ridge waveguides," *Optics Letters*, vol. 37, no. 11, pp. 2028–2030, Jun. 2012.
- [93] A. Ashkin, G. D. Boyd, J. M. Dziedzic, R. G. Smith, A. A. Ballman, J. J. Levinstein, and K. Nassau, "Optically Induced Refractive Index Inhomogeneities in LiNbO<sub>3</sub> and LiTaO<sub>3</sub>," *Applied Physics Letters*, vol. 9, no. 1, pp. 72–74, Nov. 1966.
- [94] F. S. Chen, J. T. LaMacchia, and D. B. Fraser, "Holographic Storage in Lithium Niobate," *Applied Physics Letters*, vol. 13, no. 7, pp. 223–225, Oct. 1968.
- [95] D. L. Staebler, W. J. Burke, W. Phillips, and J. J. Amodei, "Multiple storage and erasure of fixed holograms in Fe-doped LiNbO<sub>3</sub>," *Applied Physics Letters*, vol. 26, no. 4, pp. 182–184, Feb. 1975.
- [96] F. S. Chen, "Optically Induced Change of Refractive Indices in LiNbO<sub>3</sub> and LiTaO<sub>3</sub>," *Journal of Applied Physics*, vol. 40, no. 8, pp. 3389–3396, Jul. 1969.
- [97] L. R. Dalton, P. Günter, M. Jazbinsek, O.-P. Kwon, and P. A. Sullivan, *Organic Electro-Optics and Photonics*. Cambridge University Press, Oct. 2015.
- [98] Y. Kong, S. Liu, and J. Xu, "Recent Advances in the Photorefraction of Doped Lithium Niobate Crystals," *Materials*, vol. 5, no. 10, p. 1954, Oct. 2012.
- [99] R. G. Smith, D.B.Fraser, R.T.Denton, and T. Rich, "Correlation of Reduction in Optically Induced Refractive Index Inhomogeneity with OH<sup>-</sup> Content in LiTaO<sub>3</sub> and LiNbO<sub>3</sub>," *Journal of Applied Physics*, vol. 39, no. 10, pp. 4600–4602, Nov 1968.
- [100] G. E. Peterson, A.M.Glass, and T. Negran, "Control of the Susceptibility of Lithium Niobate to Laser-Induced Refractive Index Changes," *Applied Physics Letters*, vol. 19, no. 5, pp. 130–132, Sep. 1971.
- [101] *Study of resistance against photorefractive light-induced scattering in LiNbO<sub>3</sub>:Fe,Mg crystals*, vol. 2529, 1995.

- [102] M. Volk, T. and Wohlecke, N. Rubinina, A. Reichert, and N. Razumovski, "Optical-damage-resistant impurities (Mg, Zn, In, Sc) in lithium niobate," *Ferroelectrics*, vol. 183, no. 1, pp. 291–300, Jan. 1996.
- [103] D. L. Staebler and J. J. Amodei, "Thermally fixed holograms in LiNbO<sub>3</sub>," *Ferroelectrics*, vol. 3, no. 1, pp. 107–113, Nov. 1972.
- [104] I. B. Barkan, S. I. Marennikov, and M. V. Entin, "Holographic storage in LiNbO<sub>3</sub> crystal at high temperatures," *Physica Status Solidi (a)*, vol. 38, no. 2, pp. K139–K142, Dec. 1976.
- [105] A. M. Glass, "The Photorefractive Effect," *Optical Engineering*, vol. 17, no. 5, pp. 470–479, Sep. 1978.
- [106] P. Günter and H. Eichler, Eds., *Electro-optic and Photorefractive Materials*, ser. Springer Proceedings in Physics. Springer Berlin Heidelberg, 1987, vol. 18, proceedings of the International School on Material Science and Technology, Erice, Italy, July 6–17, 1986.
- [107] H. Kurz, "Wavelength dependence of the photorefractive process in doped LiNbO<sub>3</sub>," *Ferroelectrics*, vol. 8, no. 1, pp. 437–439, Sep. 1974.
- [108] P. Dittrich, G. Montemezzani, M. Habu, M. Matsukura, S. Takekawa, K. Kitamura, and P. Gunter, "Sub-millisecond interband photorefractive process in magnesium doped lithium tantalate," *Optics Communications*, vol. 234, no. 1-6, pp. 131–136, Apr. 2004.
- [109] T. R. Volk, S. A. Shramchenko, and L. Shuvalov, "X-Ray induced change of the refractive indices in LiNbO<sub>3</sub> crystals," *Ferroelectrics Letters*, vol. 2, no. 2, pp. 55–58, Feb 1984.
- [110] E. R. Hodgson and F. Agullo-Lopez, "Displacement damage in LiNbO<sub>3</sub>," *Nuclear Instruments and Methods in Physics Research Section B*, vol. 32, no. 1, pp. 42–44, May 1988.
- [111] A. M. Glass, D. von der Linde, and T. J. Negran, "High-voltage bulk photovoltaic effect and the photorefractive process in LiNbO<sub>3</sub>," *Applied Physics Letters*, vol. 25, no. 4, pp. 233–235, Aug. 1974.
- [112] K. Buse, "Light-induced charge transport processes in photorefractive crystals II : Materials," *Applied Physics B*, vol. 64, no. 4, pp. 391–407, Mar. 1997.
- [113] V. Belinicher, V. K. Malinovski, and B. I. Sturman, "Photogalvanic effect in a crystal with polar axis," *Soviet Journal of Experimental and Theoretical Physics (Soviet Physics JETP)*, vol. 46, no. 2, pp. 362–366, Aug. 1977.
- [114] V. Fradkin and R. M. Magomadov, "Anomalous photovoltaic effect in LiNbO<sub>3</sub>:Fe in polarized light," *Journal of Experimental and Theoretical Physics Letters*, vol. 38, no. 11, pp. 686–688, Dec 1979.
- [115] O. F. Schirmer, "X-ray photovoltaic effect in undoped LiNbO<sub>3</sub> and its correlation with ESR," *Journal of Applied Physics*, vol. 50, no. 5, pp. 3404–3406, May 1979.

- [116] E. Krätzig, “Photorefractive effects and photoconductivity in  $\text{LiNbO}_3\text{:Fe}$ ,” *Ferroelectrics*, vol. 21, no. 1, pp. 635–636, Sep. 1978.
- [117] N. V. Kukhtarev, V. B. Markov, S. G. Odulov, M. S. Soskin, and V. L. Vinetskii, “Holographic storage in electrooptic crystals. I. steady state,” *Ferroelectrics*, vol. 22, no. 1, pp. 949–960, Jan 1978.
- [118] N. V. Kukhtarev, V.B.Markov, , S. Odulov, M. Soskin, and V. Vinetskii, “Holographic storage in electrooptic crystals. II. beam coupling and light amplification,” *Ferroelectrics*, vol. 22, no. 1, pp. 961–964, Jan 1978.
- [119] T. Volk and M. Wöhlecke, *Lithium Niobate*, 1st ed., ser. Springer Series in Materials Science, R. Hull, C. Jagadish, R. Osgood, J. Parisi, T.-Y. Seong, Z. Uchida, S.-i.and Wang, and Y. Kawazoe, Eds. Springer-Verlag Berlin Heidelberg, 2009, vol. 115.
- [120] P. Günter and J. P. Huignard, Eds., *Photorefractive Materials and Their Applications I: Basic Effects*, 1st ed., ser. Springer Series in Optical Sciences. Springer-Verlag New York, 2006, vol. 113.
- [121] O. Althoff, A. Erdmann, L. Wiskott, and P. Hertel, “The Photorefractive Effect in  $\text{LiNbO}_3$  at High Light Intensity,” *Physica Status Solidi (a)*, vol. 128, no. 1, pp. K41–K46, Apr. 1991.
- [122] F. Jermann and J. Otten, “Light-induced charge transport in  $\text{LiNbO}_3\text{:Fe}$  at high light intensities,” *Journal of the Optical Society of America B*, vol. 10, no. 11, pp. 2085–2092, Nov 1993.
- [123] F. Jermann, M. Simon, and E. Krätzig, “Photorefractive properties of congruent and stoichiometric lithium niobate at high light intensities,” *Journal of the Optical Society of America B*, vol. 12, no. 11, pp. 2066–2070, Nov. 1995.
- [124] E. E. Kraetzig and R. Sommerfeldt, “Influence of dopants on photorefractive properties of  $\text{LiNbO}_3$  crystals,” *SPIE Proceedings*, vol. 1273, pp. 2–11, Aug. 1990.
- [125] F. Jermann and E. Krätzig, “Charge transport processes in  $\text{LiNbO}_3\text{:Fe}$  at high intensity laser pulses,” *Applied Physics A*, vol. 55, no. 1, pp. 114–118, Jul. 1992.
- [126] F. Devaux, J. Safioui, M. Chauvet, and R. Passier, “Two-photoactive-center model applied to photorefractive self-focusing in biased  $\text{LiNbO}_3$ ,” *Physical Review A*, vol. 81, no. 1, pp. 013 825–6, Jan. 2010.
- [127] K. Peithmann, A. Wiebrock, and K. Buse, “Photorefractive properties of highly-doped lithium niobate crystals in the visible and near-infrared,” *Applied Physics B*, vol. 68, no. 5, pp. 777–784, May 1999.
- [128] M. H. Chou, J. Hauden, M. A. Arbore, and M. M. Fejer, “1.5- $\mu\text{m}$ -band wavelength conversion based on difference-frequency generation in  $\text{LiNbO}_3$  waveguides with integrated coupling structures,” *Optics Letters*, vol. 23, no. 13, pp. 1004–1006, Jul. 1998.

- [129] H. Hu, R. Nouroozi, W. Wang, J. Yu, H. Suche, and W. Sohler, "Tunable All-Optical Wavelength Conversion Based on Cascaded SHG/DFG in a Ti:PPLN Waveguide Using a Single CW Control Laser," *IEEE Photonics Journal*, vol. 4, no. 5, pp. 1396–1400, Oct. 2012.
- [130] R. White, I. McKinnie, S. Butterworth, G. Baxter, D. Warrington, P. Smith, G. Ross, and D. Hanna, "Tunable single-frequency ultraviolet generation from a continuous-wave Ti:sapphire laser with an intracavity PPLN frequency doubler," *Applied Physics B*, vol. 77, no. 6, pp. 547–550, Oct. 2003.
- [131] B. Chen, J. F. Campos, W. Liang, Y. Wang, and C.-Q. Xu, "Wavelength and temperature dependence of photorefractive effect in quasi-phase-matched LiNbO<sub>3</sub> waveguides," *Applied Physics Letters*, vol. 89, no. 4, pp. 043 510–3, Jul. 2006.
- [132] J. Ctyroky, M. Hofman, J. Janta, and J. Schrofel, "3-D analysis of LiNbO<sub>3</sub>:Ti channel waveguides and directional couplers," *IEEE Journal of Quantum Electronics*, vol. 20, no. 4, pp. 400–409, Apr. 1984.
- [133] S. Fouchet, A. Carencio, C. Daguet, R. Guglielmi, and L. Riviere, "Wavelength dispersion of Ti induced refractive index change in LiNbO<sub>3</sub> as a function of diffusion parameters," *IEEE Journal of Lightwave Technology*, vol. 5, no. 5, pp. 700–708, May 1987.
- [134] M. A. R. Franco, L. C. d. Vasconcellos, and J. M. Machado, "Coupling Efficiency Between Optical Fiber and Ti:LiNbO<sub>3</sub> Channel Waveguide," *Revista Científica Periódica - Telecomunicacoes*, vol. 7, no. 1, pp. 54–59, Jul. 2004.
- [135] J. A. Armstrong, N. Bloembergen, J. Ducuing, and P. Pershan, "Interactions between light waves in a nonlinear dielectric," *Physical Review*, vol. 127, no. 6, pp. 1918–1939, Sep. 1962.
- [136] R. Schiek and T. Pertsch, "Absolute measurement of the quadratic nonlinear susceptibility of lithium niobate in waveguides," *Optical Materials Express*, vol. 2, no. 2, pp. 126–139, Feb. 2012.
- [137] L. Gui, H. Hu, M. Garcia-Granda, and W. Sohler, "Local periodic poling of ridges and ridge waveguides on X- and Y-Cut LiNbO<sub>3</sub> and its application for second harmonic generation," *Optics Express*, vol. 17, no. 5, pp. 3923–3928, Mar. 2009.
- [138] S. Pal, A. K. Sahoo, and B. Das, "Experimental Studies on Swelling and Surface Roughness Dependent Guiding Properties of APE: LiNbO<sub>3</sub> Channel Waveguides," in *International Conference on Fiber Optics and Photonics (Photonics)*, Dec. 2008.
- [139] K. Rajneesh, S. Pal, and B. Das, "Fabrication and Characterization of Integrated Optical TE-Pass Polarizer in LiNbO<sub>3</sub>," in *International Conference on Optics and Photonics-2009*, Oct. 2009.
- [140] H. Hu, R. Ricken, W. Sohler, and R. Wehrspohn, "Lithium niobate ridge waveguides fabricated by wet etching," *IEEE Photonics Technology Letters*, vol. 19, no. 6, pp. 417–419, Mar. 2007.

- [141] K. Wong, A. Nutt, D. Clark, P. Laybourn, R. De La Rue, and J. Winfield, "Characterisation of proton-exchange slab optical waveguides in x-cut LiNbO<sub>3</sub>," *IEE Proceedings Journal Optoelectronics*, vol. 133, no. 2, pp. 113–117, Apr. 1986.
- [142] H. Nagata, N. Mitsugi, K. Shima, M. Tamai, and E. Haga, "Growth of crystalline LiF on CF<sub>4</sub> plasma etched LiNbO<sub>3</sub> substrates," *Journal of Crystal Growth*, vol. 187, no. 3-4, pp. 573–576, May 1998.
- [143] O. Espeso, G. Garcia, A. Climent, F. Agullo-Lopez, G. de la Paliza, J. M. Cabrera, and T. Sajavaara, "H-Li correlation and stoichiometry of mixed phases in proton-exchanged LiNbO<sub>3</sub> waveguides," *Journal of Applied Physics*, vol. 94, no. 12, pp. 7710–7718, Dec. 2003.
- [144] R. Regener and W. Sohler, "Loss in low-finesse Ti:LiNbO<sub>3</sub> optical waveguide resonators," *Applied Physics B*, vol. 36, no. 3, pp. 143–147, Mar. 1985.
- [145] J. R. Kurz, "Integrated Optical-Frequency Mixers," Ph.D. dissertation, Department of Applied Physics, Stanford University, Nov. 2003.
- [146] S. J. Wagner, "Wavelength Conversion in Domain-Disordered Quasi-Phase Matching Superlattice Waveguides," Ph.D. dissertation, Department of Electrical and Computer Engineering, University of Toronto, 2011.
- [147] G. P. Agrawal, *Nonlinear Fiber Optics*, 5th ed., ser. Optics and Photonics. Academic Press, Oct. 2012.

# APPENDIX B

## LIST OF PAPERS BASED ON THESIS

### Papers in Journal/Proceedings

1. **S. Pal** , B. K. Das and W. Sohler  
Photorefractive damage resistance in Ti:PPLN waveguides with ridge geometry.  
*Applied Physics B*, **120**, 737 (2015).
2. **S. Pal** , B. K. Das  
Fabrication of ridge waveguide in X-cut LiNbO<sub>3</sub> for nonlinear optic applications.  
*Proc. SPIE*, **8173**, 81730W (2011).

### Papers in Conferences

1. W. Sohler, H. Herrmann, R. Ricken, V. Quiring, M. George, **S. Pal**, X. Yang, K. Luo, C. Silberhorn, F. Kaiser, S. Tanzilli, E. Saglamyurek, N. Sinclair, D. Oblak, W. Tittel.  
**Title** : *Integrated Photon Pair Sources, Quantum Memories, and Lasers in Lithium Niobate.*  
**5th International Photonics and Opto-Electronics Meetings (POEM 2012)**, 01-02 November 2012, Wuhan, China.
2. **S. Pal**, B. K. Das.  
**Title** : *Fabrication of Ridge Waveguide in X-cut Lithium Niobate for Nonlinear optic Applications.*  
**The International Conference on Fiber Optics and Photonics-PHOTONICS 2010**, 11-15 December 2010, Guwahati, India.
3. K. Rajneesh, **S. Pal**, B. K. Das.  
**Title** : *Fabrication and Characterization of Integrated Optical TE-Pass Polarizer in LiNbO<sub>3</sub>.*  
**The International Conference on Optics and Photonics (ICOP)-2009**, 30 October-01 November 2009, Chandigarh, India.
4. **S. Pal**, A. K. Sahoo, B. K. Das.  
**Title** : *Experimental Studies on Swelling and Surface Roughness Dependent Guiding Properties of APE: LiNbO<sub>3</sub> Channel Waveguides.*  
**The International Conference on Fiber Optics and Photonics-PHOTONICS 2008**, 13-17 December 2008, New Delhi, India.



# APPENDIX C

## CURRICULUM VITAE

**Name** : Shantanu Pal

**Date of birth** : 14-February-1979

**Educational qualification** : M.Tech

**2004 Master of Science (M. Sc)**

Institution : University of Calcutta

Specialization : Condensed Matter Physics

**2006 Master of Technology (M. Tech)**

Institution : Indian Institute of Technology Kharagpur

Specialization : Solid State Technology

# APPENDIX D

## DOCTORAL COMMITTEE

**CHAIR PERSON** : Dr. Harishankar Ramachandran

Professor and Head

Department of Electrical Engineering

Indian Institute of Technology, Madras

**GUIDE** : Dr. Bijoy Krishna Das

Associate Professor

Department of Electrical Engineering

Indian Institute of Technology, Madras

**MEMBERS** : Dr. Nandita DasGupta

Professor

Department of Electrical Engineering

Indian Institute of Technology, Madras

: Dr. Nilesh J. Vasa

Professor

Department of Engineering Design

Indian Institute of Technology, Madras

: Dr. C. Vijayan

Professor

Department of Physics

Indian Institute of Technology, Madras